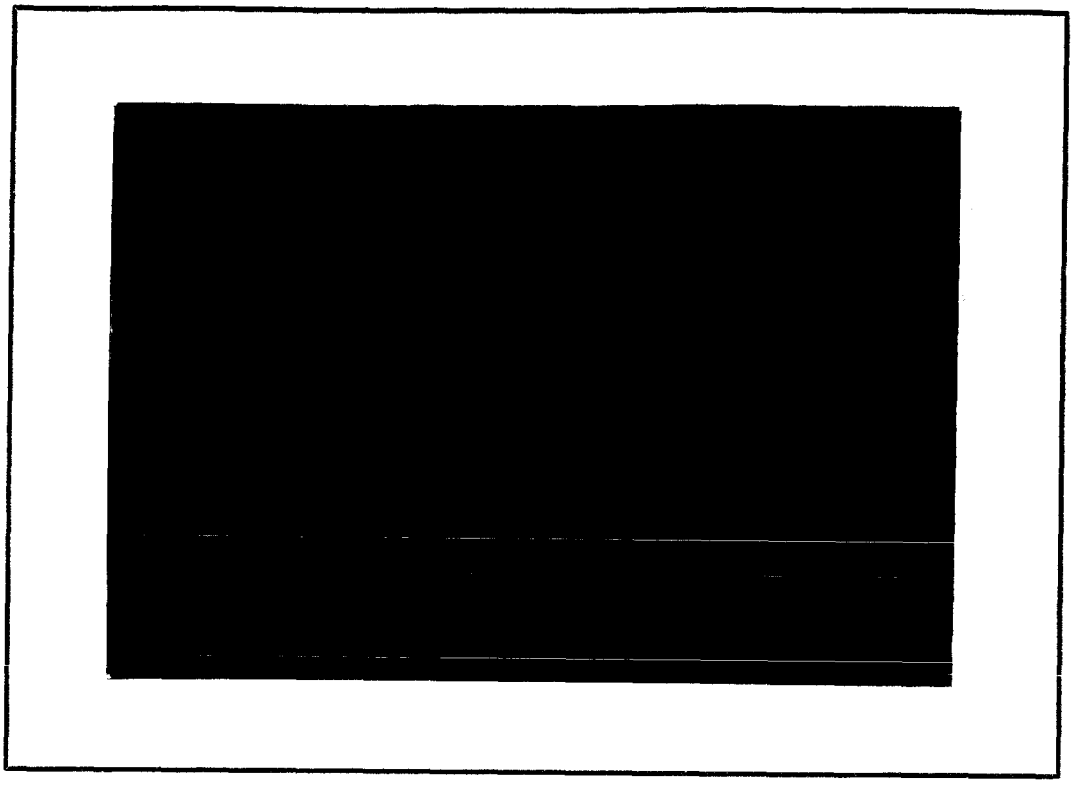

(NASA-CR-132786) ELECTRON-PROTON SPECTROMETER Final Project Report (Minnesota Univ.) 99 p HC $7.00 N73-27381

CSCL 14B Unclas
G3/14 09266

COSMIC PHYSICS GROUP

School of Physics and Astronomy

UNIVERSITY OF MINNESOTA

FINAL PROJECT REPORT

FOR

ELECTRON-PROTON SPECTROMETER

Contract No: NAS 5-11687

Goddard Space Flight Center
Contracting Officer: John Blum
Technical Officer: Robert Wales

Cosmic Physics Report
No. CR-163

Prepared By:

University of Minnesota
School of Physics and Astronomy
Minneapolis, Minnesota 55455

Principal Experimenter: John R. Winckler

For

GODDARD SPACE FLIGHT CENTER
Greenbelt, Maryland

May 1973

/

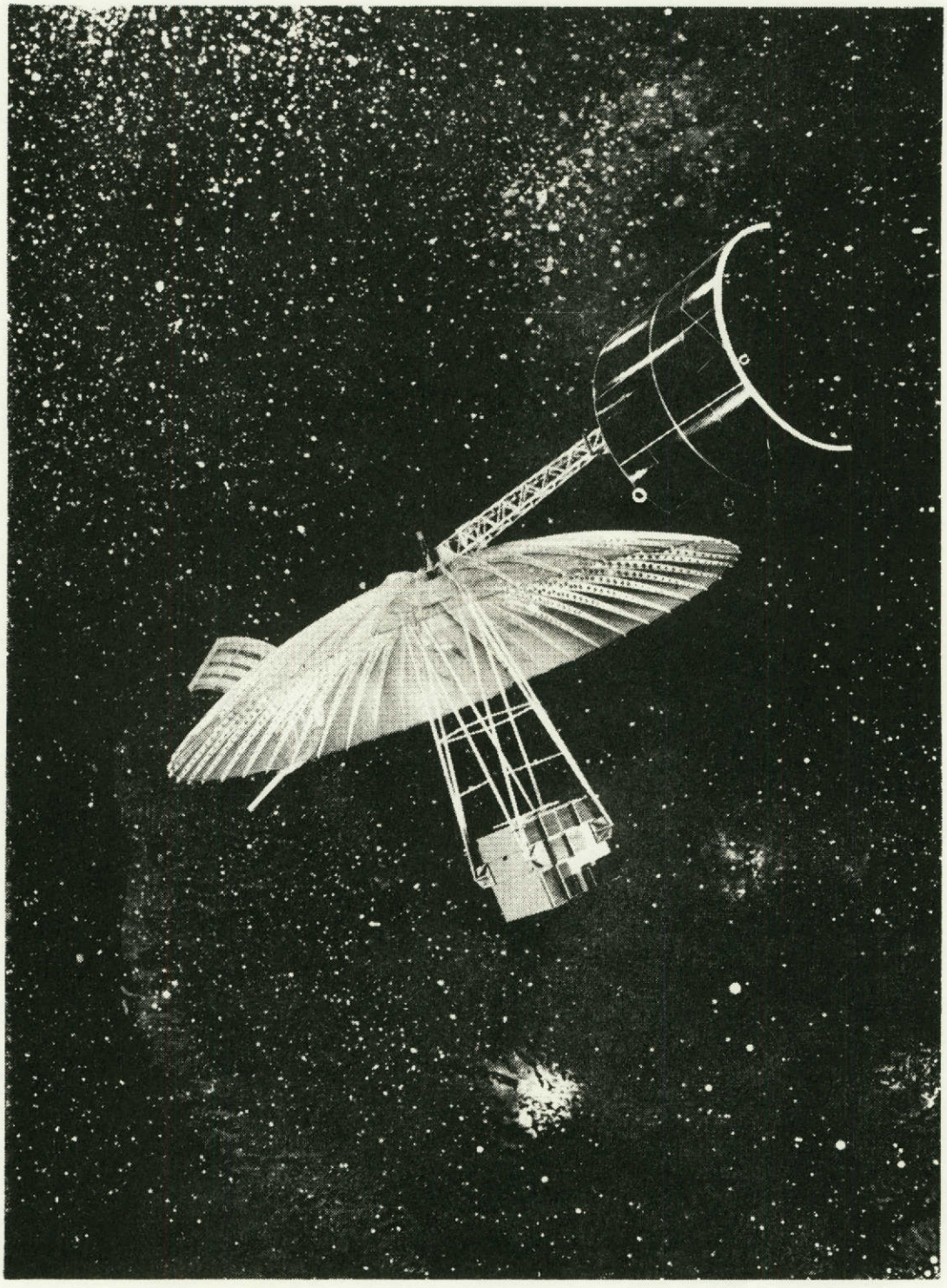

FINAL PROJECT REPORT FOR ELECTRON-PROTON SPECTROMETER

John R. Winckler
University of Minnesota

ABSTRACT

This document is the Final Project Report on the experiment fabrication phase of Contract No. NAS 5-11687 initiated 21 May 1969.

An electron-proton spectrometer was designed to measure the geomagnetically trapped radiation in a geostationary orbit at 6.6 earth radii in the outer radiation belt. This instrument is to be flown on the Applications Technology Satellite-F (ATS-F).

The electron-proton spectrometer consists of two permanent magnet-surface barrier detector arrays and associated electronics capable of selecting and detecting electrons in three energy ranges: 30-50 keV, 150-200 keV, and >500 keV and protons in three energy ranges: 30-70 keV, 70-170 keV, and 170-500 keV.

The electron-proton spectrometer has the capability of measuring the fluxes of electrons and protons in various directions with respect to the magnetic field lines running through the satellite. One magnet-detector array system is implemented to scan between EME north and south through west, sampling the directional flux in 15° steps. The other magnet-detector array system is fixed looking toward EME east.

The electron-proton spectrometer response to electrons was tested with an electron accelerator up to 125 keV and with Sr-90 and Pm-147 β-sources at higher energies. The response to protons was tested with a proton accelerator. Sr-90 and Pm-147 calibration source spectrums were determined and calibration coefficients for the electron-proton spectrometer were calculated.

TABLE OF CONTENTS

LIST OF FIGURES

LIST OF TABLES

I. BRIEF HISTORY OF THE RADIATION BELTS

The existence of a large flux of geomagnetically trapped radiation around the earth was discovered in early 1958 by Geiger counters flown on Explorers I and III by Professor J. A. Van Allen's group (Van Allen et al. (1958) and Van Allen (1960)). Later in 1958, data from Geiger counters and scintillation detectors on Soviet satellites Sputnik II and III (Vernov and Chudakov (1960)) and from Geiger counters on Explorer IV and Pioneer III (Van Allen and Frank (1959)) revealed a second belt of radiation in addition to the one first reported by Van Allen. These discoveries have led to the concept of an inner radiation zone between 1-2 R_e and an outer radiation zone between 3-4 R_e. The identity and energy distribution of the trapped radiation was still unknown at that time other than it consisted of charged particles. Also, the source and loss processes of the trapped radiation were not completely known.

The first experiment that unambiguously identified protons in the inner radiation zone was performed with a stack of nuclear emulsions by Freden and White (1959). This and later experiments revealed that the earlier instruments used by Van Allen responded mainly to protons with $E > 30$ meV in the inner zone. The population of outer zone protons was studied later by Davis and Williamson (1963) in the energy range $0.1 < E < 5$ meV with a scintillator and phototube on Explorer XII and again on Explorer XIV with the same instrument (Davis, Hoffman, and Williamson (1964)). These studies revealed that the proton fluxes in the measured energy ranges in the inner and outer radiation zones were quite stable in time. Later studies of the lower energy outer zone protons by Frank (1967), however, revealed that the flux of 3-50 keV protons increased considerably during geomagnetic storms.

Early measurements of the inner zone electron population are very fragmentary. Most early detectors did not discriminate between electrons and protons, and the large flux of inner zone protons dominated their response. Also, after July 9, 1962, a large flux of artificially injected electrons from the Starfish nuclear detonation obscured the natural electron population in the inner zone. O'Brien (1962a) summarizes the available data prior to Starfish. Many later experiments have measured the time decay of the artificial belt and the temporal variations of the natural electron population in the inner zone, including Bostrom et al. (1970) and Pfitzer (1968).

The outer zone electrons were first identified with a permanent magnet spectrometer flown on a sounding rocket by Cladis et al. (1961). Detectors on Explorer VI (Arnoldy, Hoffman, and Winckler (1960)) and on Explorer XIV (Frank, Van Allen, and Hills (1964)) plus many other experiments have found that outer zone electrons are quite variable in time and that fluxes can change by orders of magnitude in hours.

Several sources of inner zone particles have been suggested. Neutron albedo decay, in which an incoming cosmic-ray proton suffers a collision in the earth's atmosphere with oxygen and nitrogen nuclei and produces a neutron that emerges into space and decays into an electron and proton, has been suggested to be an important inner zone source (Hess, 1968). Studies by Pfitzer and Winckler (1968) and Bostrom et al. (1970) indicate that inner zone electrons (<690 keV and <1 meV respectively) are injected deep into the inner zone during a major geomagnetic storm and diffuse inward both during and after a geomagnetic storm. Nakada and Mead (1965), assuming that the solar wind was the source of protons, calculated that the cross-field inward radial diffusion was the dominant process in controlling the outer zone protons. Measurements of the outer zone protons between 0.17 and 3.4 MeV by Mihalov and White (1966) likewise support the idea that the source of outer zone protons is inward radial diffusion. Recently, measurements by Frank (1970) indicate that low energy protons are injected into the outer zone near local midnight during magnetospheric substorms, establishing an extraterrestrial ring current.

In an early study of outer zone electrons with energies >40 keV, Frank, Van Allen and Hills (1964) suggested that inward radial diffusion was a source of electrons after a geomagnetic storm. Observations by Winckler's group (Winckler, 1969) using electron spectrometers on OGO III and ATS I have shown that the polar substorm as described by Akasofu (1968) plays a fundamental role in the injection, modulation, and distribution of energetic electrons in the outer and inner radiation belts. From his measurements of precipitated electrons with energies >40 keV on the polar orbiting Injun I and III, O'Brien (1962b, 1962c, 1964) hypothesized the "splashcatcher" model of the outer radiation zone. In this model, a fraction of the electrons from the same acceleration mechanism are caught in the outer zone concurrently with large precipitated fluxes of electrons and aurora.

Several loss processes have been suggested. In the inner zone, high energy protons are removed by slowing down from interaction with the atmosphere until their energies are reduced to 100 keV (Hess, (1968)). Below 100 keV, charge exchange, in which fast protons are turned into fast neutrons, becomes the dominant loss process. Inelastic nuclear collisions is the most important loss process for protons above 200-300 meV. In the outer zone, additional processes, probably involving non-adiabatic effects such as time varying electric and magnetic fields or various plasma instabilities, are also a cause of loss of protons. Different loss processes are operative for electrons. In the inner zone, coulomb scattering into the loss cone is the principal process (Hess, (1968)). In the outer zone, various causes involving magnetic disturbances such as whistlers have been suggested for the electron precipitation.

II. PURPOSE OF EXPERIMENT

An experiment for use on the Applications Technology Satellite -F (ATS-F) was proposed by Dr. John R. Winckler to investigate the origin of the outer Van Allen trapped radiation belt. This experiment would help to clarify the mechanism involved in accelerating electrons and protons into the trapping region. The experiment consists of measurements of the intensity and time variations of electrons and protons at synchronous orbit. These measurements will then be analyzed in their relationship with magnetic storms and substorms and other perturbations of the magnetosphere. An on-board magnetometer which measures the magnetic field vector at the satellite will allow pitch angle calculations to be made. Other magnetic field data are available from various ground stations.

A similar experiment was successfully carried out on the ATS-1 satellite by Lezniak and Winckler (1970) using only an electron spectrometer which detected electrons in the energy range 50-1000 keV. Their observations show that electrons in the energy range 50-200 keV are injected into the magnetosphere at synchronous orbit in the vicinity of local midnight during magnetospheric substorms. From their data, Lezniak and Winckler (1970) propose a model of electron (and proton) acceleration and injection into the magnetosphere just prior to a substorm and a substorm-associated, rapid, convective surge collapse of the geomagnetic field lines east of a "fault line" near local midnight carrying with them and heating the magnetotail plasma.

More recently, DeForest and McIlwain (1971) have measured the electron and proton fluxes in the energy range 50 eV-50 keV at synchronous orbit on the ATS-5 satellite. Their observations confirm the earlier findings of Frank (1967, 1970) of the injection and dispersion of the electrons and protons in this energy range. However, the ATS-5 satellite has an advantage of being in synchronous orbit (which is almost always in the outer radiation belt) as compared to the earlier measurements made on satellites which passed rapidly through the radiation belts and then only every day or so. As a result, the data from the electron and proton spectrometers on ATS-5 show stronger local time dependence and even greater structure in the energy spectra than before.

From the ATS-5 data, DeForest and McIlwain (1971) conclude that the magnetospheric substorms correspond to a sudden intensification of the east-west electric fields in a narrow sector near midnight, that the enhanced electric fields move particles from the plasma sheet deep into the magnetosphere, that these electric fields decrease in time, and that its decrease cuts off the flow of particles to the inner regions. They conclude that this injected "cloud" of plasma follows radically different paths of dispersion owing to magnetic field gradient and curvature contributions to the drift velocity, which is dependent on energy, charge and pitch angle. They state that the injection and dispersion of the high-energy tail of these plasma clouds

agree with the observations of Lezniak and Winckler (1970). Their observed injection of energetic protons which drift westward after injection agrees with the observations of "asymmetric ring current" protons reported by Frank (1970).

The experiment for the ATS-F satellite is a unique extension of these previous studies including measurements from both an electron and proton spectrometer and including higher energy ranges than the electron and proton spectrometers on ATS-5. Three separate energy ranges of electrons will be measured: 30-50 keV, 150-200 keV and >500 keV. For protons, the energy ranges are 30-70 keV, 70-170 keV, and 170-500 keV. These proton energy ranges cover the predominant proton population in the outer zone and the lower energy range includes the protons which constitute a significant portion of the extra-terrestrial ring current (Frank, 1967). The electron response covers the "energetic" range injected during substorms and is similar to the energy range responsible for ionospheric absorption and auroral X-rays up to the relativistic electrons in the stable trapped radiation. The "narrow band" energy windows give better defined energies for observing particle drift effects.

The electron-proton spectrometer is capable of counting low count rates such as 1 or 2 counts per sample. Thus, long term averages of these low count rates are meaningful. The lowest energy electron and proton channels have a sampling rate of 8/second. Therefore, time variations in these energy ranges can be detected up to a maximum frequency of 4/second. This will allow for the establishment, in a more direct manner, of the existence or nonexistence at the geo-stationary orbit of certain rapidly varying electron fluxes commonly observed in precipitated fluxes.

The directional capabilities of the electron-proton spectrometer and the measurement of the magnetic field vector at the satellite by an onboard magnetometer will allow the pitch angle distribution characteristics of electrons and protons to be studied. The pitch angle distribution study permits one to establish whether the acceleration of these particles occurs by the Fermi mechanism (enhancement of $\vec{V}$ parallel), or by the betatron process (enhancement of $\vec{V}$ perpendicular), or by stochasti processes, for example, strong pitch angle diffusion, which tends to make the pitch angle distribution isotropic, and which may occur during precipitation and continually feed particles into the loss cone.

The electron-proton spectrometer will also allow more precise studies of the dynamic variables that may be affected in the transit of electrons and protons from the equator to the auroral zone through correlation with ground, balloon, and rocket experiments near the conjugate point of the geomagnetic field line passing through the satellite.

These studies of magnetospheric dynamics are related to the recent Electron Echo rocket experiment studies performed by Hendrickson, McEntire and Winckler (1971) involving controlled injection of electrons into the magnetosphere. It may be possible to detect these electrons at synchronous orbit after injection from a rocket at low latitude.

III. SATELLITE INFORMATION

The ATS-F satellite will be launched into a geostationary equatorial circular orbit at 6.6 earth radii. The ATS-F mission specifications call for the spacecraft to be positioned for the first year at 94° west longitude (over the United States), to be repositioned in a 41 day maneuver to 35° east longitude (over Africa) and remain there for one year, and then to be repositioned to 94° west longitude again (Goddard Space Flight Center, (1971)). These mission specifications call for an orbit inclination to the equatorial plane of 2.0 degrees maximim. The spacecraft will be stabilized by an attitude control system consisting of sun, earth, and Polaris sensors and momentum wheels and jet torquers. Figure 1 shows an artist's conception of the ATS-F satellite in orbit and Figure 2 shows the orientation of the satellite with respect to the earth.

The University of Minnesota electron-proton spectrometer is one of eight scientific instruments mounted on the environmental measurements experiment (EME) package. The EME package is mounted at the base of the 30-foot parabolic reflector on the outboard side of the reflector hub as is shown in Figure 3. The EME is rotated 13 degrees about the spacecraft Z-axis in order to align the package with the nominal direction of the magnetic field lines at the 35° east longitude position (Westinghouse Operations Manual, EME Mission-F Revised September 24, 1971). Figure 4 shows the coordinate system for the EME. The elctron-proton spectrometer orientation is given in Figure 5, in terms of the EME coordinates. One particle detection system of the electron-proton spectrometer is fixed with a look direction toward EME east and tilted 6-1/2° in the anti-earth direction. The other particle detection system is a scanning system with 13 look directions spaced in 15° steps from EME north to south through west. The mechanical scanning mechanism (to allow pitch angle distribution studies) was required because the satellite is not spinning with respect to earth-fixed coordinates. The positioning at 35° east longitude will allow correlations with ground, balloon, and rocket observations based at Kiruna, Sweden, which is near the conjugate point of the magnetic field line passing through the satellite.

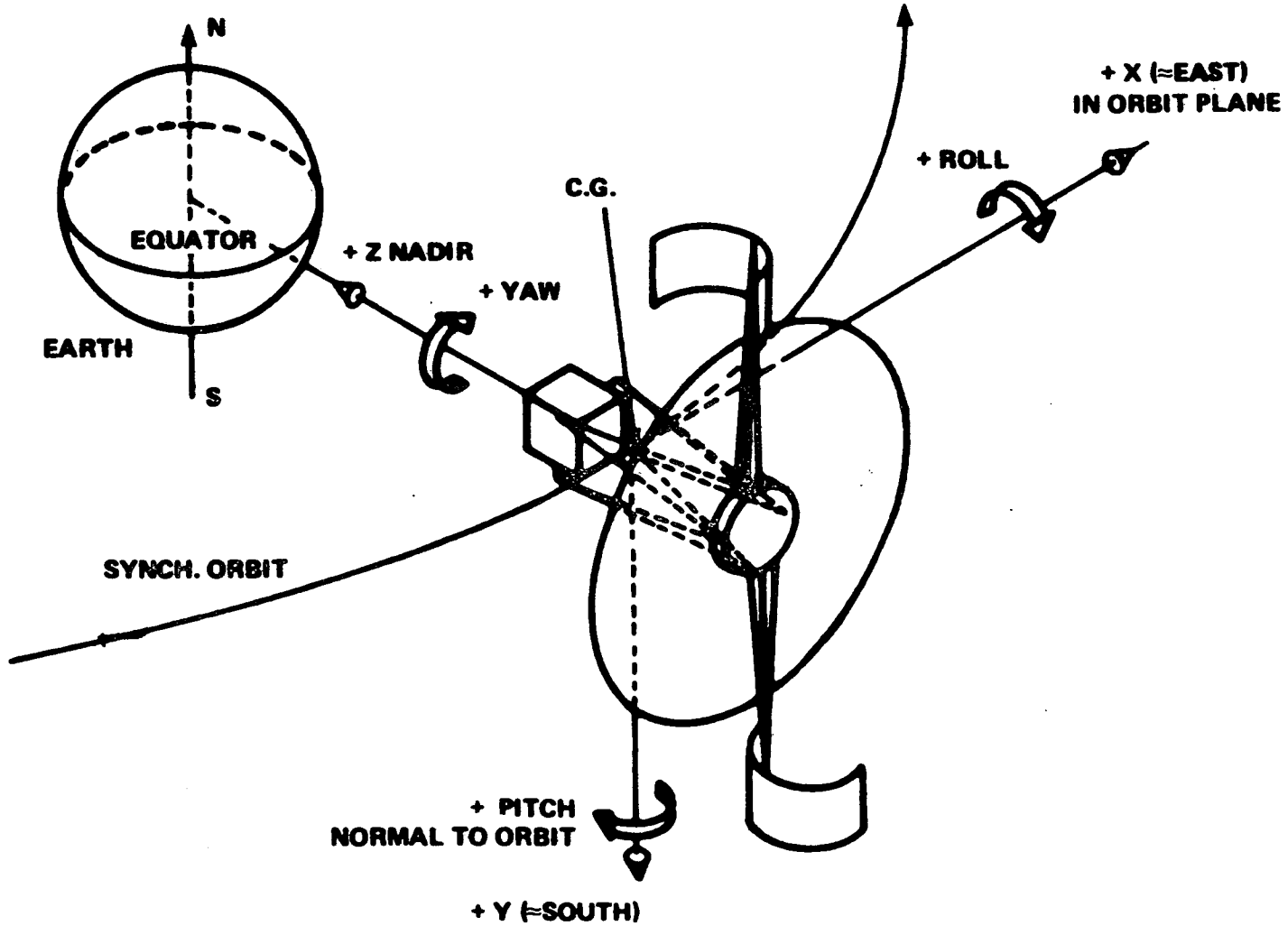
N
EQUATOR
EARTH
S
+ Z NADIR
+ YAW
C.G.
+ ROLL
+ X (≈EAST)
IN ORBIT PLANE
SYNCH. ORBIT
+ PITCH
NORMAL TO ORBIT
+ Y (≈SOUTH)

Figure (2)

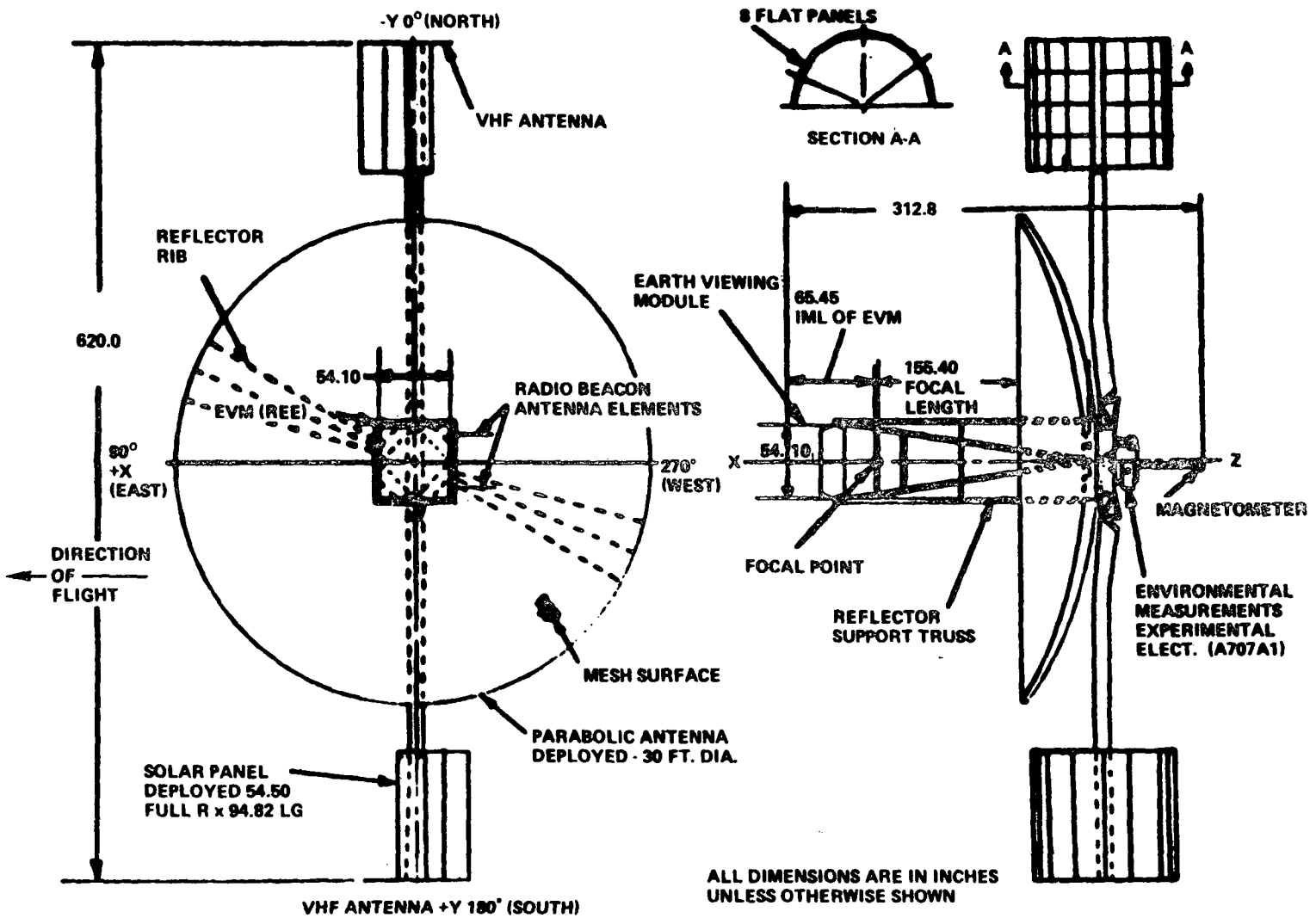
-Y 0° (NORTH)
VHF ANTENNA
REFLECTOR RIB
620.0
54.10
EVM (REE)
RADIO BEACON ANTENNA ELEMENTS
90° +X (EAST)
270° (WEST)
DIRECTION OF FLIGHT
MESH SURFACE
PARABOLIC ANTENNA DEPLOYED - 30 FT. DIA.
SOLAR PANEL DEPLOYED 54.50 FULL R x 94.82 LG
VHF ANTENNA +Y 180° (SOUTH)
8 FLAT PANELS
SECTION A-A
312.8
EARTH VIEWING MODULE
65.45 IML OF EVM
155.40 FOCAL LENGTH
54.10
X
Z
MAGNETOMETER
FOCAL POINT
REFLECTOR SUPPORT TRUSS
ENVIRONMENTAL MEASUREMENTS EXPERIMENTAL ELECT. (A707A1)
ALL DIMENSIONS ARE IN INCHES UNLESS OTHERWISE SHOWN

Figure (3)

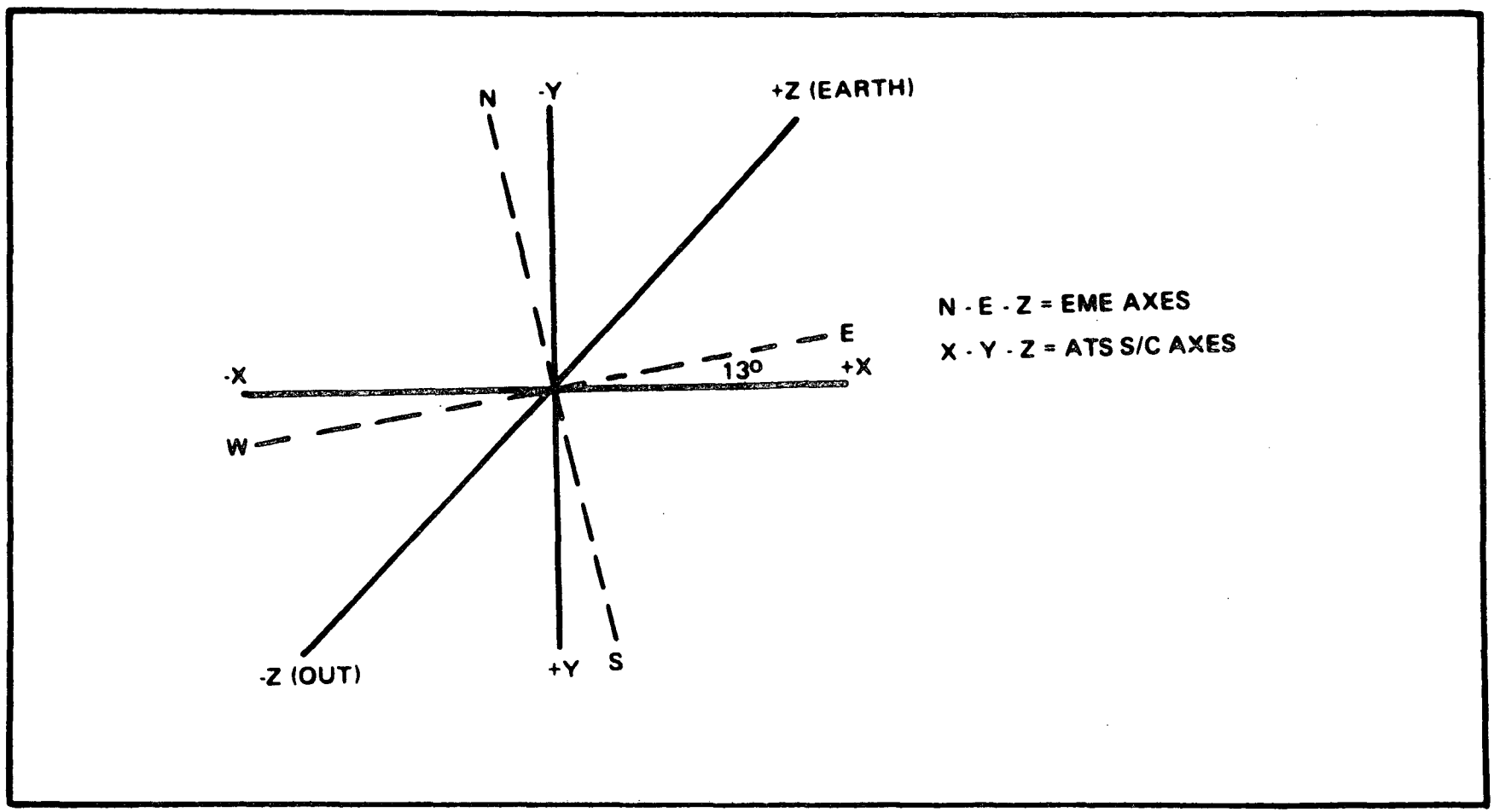

Figure (4)

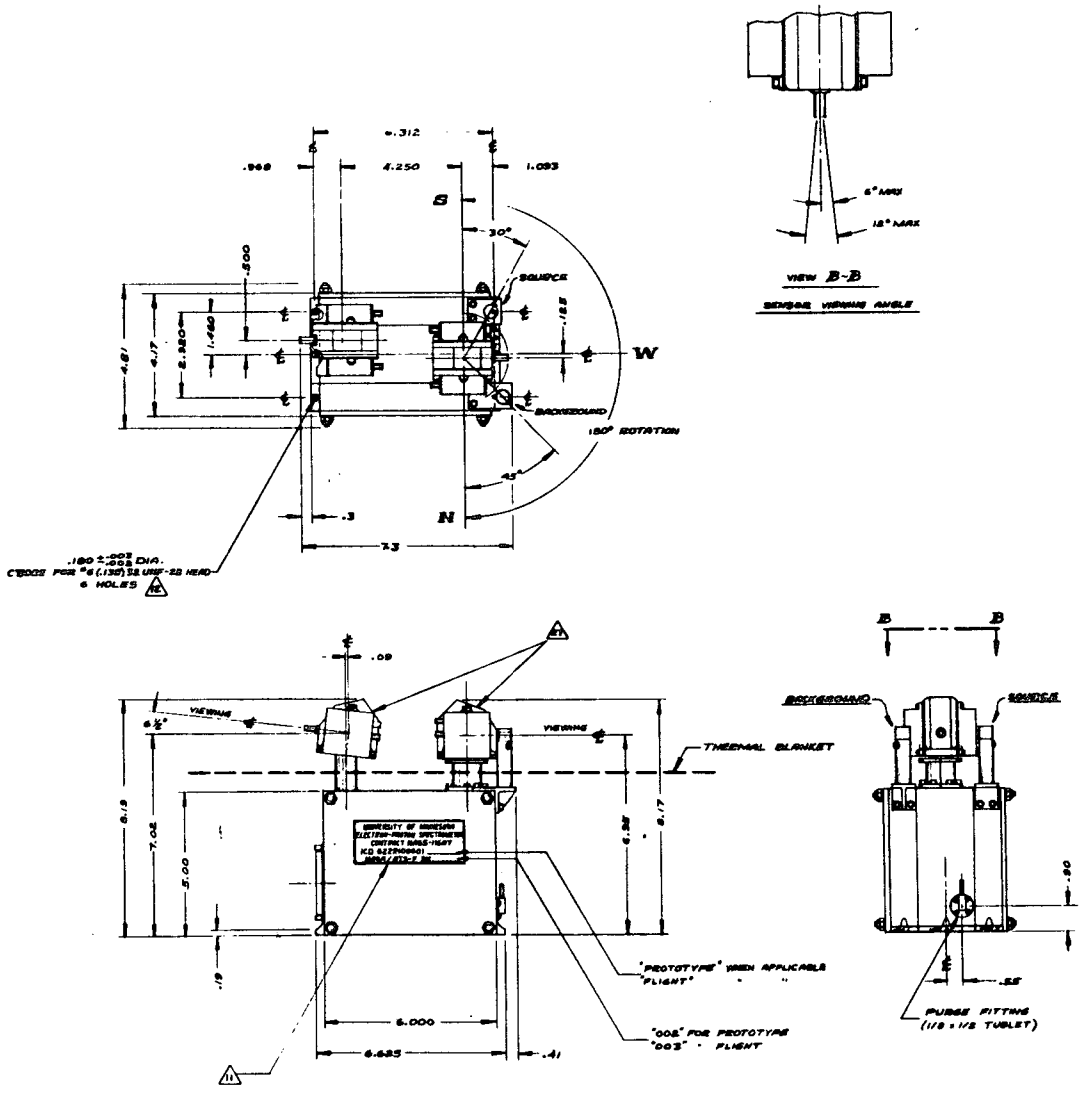
.312
.968
4.250
1.093
S
30°
SOURCE
W
BACKBOARD
180° ROTATION
45°
N
.3
7.3
VIEW B-B
SENSOR VIEWING ANGLE
6° MAX
18° MAX
THERMAL BLANKET
PROTOTYPE WHEN APPLICABLE
FLIGHT
.005" FOR PROTOTYPE
.002" FLIGHT
6.000
6.625
PURGE FITTING
(1/8 x 1/2 TUBE)

Figure (5)

IV. THE ELECTRON-PROTON SPECTROMETER

The electron-proton spectrometer consists of two identical particle detection systems, each capable of measuring the directional flux of electrons in the energy ranges: 30-50 keV, 150-200 keV, and >500 keV and protons in the energy ranges: 30-70 keV, 70-170 keV, and 170-500 keV. The twelve electron and proton energy channels are labeled as in Table I. The energies for electrons are determined by magnetic deflection and pulse height analysis in the two lower energy channels. Electrons of energy >500 keV are not appreciably deflected and are detected by two counters in coincidence, in line with the entrance aperture. The first of these two also detects protons by pulse height analysis. One particle detection system is fixed with a look direction toward EME east and tilted 6-1/2° in the anti-earth direction. The other particle detection system is a scanning system with 13 look directions spaced in 15° steps from EME north to south through west and not tilted, but lies in the EME N-E plane. The particle directional flux will be averaged over an acceptance solid angle consisting of a cone of approximately 5° semi-angle. The same type of collimator will be used for all particle types and energy ranges.

The magnetic deflection system consists of a permanent magnet and soft iron cup-core type yoke. Ortec gold-silicon surface barrier detectors arranged in an array around the permanent magnet pole faces are used to detect the electrons and protons in all of the energy ranges. (See Figure 6). The complete specifications of the surface barrier detectors are given in Table III in Section V. The two magnet-detector array systems, each with four Ortec gold-silicon surface barrier detectors and four preamplifiers mounted on the outside of the soft iron yoke, are mounted on stainless steel shafts several inches above the approximately 4" x 6" x 5" main electronics package of the electron-proton spectrometer. These magnet-detector array systems will extend outside of the thermal blanket of the spacecraft and will thus be passively cooled. Figure 5 shows the mechanical drawing of the electron-proton spectrometer and the position of the thermal blanket. Figure 7 shows the assembled flight model electron-proton spectrometer and Figure 8 shows a breakdown of the sections of the main electronics package of the flight model electron-proton spectrometer. The flight model electron-proton spectrometer weighs 6.649 pounds.

The scanning mechanical system consists of the following main components as labeled in Figure 9: (A) stepper motor, (B) tubular, stainless steel shaft (extending out of the scanning mechanism housing and supporting the scanning magnet-detector system), (C) scanning mechanism housing, (D) two pairs of preloaded bearings (hidden from view), and (E) a flexible coupling between the shaft and stepper motor - gear drive system. For a more detailed description of the scanning mechanical system and its design considerations, see Appendix I.

TABLE I

ELECTRON-PROTON SPECTROMETER ENERGY CHANNELS*

	Scanning System	Fixed System	Energy Range (kev)**
	E11	E12	30-50
Electrons:	E21	E22	150-200
	E31	E32	>500
	P11	P12	30-70
Protons:	P21	P22	70-170
	P31	P32	170-500

** Nominal values for prototype and flight models.

* Explanation of Subscript System:

The "E" or "P" designates electron or proton channel respectively. The first subscript ("1", "2", or "3") following one of these letters designates the energy channel. The second subscript ("1" or "2") designates the scanning or fixed magnet-detector system, respectively. The three electron channels are labeled to correspond with three different Ortec surface barrier detectors and all three proton channels are associated with one Ortec surface barrier detector, as shown in Figure 6. Thus, for example, the E21 energy channel is the 150-200 keV electron channel corresponding to the electron detector #2 (E2) in the scanning magnet-detector system.

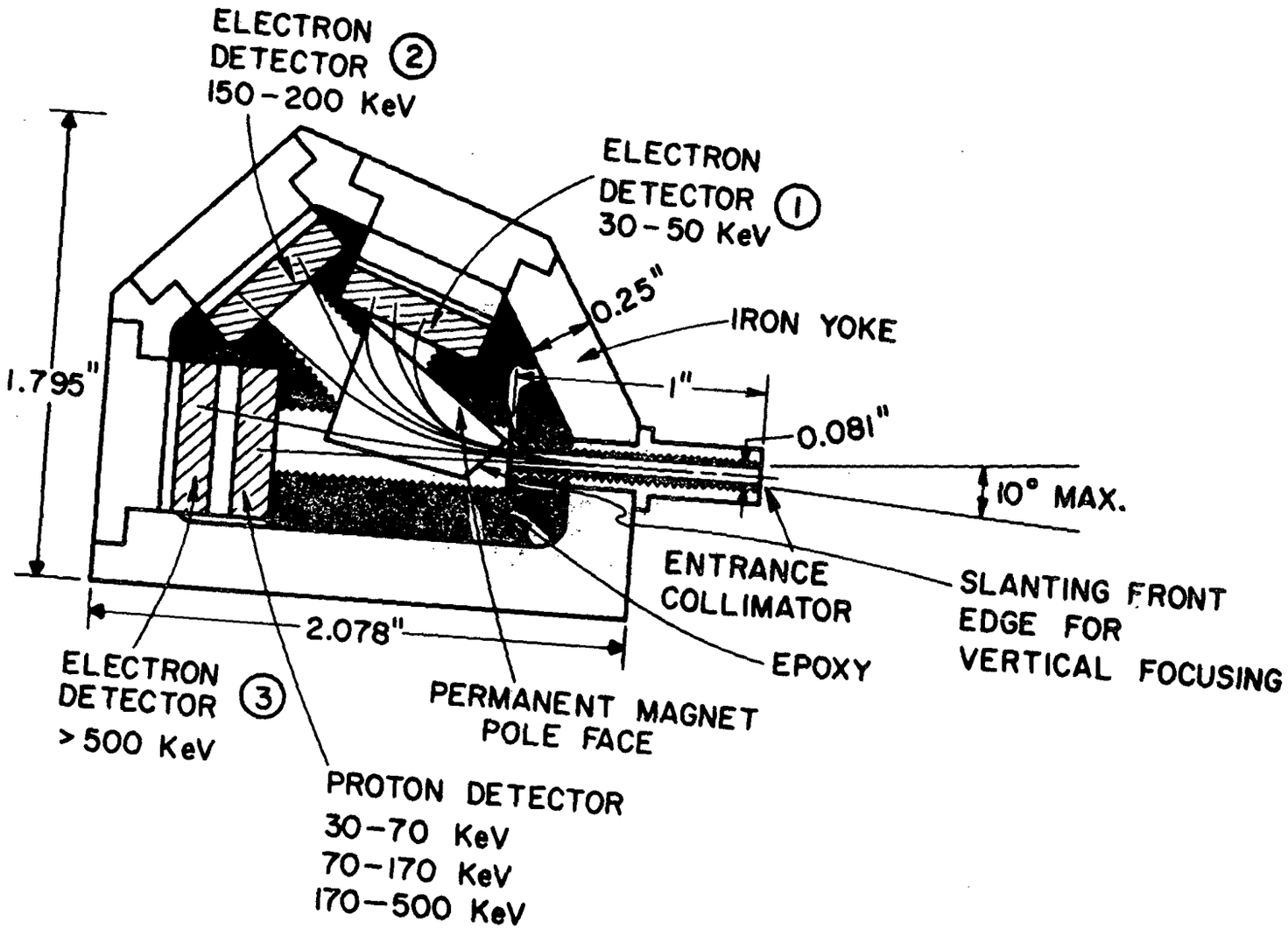
ELECTRON
DETECTOR (2)
150 – 200 KeV
ELECTRON
DETECTOR (1)
30 – 50 KeV
0.25"
IRON YOKE
1.795"
1"
0.081"
10° MAX.
ENTRANCE
COLLIMATOR
SLANTING FRONT
EDGE FOR
VERTICAL FOCUSING
2.078"
EPOXY
ELECTRON
DETECTOR (3)
> 500 KeV
PERMANENT MAGNET
POLE FACE
PROTON DETECTOR
30 – 70 KeV
70 – 170 KeV
170 – 500 KeV

Figure (6)

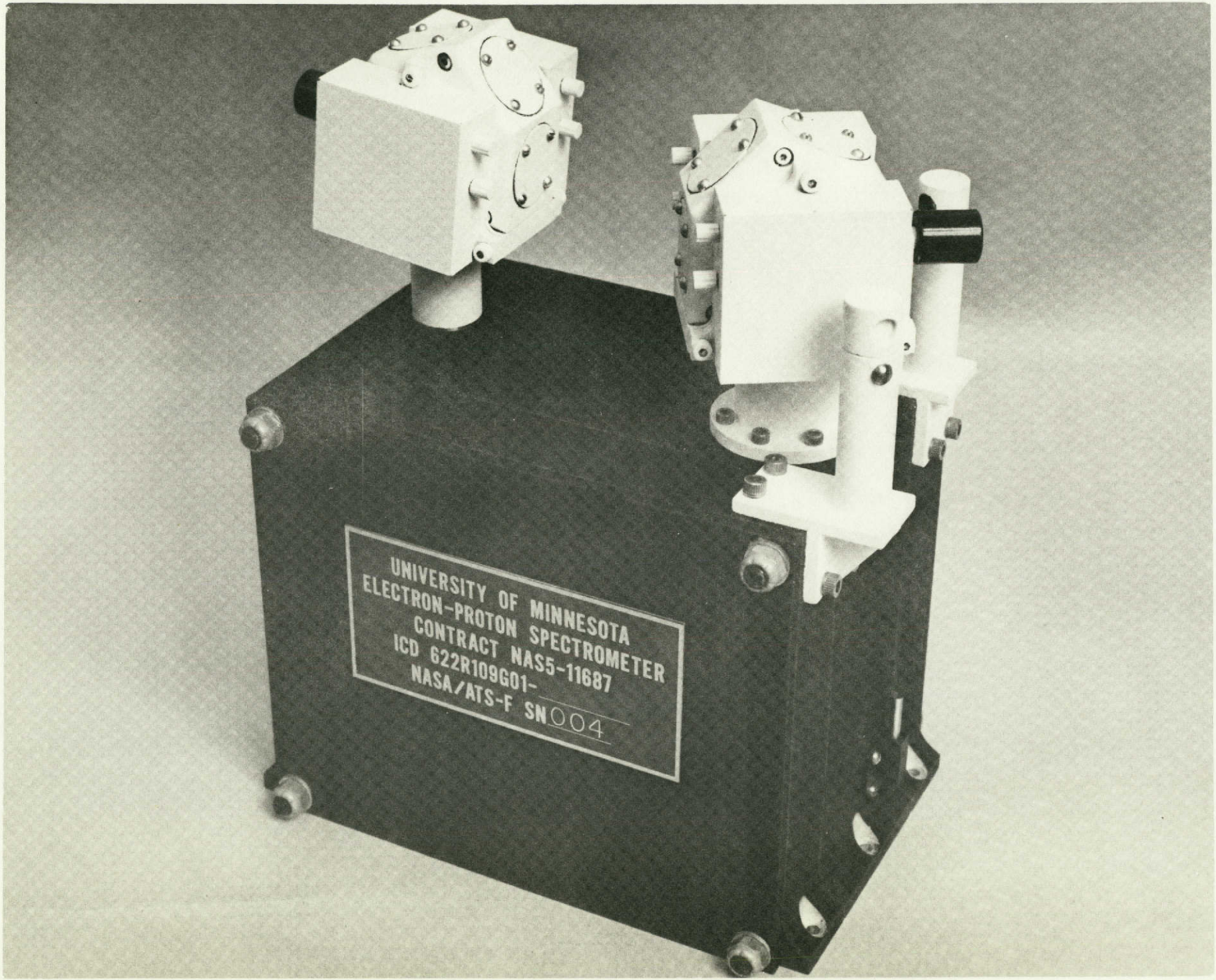
UNIVERSITY OF MINNESOTA
ELECTRON-PROTON SPECTROMETER
CONTRACT NAS5-11687
ICD 622R109G01-
NASA/ATS-F SN004

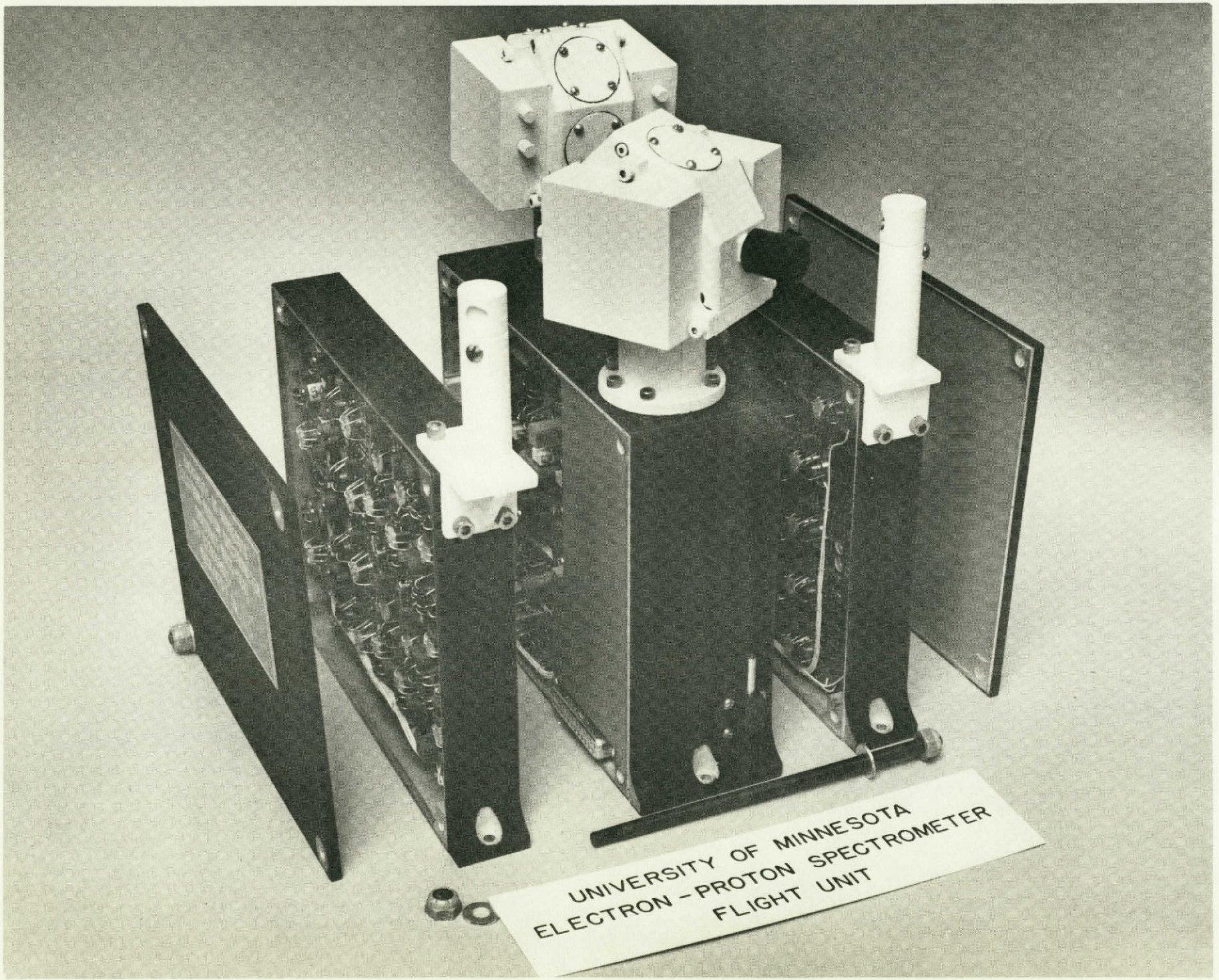
UNIVERSITY OF MINNESOTA
ELECTRON - PROTON SPECTROMETER
FLIGHT UNIT

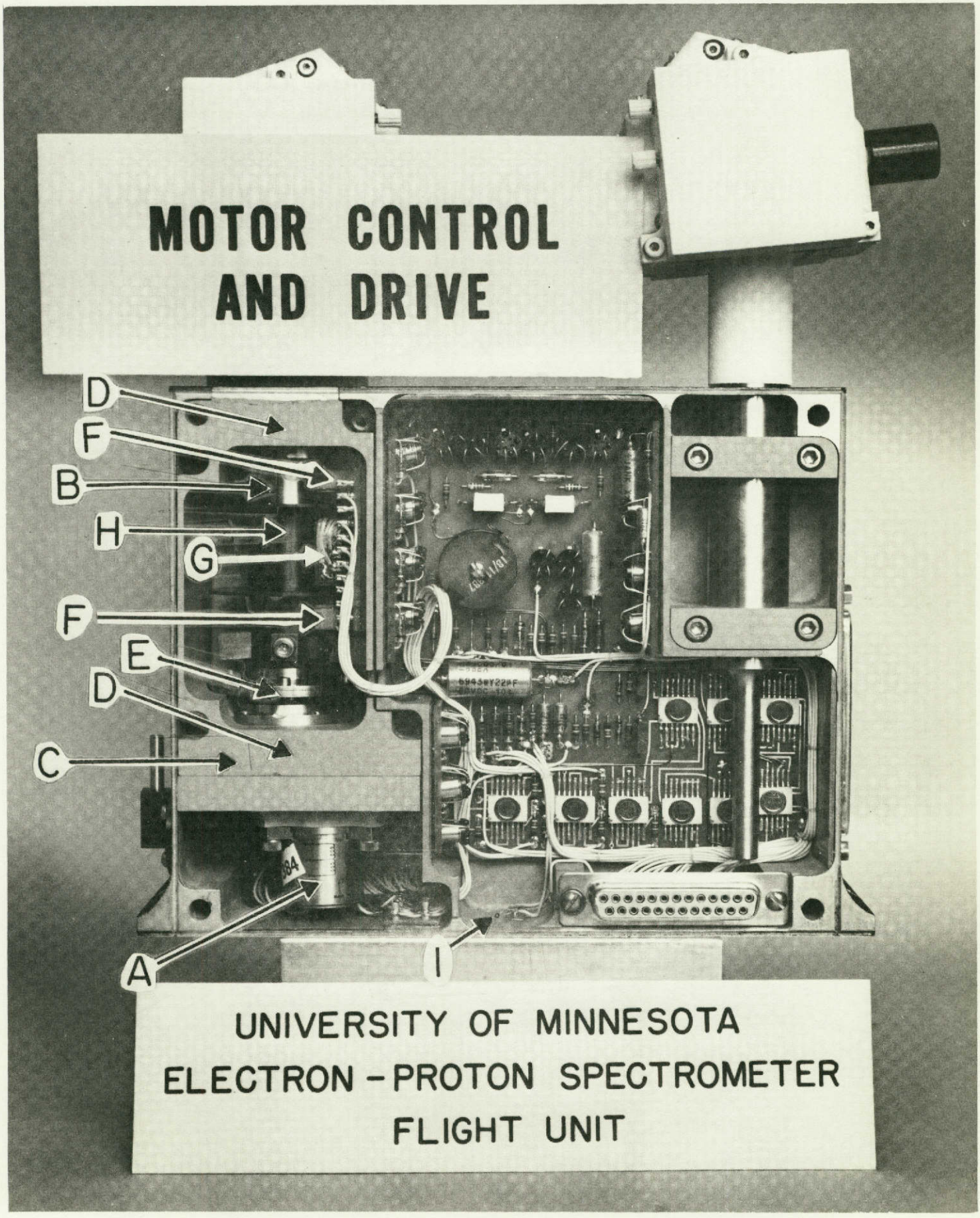
MOTOR CONTROL
AND DRIVE
D
F
B
H
G
F
E
D
C
A
I
UNIVERSITY OF MINNESOTA
ELECTRON - PROTON SPECTROMETER
FLIGHT UNIT

The position of the scanning detector is detected by an optical encoder system consisting of the following main components shown in Figure 9: (F) lamps, (G) light sensors, and (H) an encoder spool attached to the shaft. The shaft encoder system reads out in four bi-level signals from which the look directions of the scanning detector system can be interpreted. The shaft encoder system also senses the north and south limits of the scanning detector system's range and provides the signal to reverse the stepping direction. The nominal look directions and corresponding shaft encoder readouts of the scanning detector system are given in Table II. A calibration of the scanning detector position in 1^{o} increments versus the shaft encoder binary readout is given for the prototype model in Table IX in Section VIII of this paper. This more detailed calibration gives the exact limits of each coded sector and reveals some coding irregularities.

At the position 45^{o} from EME north and west, the scanning detector system looks at a brass plug which prevents the trapped radiation from entering the detector system. Thus, the background determination is made at this position. At the position 30^{o} from EME south and 60^{o} from EME west, the scanning detector system looks at the Strontium (Sr-90) and Promethium (Pm-147) in-flight calibration source.

The electron-proton spectrometer is operated in flight by the application of +28 volts DC to the appropriate terminals in the spacecraft connector and by counting for suitable periods the positive, ten-volt, two microsecond pulses emitted on the twelve output terminals in the same connector corresponding to the twelve energy channels. For proper operation with protons and electrons, the instrument should be at a pressure of no greater than 10^{-5} Torr.

Three thermistor circuits are provided so that voltages observed on the appropriate three spacecraft connector terminals may be interpreted as temperature indications. One thermistor is located in one of the preamplifier boxes of each magnet-detector array system and the third one is located inside the main electronics package. (See (I), Figure 9).

A block diagram of the electronic data systems and associated systems is shown in Figure 10.

All additional information concerning the electron-proton spectrometer interface with the satellite including specific telemetry identification of all of the instrument's outputs beyond that shown in Figure 10 or given in this document which are necessary for complete interpretation of the data is given in the Westinghouse Operations Manual, EME Mission-F (Revised 24 September 1971).

TABLE II

NOMINAL LOOK DIRECTIONS OF THE

SCANNING DETECTOR SYSTEM

Shaft Encoder Binary Readout	Scanning Detector Position (EME Coordinates)
0000	North
0001	345°
0010	330°
0011	Background 315°
0100	300°
0101	285°
0110	270°
0111	255°
1000	240°
1001	225°
1010	Cal. Source 210°
1011	195°
1100	South
1101	N/A
1110	N/A
1111	N/A

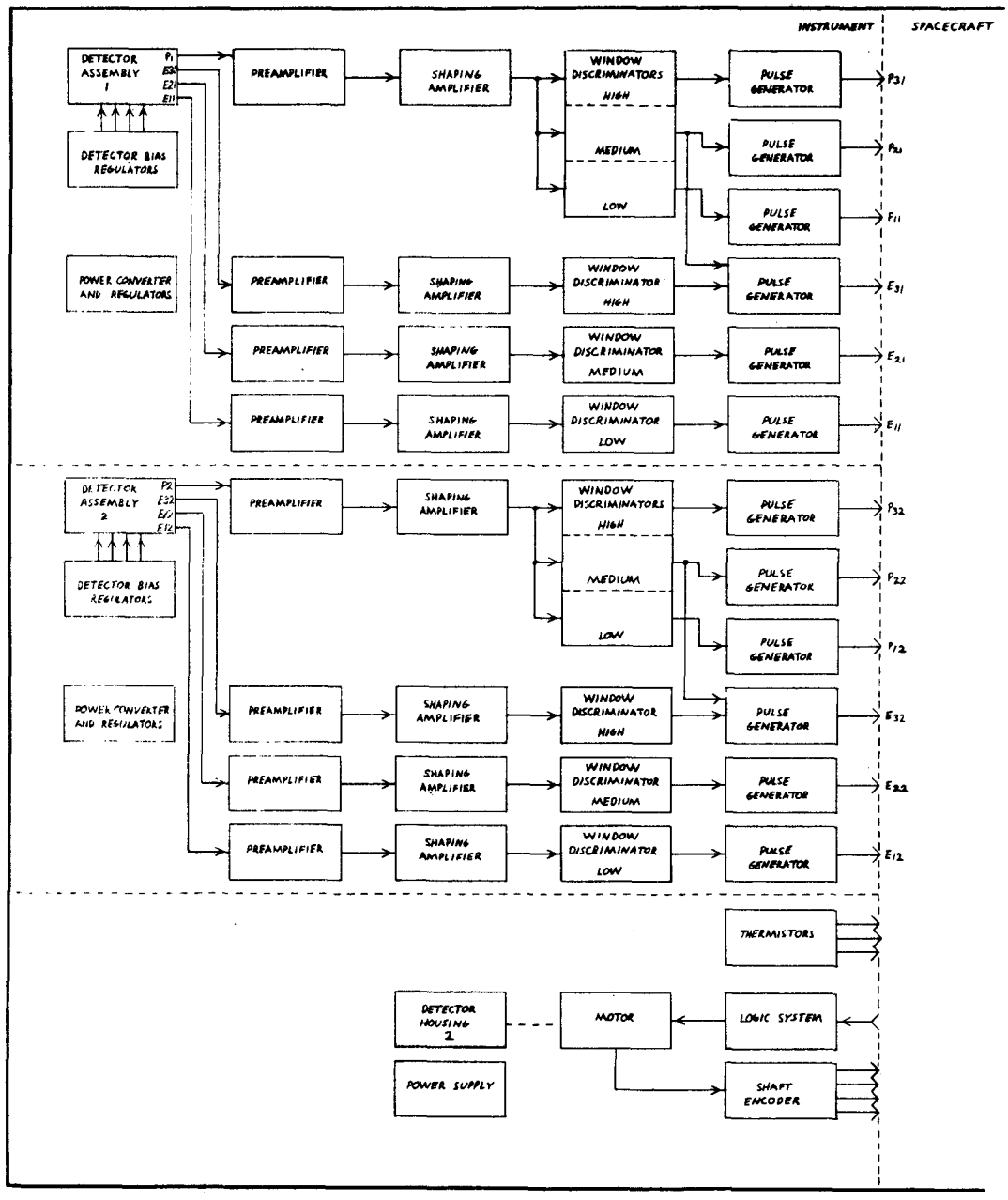
INSTRUMENT
SPACECRAFT
DETECTOR ASSEMBLY 1
DETECTOR BIAS REGULATORS
POWER CONVERTER AND REGULATORS
PREAMPLIFIER
SHAPING AMPLIFIER
WINDOW DISCRIMINATORS HIGH
MEDIUM
LOW
WINDOW DISCRIMINATOR HIGH
WINDOW DISCRIMINATOR MEDIUM
WINDOW DISCRIMINATOR LOW
PULSE GENERATOR
DETECTOR ASSEMBLY 2
DETECTOR BIAS REGULATORS
POWER CONVERTER AND REGULATORS
THERMISTORS
DETECTOR HOUSING 2
MOTOR
LOGIC SYSTEM
POWER SUPPLY
SHAFT ENCODER

Figure (10)

V. SURFACE BARRIER PARTICLE DETECTORS

A. Description

The decision to use surface barrier particle detectors was based on the initial goal to detect electrons and protons in the energy range as low as 20-50 keV. Scintillation particle detectors as used on ATS-1 have a lower energy detection limit of approximately 50 keV. However, state-of-the-art surface barrier detectors operated at temperatures below -10°C and with state-of-the-art preamplifiers are capable of resolving electrons with energies as low as approximately 15 keV.

The Ortec gold-silicon surface barrier detector is a large area diode formed by a rectifying junction between gold and silicon. It is known that a potential barrier exists at the intimate junction of a metal and a semiconductor. This electrostatic potential difference (the barrier height) is established when the electrons in the metal and the semiconductor seek an equilibrium level characterized by the Fermi energy level becoming the same throughout both solids. The potential will be established by the diffusion of charge carriers across the junction in a manner similar to that at p-n semiconductor junction. A further description of p-n semiconductor junctions can be found in Melissinos (1968), Dearnaley and Northrop (1966), and Bertolini and Coche (1968).

The conventional p-n semiconductor junction is well understood and easily manufactured. The manufacture of surface barrier detectors, however, involves certain processes which result in good surface barriers but which cannot be readily explained. A surface barrier detector is made from an n-type slab of silicon. One surface is oxidized by exposure to air at room temperature forming an approximately 70 Angstrom layer of p-type silicon oxide on the much thicker n-type silicon slab. Apparently, better surface barriers are formed if this oxidized layer is exposed to water vapor. Then, a 40 $\mu g\text{-}cm^{-2}$ layer of gold is deposited onto the oxidized silicon layer forming a rectifying contact. Some experiments (Bertolini and Coche, (1968)) have shown that the rectification occurs only after a period in oxygen or air after the gold deposition. It is generally agreed that some aging process takes place after the deposition of the gold. Whether this is a continuation of the surface treatment of the silicon as before the gold evaporation or an ionic rearrangement in the oxide layer is not known. The exact nature of this surface barrier is not completely understood, but it is clear that the absorbed layers from the exposure to oxygen and water vapor are very important in order to make a very good junction. The electrical contact to the other side of the n-type silicon is made by a 40 $\mu g\text{-}cm^{-2}$ or thicker layer of non-rectifying aluminum.

The surface barrier particle detector is analogous to an ionization chamber, but with the gas replaced by a semiconducting solid. When an

ionizing particle (electron or proton) enters the silicon, it creates free electron-hole pairs by losing energy at a mean rate of 3.6 electron volts (eV) per electron-hole pair. These free charges in the silicon must then be collected before they recombine. This charge collection is accomplished by the application of an electric field in the silicon.

In silicon surface barrier detectors, the electric field in the silicon is the result of the application of a reverse bias across the gold-silicon junction. The gold side is biased negatively with respect to the aluminum side. The electric field created in the silicon by reverse biasing the junction extends from the junction throughout a volume called the "depletion zone". (See Figure 11). The thickness of the depletion zone is proportional to the square root of the reverse bias voltage. If an electron-ion pair is created in the depletion zone, the electric field is such to accelerate the electron and the hole in opposite directions so that they are collected at the electrodes. Thus, the electron-ion pair are separated before they can recombine, and a good collection efficiency is achieved. All surface barrier detectors in the electron-proton spectrometer have a depletion zone extending throughout the volume of the detector from the gold to the aluminum contact and, thus, are said to be totally depleted.

The silicon surface barrier detectors are well suited for space experiments in that they are very small compared with ion chambers or with the phototubes necessary for scintillation counters. The silicon surface barrier detector also does not require the high voltage necessary for operation of the phototube. The silicon surface barrier detector does not have to be cooled to liquid nitrogen temperatures such as is necessary for germanium semiconductor detectors in order to have good energy resolution. The silicon surface barrier detectors also offer better energy resolution than is possible with diffused junction semiconductor detectors because the high temperatures necessary for manufacturing diffused junction detectors lead to a reduction of minority carrier lifetime which results in an increase in current noise. They are in addition much less susceptible to radiation damage than lithium-drifted semiconductor detectors. Their disadvantages compared with non-semiconductor type detectors are that the signals are quite small, requiring highly sophisticated low-level preamplifiers, and that noise is generated in the detector itself which can restrict the lower limit of detectable particle energies.

B. Noise and Resolution Considerations

There are several sources of electronic noise in the surface barrier detector-preamplifier circuit which affect the ultimate resolution of the detector system. The most important types of electronic noise present are thermal or Johnson noise of the preamplifier and input resistors, and current noise of the detector.

First, thermal or Johnson noise will be discussed. Thermal noise

SCHEMATIC OF TYPICAL

SURFACE BARRIER DETECTOR *

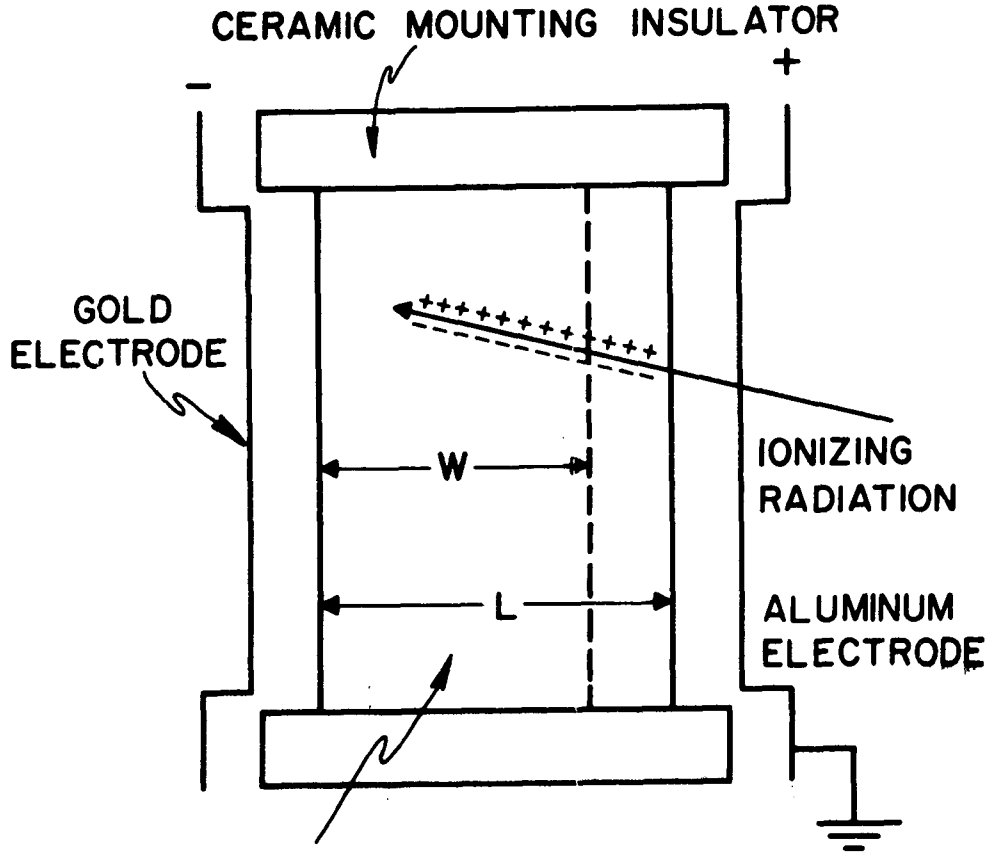

L = TOTAL THICKNESS

W = DEPLETION ZONE

TOTALLY DEPLETED: W = L

* FROM ORTEC INSTRUCTION MANUAL SURFACE BARRIER DETECTORS.

Figure (11)

occurs whether a current is flowing or not. This "white noise" arises because electrical charges in a conductor are in a state of constant thermal agitation, which manifests itself by voltage fluctuations between the terminals of the conductor (Johnson, 1928). These voltage fluctuations have an average value of zero, but the r.m.s. (root mean square) value is nonzero and is given by the formula (Dearnaley and Northrop, (1966)):

$$\overline{V^2} = 4\ kT\ R\ \Delta f \qquad (1)$$

where V = voltage across the resistor
k = Boltzmann constant
T = absolute temperature
R = resistor value
Δf = bandwidth

The preamplifier noise is mainly due to thermal noise in the conducting channel of the first stage field effect transistor (FET). Using equation (1) and the relation Q = CV, the equivalent noise charge is:

$$\overline{Q^2} = 4\ kT\ R_n \frac{C^2}{\tau} \qquad (2)$$

where
Q = r.m.s. noise charge
τ = $1/\Delta f$ = RC = preamplifier time constant
R_n = main series resistor value
= $\approx .7/g_m$ for the FET; g_m = transconductance
C = total capacitance parallel to the main series resistor
= detector capacitance + FET input capacitance + stray wiring capacitance.

The resistance parallel to the detectors such as the bias and feedback resistors also produces thermal noise. This thermal noise is a small part (<5%) of the total thermal noise including preamplifier thermal noise. From equation (1) and using the relation that $\tau = 1/\Delta f = RC$ gives the equation:

$$\overline{V^2} = 4 \frac{kT}{C} \qquad (3)$$

Using Q = CV, the r.m.s. noise charge is given by the formula:

$$\overline{Q^2} = 4\ kTC = 4\ kT \frac{\tau}{R} \qquad (4)$$

where τ = RC = preamplifier time constant.

In Figure 12 (Noise vs. Capacitance), various capacitances were substituted in place of surface barrier detectors in the engineering model of the electron-proton spectrometer. The total thermal noise in

terms of FWHM (full width at half maximum) broadening of a monoenergetic pulser peak was measured. The graph shows the increasing thermal noise with increasing equivalent detector capacitance.

The second important source of electronic noise is current noise due to the leakage current of the detector when voltage is applied to the detector. The detector leakage current consists of several components including currents determined by recombination centers in the detector sensitive volume and surface currents. The theoretical treatment of surface currents is not adequately understood and, thus, not discussed by Dearnaley and Northrop (1966) or Bertolini and Coche (1968) or in this paper. However, Dearnaley and Northrop (1966) state, and it may be concluded in this experiment, that surface currents appear to be the principal source of current noise.

The random fluctuations of the detector leakage current generate shot noise. The mean square value of the current fluctuation is given by Bertolini and Coche (1968):

$$\overline{i_n^2} = 2\, e\, I_L\, \Delta f \tag{5}$$

where

e = electron charge
I_L = mean leakage current
Δf = frequency bandwidth of the preamplifier circuit.

In terms of mean square noise charge, this current noise becomes by integration of equation (5):

$$\overline{Q^2} = 2\, e\, I_L\, \tau \tag{6}$$

where $\tau = RC$ = preamplifier time constant. Note that this current noise varies directly with the preamplifier time constant τ whereas the main part of the thermal noise (due to the preamplifier) varies inversely with τ.

Note that these values of noise in terms of the r.m.s. noise charge Q can be converted to noise in terms of r.m.s. energy W, with the relation:

$$W = \omega \frac{Q}{e} \tag{7}$$

where

ω = mean energy lost per electron-hole pair produced
= 3.6 eV for silicon.

In addition to the electronic noise, there are other effects which contribute to the broadening of the energy resolution. The statistical fluctuation in the energy lost by an incident particle in

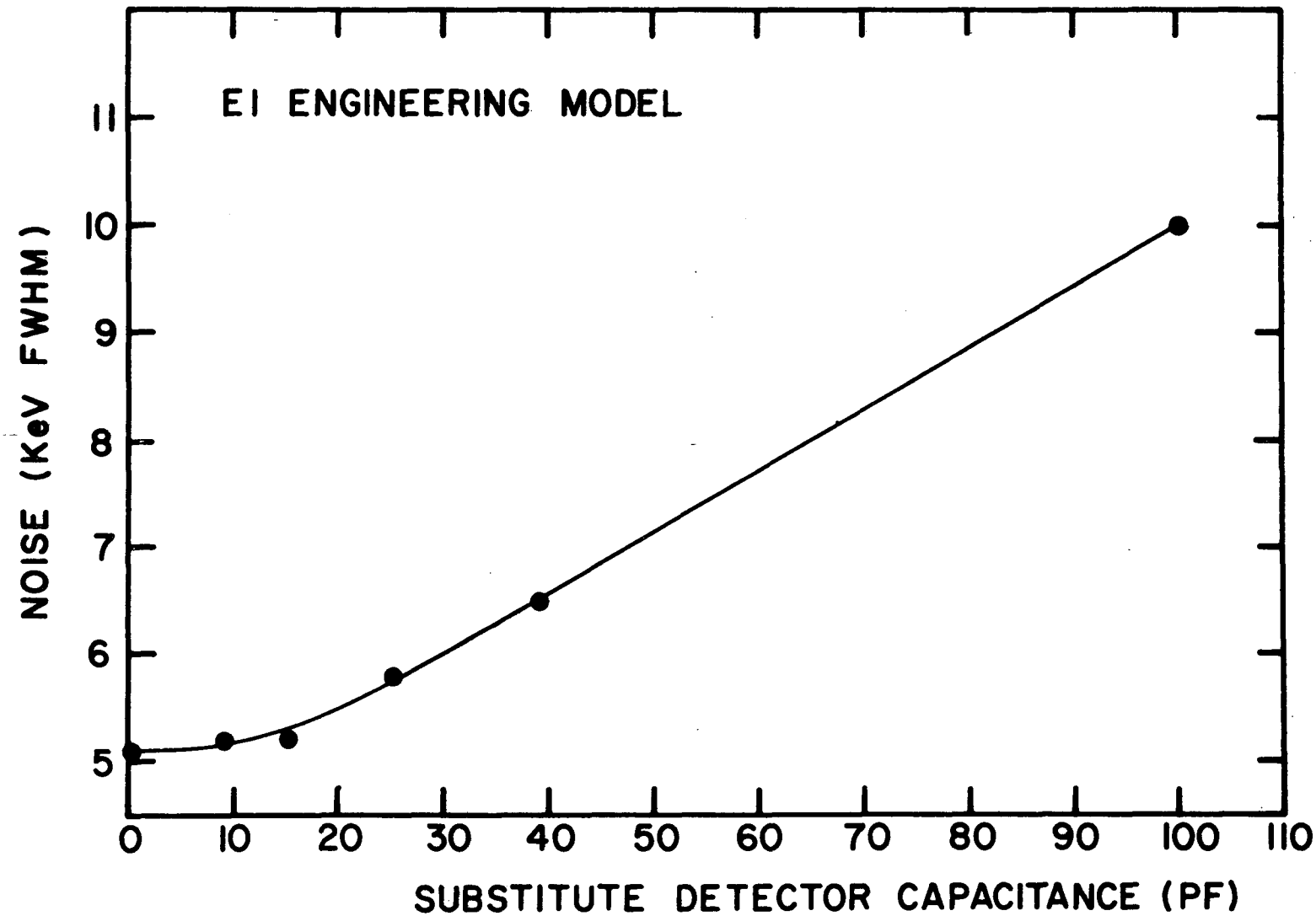
E1 ENGINEERING MODEL
NOISE (KeV FWHM)
11
10
9
8
7
6
5
0
10
20
30
40
50
60
70
80
90
100
110
SUBSTITUTE DETECTOR CAPACITANCE (PF)

Figure (12)

creating electron-hole pairs in the silicon has a broadening effect on the energy resolution. Also, imperfect charge collection and variations in energy lost in the dead layer of a detector has the same effect. For electrons and protons, these additional effects are quite small compared to the electronic noise broadening.

C. Temperature Effects

Cooling the gold-silicon surface barrier detectors below room temperature (+25°C) has a large effect on the detector leakage current and, thus, on the detector current noise following from equation (6). The current density J_s from carriers generated by recombination centers in the detector sensitive volume is given by Dearnaley and Northrop (1966) as:

$$J_s = \frac{en_i}{2\tau_r} \quad x \tag{8}$$

where

e = electron charge
x = depletion layer thickness
n_i = number of electrons in the conduction band
τ_r = recombination time

The temperature dependence of n_i is given by:

$$n_i \propto \exp(-E_g/2kT) \tag{9}$$

where E_g is the energy gap of the semiconductor (for silicon E_g = 1.09 eV). τ_r is also somewhat temperature dependent, but the net result is dominated by the temperature dependence of n_i which gives a very rapid decrease in current and current noise with a decrease in temperature.

The temperature dependence of the surface currents is not well understood. However, experimental evidence shows that the total detector leakage current is greatly temperature dependent. The reverse currents in the prototype and flight model detectors are reduced from typical values of 0.2 - 0.4 microamps at +25°C to <0.01 microamps upon cooling to -10°C.

Cooling the conductors causing thermal noise has a very small effect on the thermal noise as thermal noise is proportional to the square root of the absolute temperature of the conductors. Thus, cooling from 25°C to 0°C only reduces the thermal noise by ≈4%.

Since the thermal noise of the preamplifier and the current noise of the detector are two independent sources of noise, they add in quadrature. Thus, the total electronic noise N_T from these two sources is given by:

$$N_T = (N_{TH}^2 + N_D^2)^{1/2} \qquad (10)$$

where N_{TH} is the thermal noise and N_D is the detector noise.

Figure 13 shows the experimentally determined total noise versus temperature for the flight model detectors to be used for the lowest energy electrons and protons. (The temperature was measured with thermistors located in the preamplifier box, for which calibration curves are given in Figure 32 in Section X.) Also given in Figure 13 are theoretical curves for total noise versus temperature calculated from equations (2), (6) and (10) using the approximate values characteristic of the electron-proton spectrometer electronic circuits of τ = 0.5 μsec., C = 35 pF, and R_n = 350Ω. The leakage current temperature dependence was calculated from equations (8) and (9) beginning with typical values of 0.20 μa and 0.30 μa at 25°C. Figure 13 also gives typical leakage currents for these particular four detectors at 25°C, however, the exact leakage currents corresponding to the noise levels in Figure 13 are not known. Note that the theoretical curves do not accurately describe the relation between leakage current and noise in absolute comparisons between different detectors, possibly because of individual differences in manufacturing. However, the leakage current for each particular detector does generally follow the theoretical temperature dependence. Thus, the total noise for each channel generally approaches the thermal noise value of that channel asymptotically as the temperature is reduced.

D. Light Effects

Light of quantum energy greater than the energy gap of a semiconductor is readily absorbed and generated electron-hole pairs. With the gold-silicon surface barrier detector, the detector has been found to be much more sensitive to light through the gold layer than the aluminum layer. For this reason and the fact that the gold-silicon junction is more susceptible to radiation damage, the aluminum side of the detectors faces the entrance opening in the electron-proton spectrometer. The detectors are completely enclosed by the light tight iron core with the only opening being the entrance aperture. However, only the proton detector is in direct line with the entrance aperture which would look at the sun only infrequently. Thus, the effects of light on the surface barrier detectors in the electron-proton spectrometer are reduced to minimal importance.

E. Detector Selection

In choosing specific surface barrier detectors, particular attention must be paid to the choice of detector sensitive area and sensitive depth. The detector sensitive area is related to detector noise and to the diode capacitance, which in turn determines the

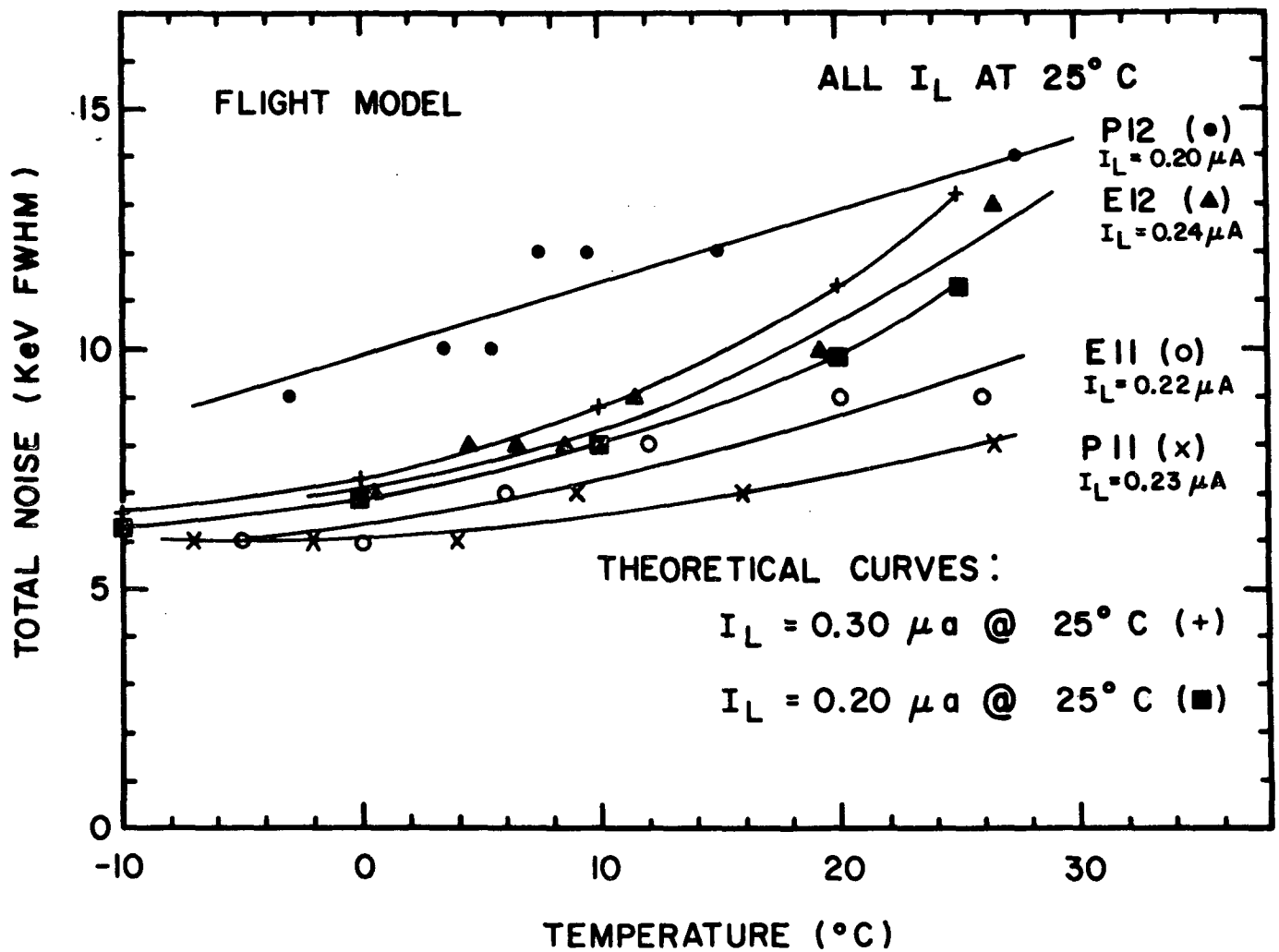
FLIGHT MODEL
ALL I_L AT 25° C
P12 (•)
I_L = 0.20 μA
E12 (▲)
I_L = 0.24 μA
E11 (o)
I_L = 0.22 μA
P11 (x)
I_L = 0.23 μA
THEORETICAL CURVES:
I_L = 0.30 μa @ 25° C (+)
I_L = 0.20 μa @ 25° C (■)
TOTAL NOISE (KeV FWHM)
TEMPERATURE (°C)
0
5
10
15
-10
0
10
20
30

Figure (13)

thermal noise at the preamplifier input as shown by equation (2). A larger sensitive area corresponds to a greater diode capacitance which gives a larger thermal noise.

The detector sensitive depth is inversely proportional to the diode capacitance. Therefore, a greater sensitive depth would give a lower thermal noise. However, the detector noise increases as the sensitive volume increases because of the increase in the number of charge carriers. Thus, there is usually some optimum sensitive depth which gives the lowest total noise for the system. Another consideration in selecting the detector sensitive depth is that the particle to be detected must lose all of its energy in the sensitive volume if the output pulse height is to be proportional to the particle energy. In such applications where linearity of pulse height with particle energy is required, the maximum range of the particles to be analyzed determines the minimum sensitive depth.

The flight-model detectors were specially selected for their low room-temperature detector noise. Table III lists the noise values and other specifications of the Ortec silicon surface barrier detectors used in the electron-proton spectrometer. It is especially important to select low noise detectors so that the noise edge is well below the electronic discriminator edge for the expected detector operational temperature range of $-30^{\circ}C$ to $+5^{\circ}C$. Otherwise, the noise pulses would trigger the lower edge and be counted as real particles.

Also, too high a noise level even below the discriminator edge can have spurious effects on the results. Noise broadens monoenergetic pulses by randomly adding and subtracting a distribution of voltages from the mean voltage of the monoenergetic pulse. Thus, for example, at the 20 keV lower edge of the low energy proton channel, the noise would distribute monoenergetic 20 keV pulses such that only one half of the 20 keV pulses would arrive at the discriminator with voltages high enough to trigger the 20 keV edge. Thus with a spectrum of energies, some protons depositing less than 20 keV in the detector may have noise added to their pulses and a resulting voltage high enough to trigger the 20 keV discriminator and vice versa, some protons depositing greater than 20 keV in the detector, which should be counted, will have noise subtracted from their pulses and not trigger the discriminator. The noise would have no effect on the count rate observed if there were equal numbers of pulses at all energies. However, at synchronous orbit, the number of electrons and protons increases as the electron and proton energy decreases, forming a power law spectrum as shown in Figure 15 in Section VI. Thus, at the 20 keV proton edge, more counts will be added to the window than subtracted and, at the upper edge of 50 keV, more counts will be subtracted from the window than added by the noise. The combined result at the two edges would be to add some counts to the 20-50 keV window because of the greater number of energy loss pulses around 20 keV than around 50 keV. As the noise level is reduced, this effect is also reduced. A temperature coefficient of count rate can be produced if there are many protons just below the lower edge.

TABLE III

ORTEC GOLD-SILICON SURFACE BARRIER DETECTOR CHARACTERISTICS

	Serial Number	Energy Channel	Sensitive Area (mm^2)	Sensitive Depth (μ)	Detector Capacitance (pF)	Detector Bias (volts)	Noise Width* (keV FWHM)
PROTOTYPE	9-111C	E11	25	300	9	-100	6.7
	9-28B	E21	25	300	9	-100	10.0
	9-621A	E31	50	300	18	-100	9.9
	9-432C	P1	25	200	13	-75	6.5
	9-112C	E12	25	300	9	-100	9.1
	9-209C	E22	25	300	9	-100	8.6
	9-268B	E32	50	300	18	-100	10.1
	9-438C	P2	25	200	13	-75	10.5
FLIGHT	9-208C	E11	25	300	9	-100	6.2
	9-113C	E21	25	300	9	-100	6.4
	11-270F	E31	50	300	18	-100	8.6
	9-436C	P1	25	200	13	-75	5.9
	9-114C	E12	25	300	9	-100	6.3
	9-214C	E22	25	300	9	-100	6.5
	11-270D	E32	50	300	18	-100	8.7
	11-157F	P2	25	200	13	-75	7.4
SPARES	9-118C	E1/E2	25	300	9	-100	6.8
	9-207C	E1/E2	25	300	9	-100	7.4
	11-123A	E3	50	300	18	-100	12.1
	11-123E	E3	50	300	18	-100	13.2
	11-157H	P	25	200	13	-75	9
	11-157E	P	25	200	13	-75	9.6
	11-157G	P	25	200	13	-75	10.0

*As measured by Ortec at room temperature with detector connected as a noise source to input of Ortec amplifier system.

VI. MAGNET-DETECTOR ARRAY SYSTEM DESIGN

A. Description

The primary considerations in the design of the permanent magnet and detector array system were to direct the three desired energy intervals of electrons into three different surface barrier particle detectors and to direct the protons of all energies into a fourth surface barrier detector. One important condition was that low energy electrons (<100 keV) should not be allowed to enter the proton detector and be counted spuriously as low energy protons. The permanent magnet circuit consists of two bi-lavered pole pieces, have an Alnico 5 permanent magnet layer with an Armco ingot iron layer as a pole face. These components of the permanent magnet circuit are shown in Figures 6 and 14. The desired magnetic induction in the air gap is ≈700 gauss and the air gap is 0.200" across. The detection geometry, the physical positioning of the detectors around the permanent magnet pole face, the permanent magnet design, and electronic considerations were all important variables in determining the desired result.

B. Geometry

The detection geometry was selected knowing the probable maximum differential energy spectra of electrons (Lezniak, (1970)) and protons (Frank, (1967)) at synchronous orbit and knowing the maximum count rate capacity of the accumulators on the spacecraft. Figure 15 shows the typical differential energy spectra expected at synchronous orbit for a substorm maximum. The spacecraft accumulators have a maximum capacity of 2^{16} or 65,536 counts. The collimator was designed so that there would be an ample margin between the expected count rates and the spacecraft's capabilities. The geometry is calculated from the dimensions of the tubular collimator according to the following equation:

$$\text{Geometry Factor} = \frac{A^2}{l^2} \qquad (11)$$

where A is the cross-sectional area of the tubular opening and l is the length of the tubular opening in the collimator and $l^2 >> d^2$ where d is the diameter of the tubular opening. For a l = 1 inch and d=0.081 inches, the geometry factor of the collimator is 1.69×10^{-4} ster-cm^2. The inside of the collimator is screw-threaded to reduce the electron scattering off the inside surface of the collimator.

C. Detector Array Design

The physical positioning of the detectors around the permanent magnet and the choice of the magnetic field strength in the air gap were initially determined by trial and error methods. Geometric ray tracing was first used with various combinations of the above variables

EXPLODED VIEW LOOKING
INTO COLLIMATOR OPENING

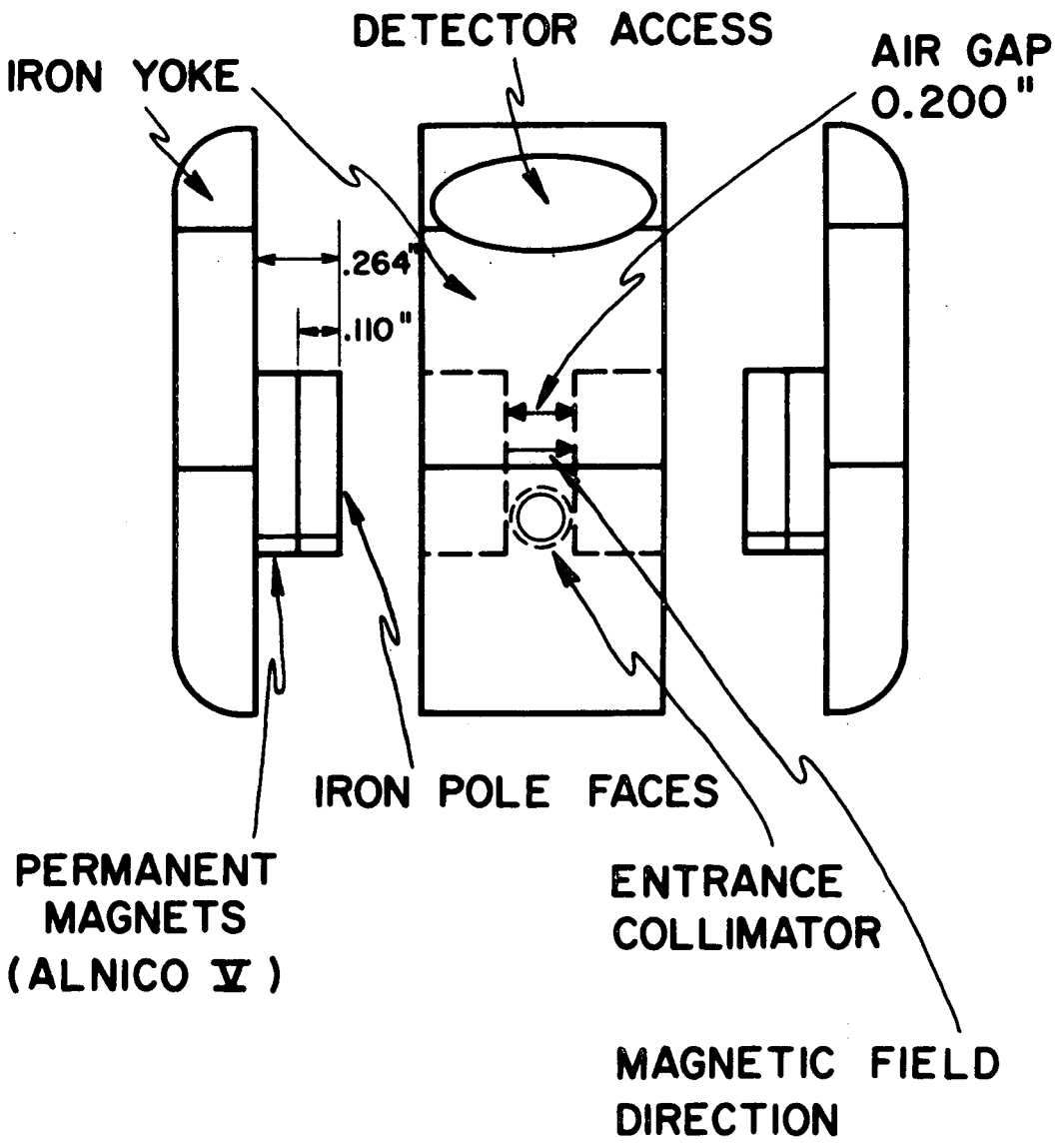

Figure (14)

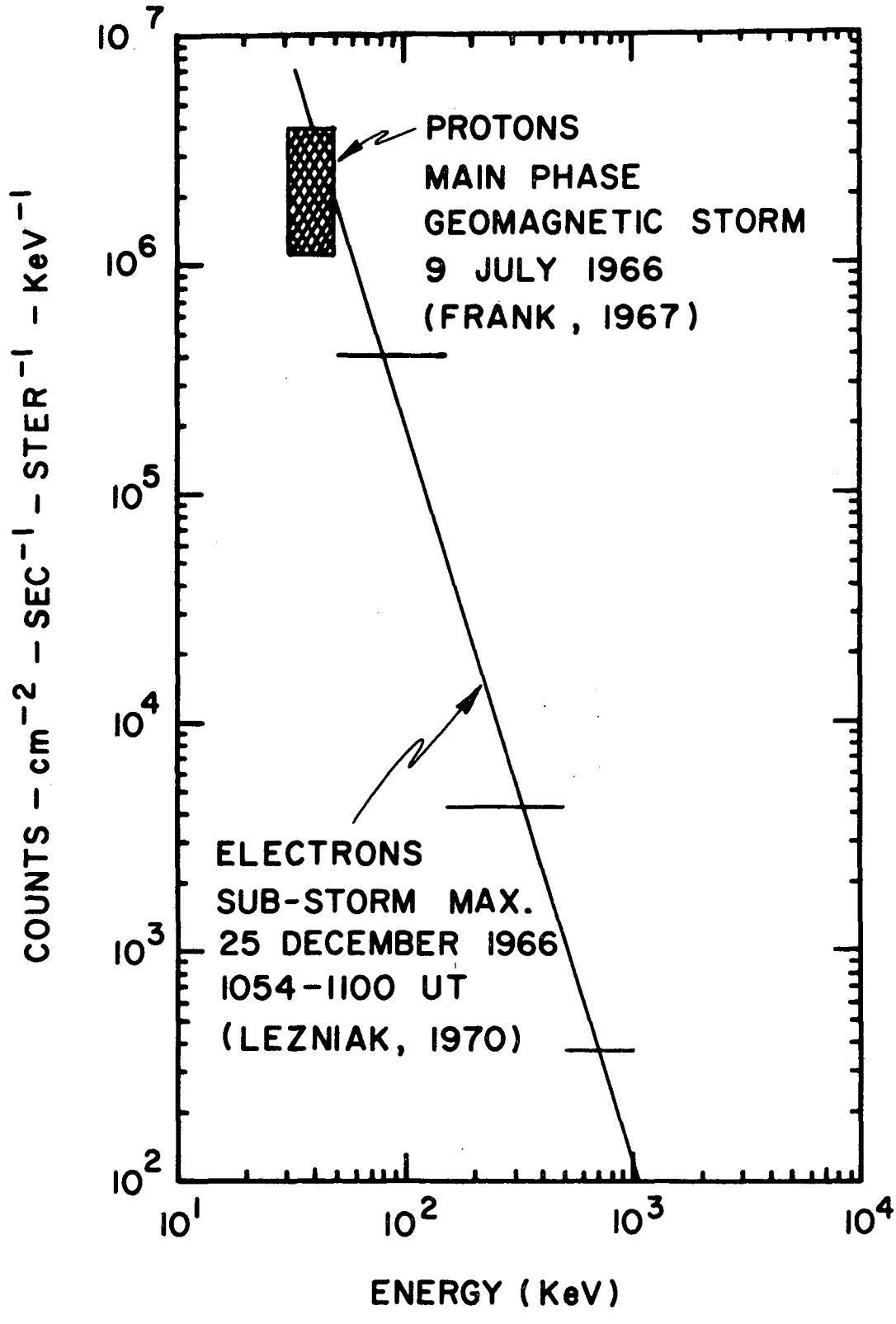
PROTONS
MAIN PHASE
GEOMAGNETIC STORM
9 JULY 1966
(FRANK , 1967)
ELECTRONS
SUB-STORM MAX.
25 DECEMBER 1966
1054-1100 UT
(LEZNIAK, 1970)
COUNTS - cm⁻² - SEC⁻¹ - STER⁻¹ - KeV⁻¹
ENERGY (KeV)
10⁷
10⁶
10⁵
10⁴
10³
10²
10¹
10²
10³
10⁴

Figure (15)

to trace the paths of electrons and protons in a uniform magnetic field in the air gap. The final positioning was determined in conjunction with the selection of the final design of the permanent magnet using a computer program written by Dr. Karl A. Pfitzer for calculating trajectories of electrons through the air gap. The final detector stacking arrangement is shown in Figure 16.

D. Permanent Magnet Design and Circuit

The permanent magnet was not designed to be a sharply focusing magnet. Rather it was designed to roughly sweep the lower energy electrons away from the proton detector in such a manner that a significant fraction of the electrons entering through the collimator would be directed into the appropriately placed electron detectors. The magnet pole faces were designed to be vertically focusing however, That is, electrons entering the collimator opening at the maximum acceptance angle on a trajectory tilted towards the inner surface of the magnetic pole faces will experience a force away from the pole face. This is accomplished by slanting the front edge of the pole pieces so that the electrons enter the air gap at an acute angle with the front side of the pole pieces (Gross, (1951)). (See Figure 6). The fringing fields at the slanting edge of the pole piece are such to give the incident electron a push back towards the center of the air gap. This prevents electrons from scattering off the pole face and entering the wrong detectors. The computer program written by Dr. Karl A. Pfitzer for tracing electron trajectories accounted for these fringing field effects.

The amount of permanent magnetic material and the degree of its magnetization, the thickness of the air gap, and the minimum thickness of the soft iron yoke needed to obtain the desired magnetic induction in the air gap were approximately determined by using magnetic circuit theory. The magnetomotive force of the permanent magnet, the reluctance of the yoke and air gap, and the magnetic flux in the circuit have relationships comparable to the Ohm's law relationship between voltage, resistance and current, respectively. The exact amount of permanent magnetic material necessary for the selected air gap and yoke configuration was finally determined experimentally, and is shown in Figures 6 and 14. The Alnico V permanent magnets are 0.154" thick and the Armco iron pole faces are 0.110" thick.

The bi-layered pole piece construction was used because it simplified the selection and reproducibility of the magnetic field in the air gap. Since two identical magnet-detector systems are needed for each model of the electron-proton spectrometer, a method of magnetization was desired which would give reproducible fields of the same desired magnitude. The resulting, most satisfactory method of magnetization involved choosing the proper amount of permanent magnetic material (Alnico 5) for the given air gap and yoke configuration such that the proper field occurs in the air gap when the

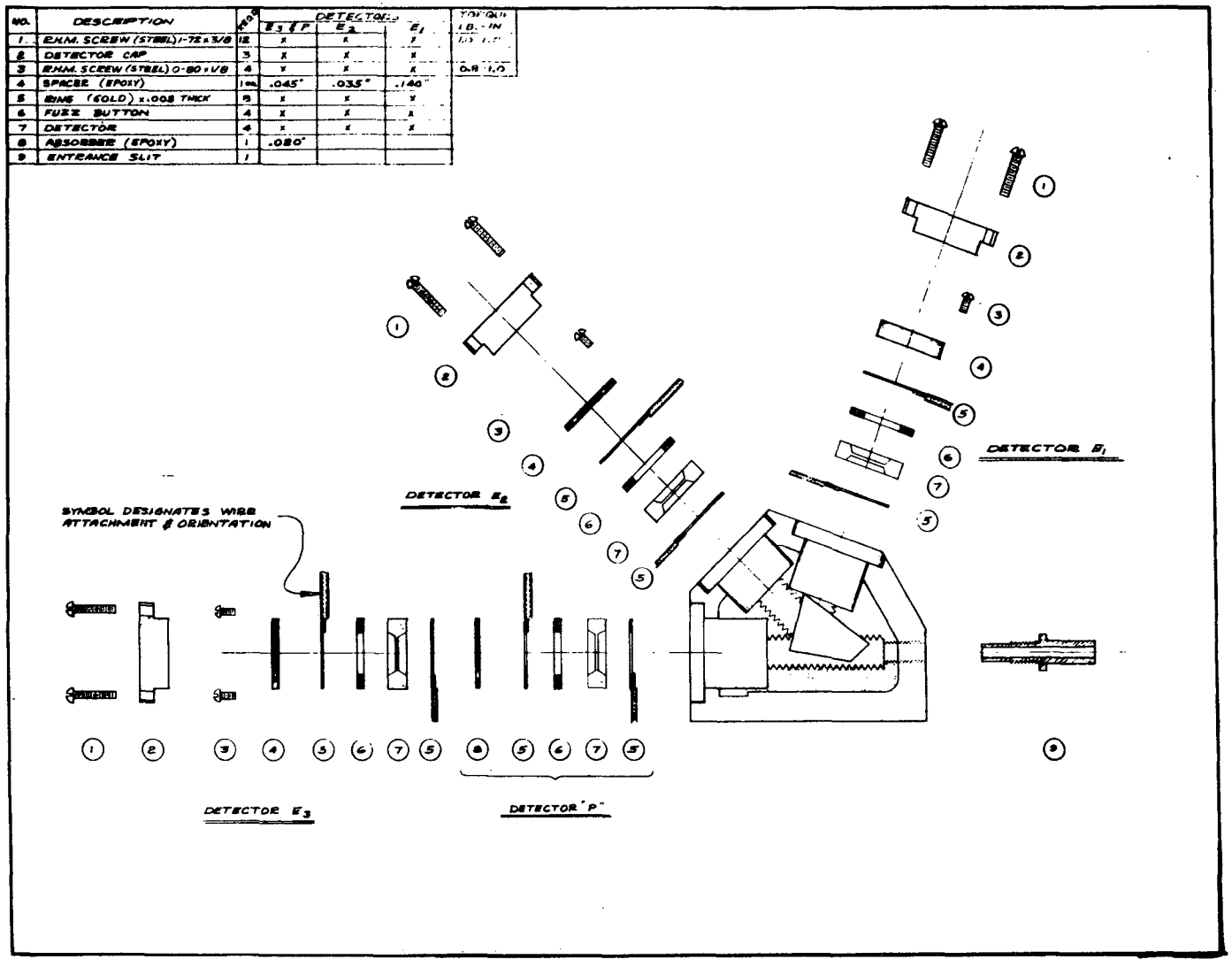
NO. DESCRIPTION REQ'D DETECTOR TORQUE LB. - IN
1. FLAT. SCREW (STEEL) 1-72 x 3/8 12 X X X
2. DETECTOR CAP 3 X X X
3. FLAT. SCREW (STEEL) 0-80 x 1/8 4 X X X 0.8 1.0
4. SPACER (EPOXY) 1 .045" .035" .140"
5. RING (GOLD) x.008 THICK 5 X X X
6. FUZZ BUTTON 4 X X X
7. DETECTOR 4 X X X
8. ABSORBER (EPOXY) 1 .020"
9. ENTRANCE SLIT 1
SYMBOL DESIGNATES WIRE ATTACHMENT & ORIENTATION
DETECTOR E2
DETECTOR E1
DETECTOR E3
DETECTOR "P"

Figure (16)

permanent magnet is saturated. Using the permanent magnets saturated means that no special magnetization apparatus is necessary. The magnet is easily saturated by any electromagnet with greater than ≈2 kilogauss since the desired field in the air gap is approximately 700 gauss.

E. Permanent Magnet Material

Alnico 5, an alloy of mainly aluminum, nickel, and iron, was chosen for the permanent magnet material because it is very stable under the influence of two main demagnetizing forces: vibration or shock, and heat. In vibration testing the engineering and prototype models of the electron-proton spectrometer, the stability of the Alnico 5 permanent magnet was indirectly tested. Count rates in all energy channels were measured before and after each vibration with no change observed. This implies that the magnetic induction of the permanent magnets did not change within a few percent. In addition, the stability of the flight model permanent magnets under flight model vibration specifications was directly tested. The maximum magnetic induction at the center of the permanent magnet pole pieces in the air gap was measured before and after vibration with a Radio Frequencies Laboratory (R.F.L.) model 1890 Gaussmeter. No change in the magnetic induction was observed to within the 3% accuracy of the test instrument.

The manufacturer's data (Thomas and Skinner, Inc.) also shows that Alnico 5 permanent magnets lose only about 0.025% of their original flux after heating to +60°C and cooling back to room temperature. Also, cooling the Alnico 5 material below room temperature has no effect on the magnetic induction. Since +60°C is the extreme high temperature that the electron-proton spectrometer might experience in storage and since the normal operational temperatures are below +5°C, the Alnico 5 permanent magnet will be extremely stable under these temperature conditions.

F. Magnetization

The magnetis for all models of the electron-proton spectrometer were magnetized by the electromagnet in the lecture-demonstration room of the Tate Laboratory of Physics, University of Minnesota, using magnetizing fields of 4-5 kilogauss. Since the heating in the soft soldering process involved in the fabrication of the bi-layered pole pieces destroys the polarization of the magnetic field in the permanent magnet, the magnets must be magnetized after the soldering is completed. The permanent magnets are magnetized by removing the iron cover plates with the pole pieces on them from the center portion of the epoxy potted detector array. The iron pole faces of the permanent magnets are placed directly together and clamped tightly between the pole faces of the electromagnet. The current need only be turned on the electromagnet for about one second and the permanent magnets will be saturated. Each set of permanent magnets, iron yoke side plates, and epoxy potted

iron yoke center section is identified by a number etched on the inside adjoining surfaces of the iron cover plates and center yoke section. The magnetic induction is measured by placing the R.F.L. gaussmeter model 1890 Hall-effect probe through the E2 detector access port hole (before the detectors are installed) into the air gap between the pole pieces in such a manner that the flat surface of the probe is parallel to and halfway in between the pole faces and is in the center of the pole faces. Table IV gives the residual magnetization in the center of the air gap of the assembled permanent magnet-iron yoke system as measured by the procedure above.

Special care must be taken to make sure that the direction of the magnetic field between the pole pieces is correct. Looking through the collimator from the outside of the iron yoke into the air gap, the field direction should be from left to right as in Figure 14. This direction can be easily tested with a magnetic compass. The north seeking needle on a magnetic compass will point in the direction of the magnetic field. Thus, after magnetizing the pole pieces on the iron cover plates, the direction of the magnetic field must be tested. The field between the permanent magnet pole pieces should be checked by observing that the north seeking needle points to geomagnetic north.

G. Magnetic Shielding

The permanent magnet is enclosed by an Armco ingot iron (high permeability: 10^5) cup-core type yoke. This acts as a magnetic shield, drastically reducing the magnetic field of the permanent magnet outside of the iron yoke. This shielding is important on the spacecraft since there is a magnetometer experiment onboard which measurs the ambient magnetic field at synchronous orbit. The external leakage magnetic field of this magnet system was tested with a differential Magnetic Impurities Meter made by Schonstedt Instrument Company. The instrument consists of a detector core and a reference core spaced 5" apart and a meter which reads the difference in the external magnetic field at these two points. The magnetic impurities detector is placed in the center of large Helmholtz coils which help to neutralize the earth's magnetic field. The magnetic impurities meter can then be finely adjusted to totally neutralize the earth's magnetic field. Magnetic fields can be measured accurately on the order of 1 gamma. The engineering model magnet-detector array system was tested after it had been externally "de-gaussed" (placed in an alternating magnetic field and withdrawn slowly) and with a field of 1100 gauss in the air gap (greater field in the air gap than the ≈700 gauss fields now present in all the models of the electron-proton spectrometer). (The "de-gaussing" process does not change the field in the air gap.) The result, using the fact that the dipolar magnetic field drops off as the inverse cube of the distance, was that the maximum leakage field from the magnet-detector array system was 6 gammas at one foot, which easily satisfies the prescribed specifications.

TABLE IV

PERMANENT MAGNET CHARACTERISTICS

Model	Detector System	Magnet Identification Number	Magnetic Induction at Center of Air Gap (Gauss)
Prototype	Fixed	1	680 ± 20
Prototype	Scanning	3	675 ± 20
Flight	Fixed	4	720 ± 20
Flight	Scanning	5	720 ± 20

H. Radiation Shielding

The iron yoke also serves as radiation shielding. The surface barrier detectors have a minimum of 5 g-cm^{-2} of shielding in all directions except for the small collimator opening. This shielding will prevent electrons with energies less than ≈8.2 MeV and protons with energies less than ≈63 MeV from impinging upon the surface barrier detectors (Subcommittee on Penetration of Charged Particles, (1964)). Thus, essentially 100% of the electrons and protons at synchronous orbit will be shielded from the surface barrier detectors except for those entering the small collimator opening as desired. There will be some background counts due to penetrating γ-rays and X-rays which will be determined by the scanning detector when it looks at the 5 g-cm^{-2} brass plug at one of its scanning positions. This background determination can be used to correct the observed rates of both the scanning and fixed detector systems, since they are essentially identical.

I. Electrical

The iron core center section is potted with Armstrong C7 epoxy with a teflon plug in the shape of the pole pieces positioned in place of the pole pieces and air gap. Holes are then drilled through the iron yoke and epoxy potting for placement of the surface barrier detectors in the desired position around the pole pieces. The epoxy acts as an electrical insulator around the detectors. The electrical contacts to the detectors are made with thin gold washers onto which the lead wires are soldered. A compressible wire mesh washer or "fuzz button" is included to give some resiliency to the detector stacking arrangement. An epoxy-fiberglass disk is used to insulate the electrical signal contacts from the iron detector access cover. The stacking arrangement and electrical connections for the detector array are shown in Figure 16.

VII. MAGNET-DETECTOR ARRAY SYSTEM ENERGY RESPONSE CHARACTERISTICS

A. E1 Channel Response to Electrons*

The response of the magnet-detector array system to electrons was tested with a 0-125 kV electron accelerator and with Pm-147 and Sr-90 radioactive beta sources. The response of the low energy electron detector E1 was tested primarily with the 0-125 kV electron accelerator. Testing with low energy electrons (<125 keV) from the electron accelerator is always done with the detector array in a cold-trapped diffusion

*Since the scanning and fixed detector systems are essentially identical, for simplicity the E11 and E12 channels will be referred to as the E1 channel, the E21 and E22 channels as E2 channel, the E31 and E32 channels as E3 channel, and similarly for the P channels.

pump vacuum with pressures less than 1 x 10^{-5} Torr. Testing with both the engineering model and flight model magnet-detector arrays shows that the lowest energy electron directed by the permanent magnet into the E1 detector is 32 + 2 keV. Figure 17 shows the pulse height analysis of the energies lost in the E1 engineering model detector from various energy beams of electrons from the electron accelerator. The numbers of counts at each energy is not exactly comparable due to slight variations in the current in the electron emitting filament. Thus, the counts are not indicative of the counting efficiency of the magnet-detector system at the various energies. However, the figure does show the sudden energy degradation for electrons with energies of 31 and 32 keV because they are not magnetically deflected directly into the detector.

A significant fraction of electrons between 32 and 85 keV are directed into the E1 detector and lose their full energy in the detector. Above 85 keV the electrons begin to hit the epoxy between the E1 and E2 detectors. Some of the electrons are scattered off the epoxy and lose a degraded amount of energy in E1 and E2. The electronic discriminator edges for E1 are set at approximately 25 and 50 keV on the flight model. Thus, combining the magnetic selection and electronic discrimination for E1, the E11 (scanning detector array) and E12 (fixed detector array) energy channels respond primarily to electrons with energies in the interval 30-50 keV. Some spurious counts will result from degraded energy losses from scattered electrons with energies greater than 85 keV. This spurious count rate should be less than a few percent of the total count rate in this channel at synchronous orbit, however, with the lower edge set at 25 keV, the danger of having the electronic noise count in the E11 and E12 channels (due to a higher than expected operational temperature or a gradual increase in detector noise because of detector deterioration) is greatly reduced.

B. Pile-Up Effects in E1 and E2 Channels

The sharp magnet cutoff at approximately 32 keV will prevent large fluxes of lower energy electrons (<25 keV) from entering the E1 detector and causing spurious counts from electronic pile-up. Pile-up is the effect at high count rates whereby two or more events (electrons losing their energy in the detector) occur in a time interval such that the detector and electronics cannot resolve the time difference between the events. Thus, the events appear to be simultaneous and the two or more events are counted as one. Thus, the detector and preamplifier would put out a pulse equal to the sum of the energies deposited in that small time interval rather than several smaller pulses corresponding to each individual particle energy. Thus, for example, if 15 keV electrons were magnetically directed into the E1 detector, when the flux of 15 keV electrons became high enough, some pulses equivalent to 30 keV and 45 keV would occur and be counted spuriously as electrons with these higher energies.

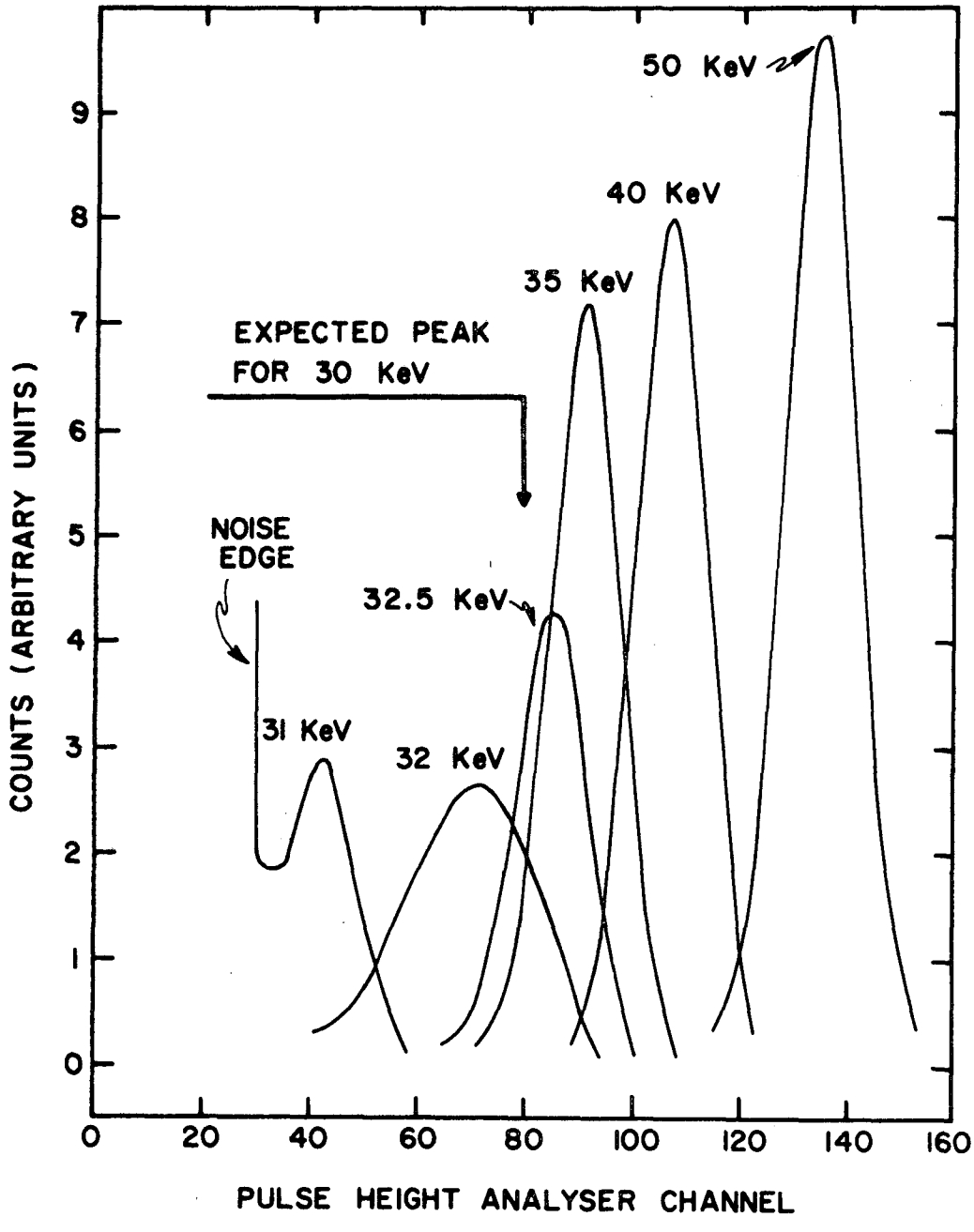
50 KeV
40 KeV
35 KeV
EXPECTED PEAK
FOR 30 KeV
NOISE
EDGE
32.5 KeV
31 KeV
32 KeV
COUNTS (ARBITRARY UNITS)
PULSE HEIGHT ANALYSER CHANNEL
0
1
2
3
4
5
6
7
8
9
0
20
40
60
80
100
120
140
160

Figure (17)

This pile-up effect is also the main reason for magnetically excluding electrons with energies less than approximately 85 keV from the E2 detector. Otherwise, these lower energy electrons would pile up forming pulses which would be spuriously counted in the 120-200 keV energy range.

C. E2 Channel Response to Electrons

The prototype fixed magnet-detector array was tested in fore-pump vacuum for the response of its E22 channel to electrons with energies between 100 and 190 keV. The OGO-I and -III type electromagnet designed by Pfitzer (1968) was used to select electrons in this energy range from the Sr-90, Pm-147 β-source 5125-3 manufactured by Isotope Products Laboratories. The source is pictured in Figure 21 and its spectrum is given in Figure 27. The E22 discriminator edges were set at 111 and 224 keV for this test. The main purpose of the test was to find the lowest energy electron that was directed into the E2 detector by the permanent magnet without scattering off the epoxy between the E1 and E2 detectors. The results of the test are shown in Figure 18. This shows that the lower magnetic cutoff for E22 on the prototype model is approximately 150 keV. This graph does not show the relative efficiency of response of E22 in this energy range. However, this test does show that E22 responds to electrons between 150 and 190 keV. The upper magnetic cutoff for the E2 detector has not been determined, but from this test and from comparison of the computer predicted electron paths and the actual experimental results for energies <100 keV, the upper magnetic cutoff is certainly greater than 200 keV and probably closer to 300 keV. Thus, with the E21 and E22 window discriminators set at 120 and 200 keV, these channels will respond mainly to electrons between 150 and 200 keV.

D. E3 and P Channels Response to Electrons

The high energy electron detector E3 is located behind the proton detector P with both detectors centered on the center line through the collimator aperture to form a two-fold coincidence circuit. In between the detectors is a fiberglass-epoxy board disk which serves as an absorber for the high energy electrons and as an electrical insulator between the electrical contacts to the P and E3 detectors. High energy electrons (>500 keV) entering through the collimator aperture are deflected by the magnet in varying amounts with the lower energies deflected the most. These electrons first pass through the P detector losing a portion of their original energy. These electrons then lose some additional energy in passing through the absorber between the P and E3 detectors. Finally, these electrons enter the E3 detector where some of lower energy in the range >500 keV will be stopped but those of higher energy will pass through the E3 detector experiencing a dE/dx energy loss.

The amount of energy lost in the P and E3 detectors by these electrons (>500 keV) can be roughly determined by range versus energy

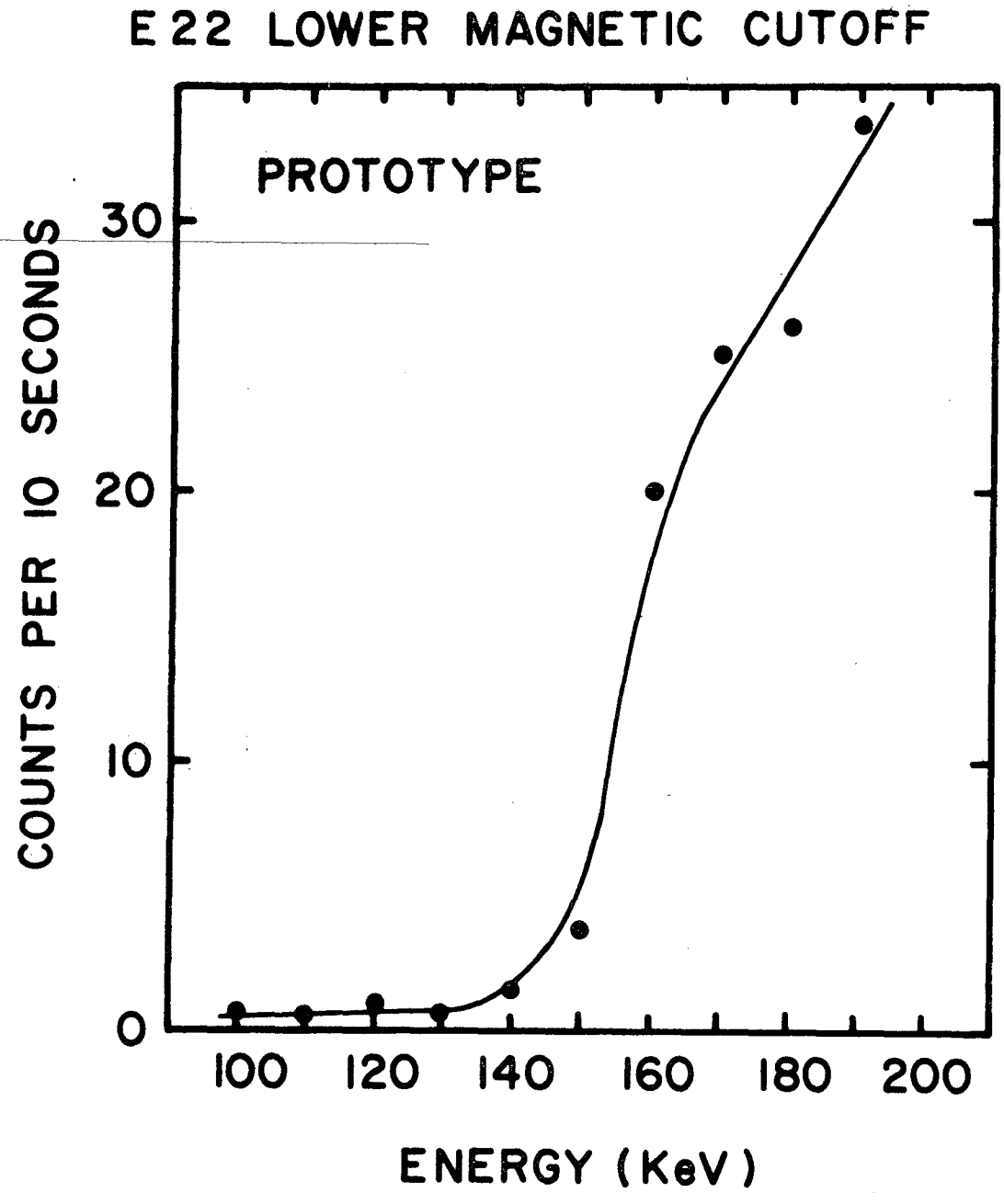
E 22 LOWER MAGNETIC CUTOFF
PROTOTYPE
COUNTS PER 10 SECONDS
0
10
20
30
100
120
140
160
180
200
ENERGY (KeV)

Figure (18)

and dE/dx versus energy graphs for electrons in silicon given in the Ortec Surface Barrier Detector Instruction Manual. The distance of penetration in matter for electrons of the same energy is not a precise distance because of straggling. Electrons are easily scattered when they interact with matter. Thus, their path through matter is not exactly a straight line, but a zig-zagging path on the atomic scale from one point of interaction to the next. The range of a particular energy electron in a given material is the mean straight-line distance penetrated into the material by electrons of that energy in losing all of their energy. Likewise, the dE/dx energy loss for the same energy electrons passing through a given thickness of material is not a precise amount, but subject to variations around a mean amount. Thus, in using the range versus energy and dE/dx versus energy curves, it must be kept in mind that these represent only the average values of the true behavior of a given energy electron.

The details of the selection of the thicknesses of the P detector, the E3 detector, and the absorber between them are given in Appendix II. The final selection of P and E3 detector and absorber depths includes a 200μ (Si) P detector, a 300μ (Si) E3 detector, and a 0.020" thick epoxy board absorber.

The details of the calculation and experimental testing of the electron energy loss in the E3 detector are also given in Appendix II. The nominal energy losses in E3 for the typical detector thicknesses are given in Figure 19. Figure 19 also shows the experimental energy loss peaks and variations around these peaks. Note that with the E3 discriminator set at 60 keV, the E3 channel responds to electrons >500 keV.

Appendix II also contains the details of the calculation and experimental testing of the electron energy loss in the P detector. The experimental results show that the majority of the $\overline{dE}/dx$ energy losses in the 200μ P detector from electrons >500 keV would fall between ≈45 and 120 keV, i.e. in the P2 energy window, as the discriminators are set at 50 and 150 keV.

The dead layer effects on electron energy loss are also discussed in Appendix II. For electrons, the energy lost in the dead layer of the detectors is negligible for all channels.

E. Coincidence Circuit for Highest Energy Electrons

An electronic coincidence circuit is arranged between the E31 and P21 channels and between the E32 and P22 channels. Pulses which trigger the E3 discriminator will only be counted if they are determined to be in coincidence with a pulse which falls in the P2 window. In the flight model, the E3 discriminator pulse lasts for approximately 4μ seconds and the P2 discriminator pulse lasts for 6μ seconds. These two discriminator pulses must overlap for at

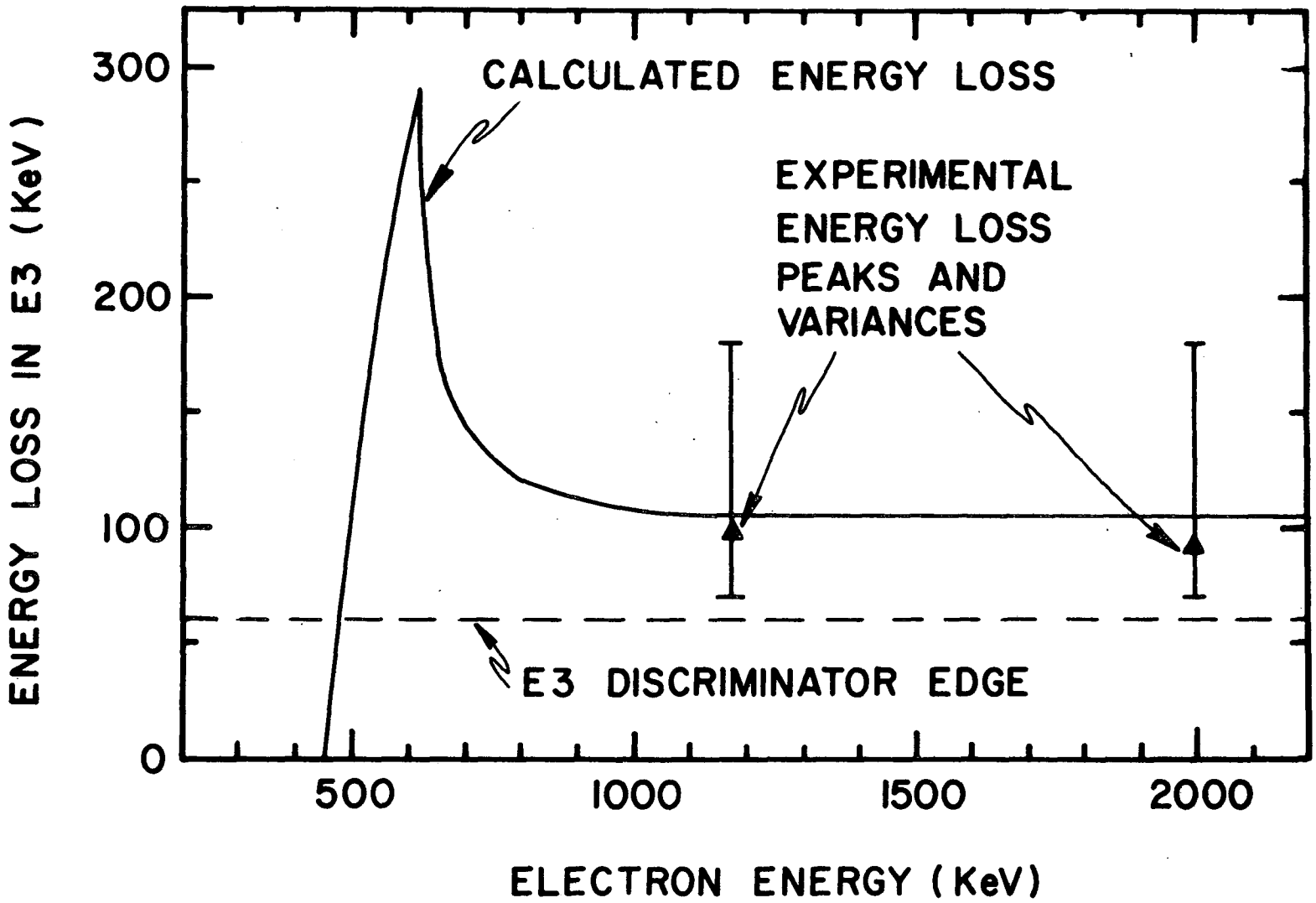
CALCULATED ENERGY LOSS
EXPERIMENTAL
ENERGY LOSS
PEAKS AND
VARIANCES
E3 DISCRIMINATOR EDGE
ENERGY LOSS IN E3 (KeV)
ELECTRON ENERGY (KeV)
300
200
100
0
500
1000
1500
2000

Figure (19)

least 2μ seconds in order for a "coincidence" to occur and for the E3 output pulse generator to be triggered. Thus, a discriminator pulse in E3 can begin during a time interval from 2μ seconds before the 4μ seconds after the beginning of a discriminator pulse in P2 and these pulses will be determined to be in "coincidence". Figure 20 shows this relationship between discriminator pulses in E3 and P2 of the flight model for a coincidence. Thus, the resolving time ($\Delta\tau$) of this coincidence circuit is 6μ seconds. This coincidence is necessary to insure that the low, true count rate in the E3 detector is not masked by the background radiation. The background count rate in E3 will usually be zero because of this coincidence circuit.

F. Spurious Background and Accidental Counts in E3

An occasional background count could occur if a background γ-ray happened to interact with some matter in front of or in the P detector such that an electron was formed which traversed both the P and E3 detectors, creating pulses of the proper magnitudes in both detectors. Spurious counts could also occur in E3 from accidental coincidences from pulses due to protons or background radiation in the P2 window and pulses due to the background radiation in E3. This accidental count rate R_{acc} in E3 is given by the following equation (Melissinos, (1968)):

$$R_{acc} = \Delta\tau\, R_1 R_2 \qquad (12)$$

where $\Delta\tau$ is the resolving time of the coincidence circuit, R_1 is the count rate due to protons and background radiation in P2, and R_2 is the total coincidenced and uncoincidenced count rate due to background radiation in E3. This equation is only valid for $R_{acc} < R_1$ or $R_{acc} < R_2$. When the scanning detector faces the background position, the observed coincidenced E3 count rate will approximately equal R_{acc}, $\Delta\tau$ is known, and R_1 will equal the background rate in P2, then the total coincidenced and uncoincidenced background rate in E3 will equal R_2 and can be calculated from the above equation. Then, when the scanning detector looks at the trapped radiation, the accidental rate R_{acc} in E3 can be calculated where R_2 has been calculated as above, $\Delta\tau$ is known, and R_1 is now the count rate in P2 from protons and background radiation.

G. Response of P Channels to Protons

Since a proton has a much smaller charge/momentum ratio than an electron of the same energy, a proton is bent much less in the magnetic field between the pole pieces than an electron of the same energy. Protons with energies 32-510 keV are hardly deflected by the ≈700 gauss magnetic field as they pass through the pole pieces. The proton detector is positioned such that all straight line trajectories through the collimator fall on its sensitive area. Thus, essentially 100% of the protons entering the collimator will lose their energy in the proton detector.

FLIGHT MODEL COINCIDENCE

DISCRIMINATOR OUTPUT PULSES

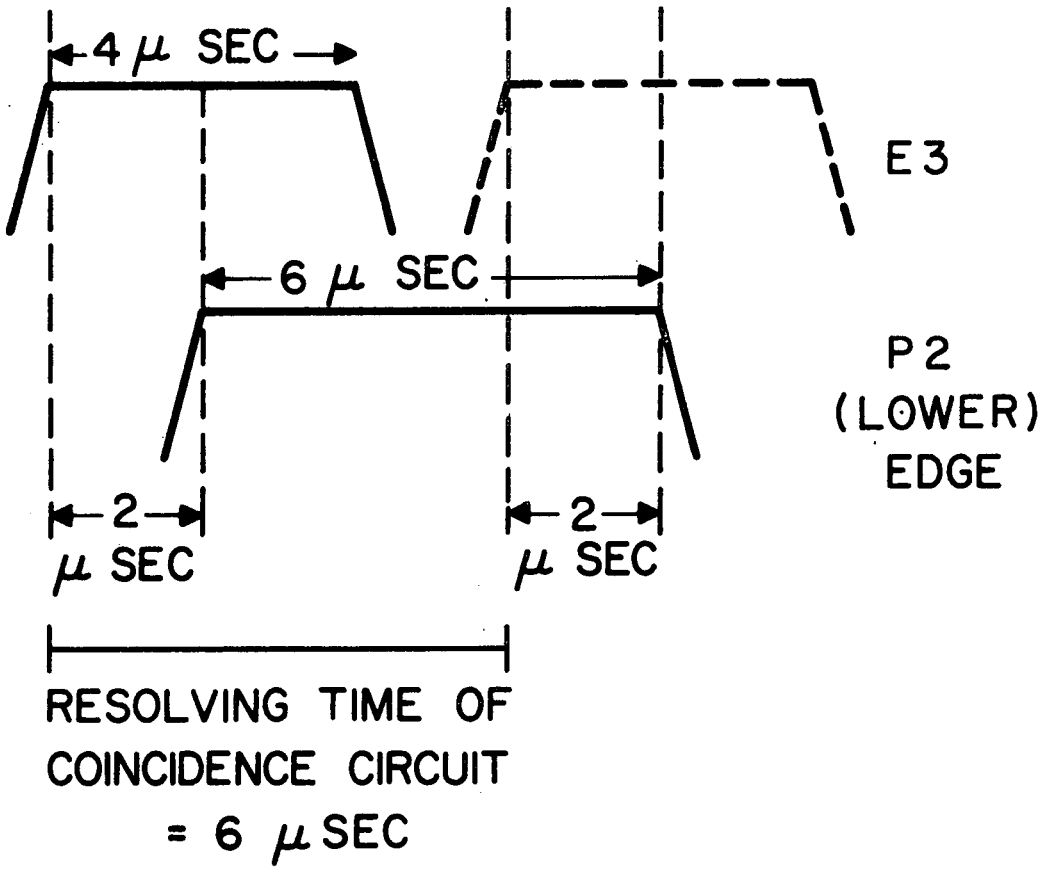

Figure (20)

The response of the surface barrier detector to protons is significantly affected by the dE/dx energy loss in the dead layer of 40μg-cm^{-2} of aluminum on the surface of the detector. Table V summarizes the energy lost in the dead layer for various proton energies. The values of dE/dx energy losses in aluminum are given by L. C. Northcliffe (Subcommittee on Penetration of Charged Particles, (1964)). Thus, with the edge discriminators set at 20, 50, 150 and 500 keV, the proton energy channels respond primarily to the following energies:

P11, P12	30-70 keV
P21, P22	70-170 keV
P31, P32	170-500 keV

The magnet-detector array response to protons was tested with a proton source capable of accelerating protons to energies of 0-125 keV. The proton source consists of an evacuated chamber, into which hydrogen (H_2) gas is leaked, containing an electron-emitting filament and an electron accelerator grid system. The hydrogen gas is ionized by the electrons eventually forming singly-charged hydrogen atoms or, in other words, protons. The protons are accelerated by applying a high positive voltage to the proton source. The repelled protons travel down an evacuated insulating tube and into the aperture of the magnet-detector array positioned at the end of the tube in an evacuated bell jar.

Tests with the proton source and the fixed magnet-detector array system of the flight model confirm the predicted dead layer effect described above. The electron-emitting filament current in the proton source was kept constant and, thus, the rate of proton production can be assumed to be approximately constant at all energies. The discriminator edges for the proton detector in a fixed magnet-detector array system were set at 22 keV and 47 keV for P12 and 47 keV and 157 keV for P22 during this test. Table VI gives the count rates observed in P12 and P22 for various energies of protons. The broadening of the monoenergetic proton beam due to electronic noise and variations in dE/dx loss in the dead layer is the reason for these channels responding to proton energies above and below the predicted energy range values above.

H. Negative Response of Electron Channels to Protons

Tests with the proton source on the flight model magnet-detector array also show that none of the electron detector channels (E11, E21, E31, E12, E22, E32) respond to protons.

I. Electron Scattering into Proton Detector

Tests with the electron accelerator and β sources show that a small percentage of low energy electrons (<100 keV) are scattered in the proton detector. Using a Sr-90 and Pm-147 β-ray source (5125-3) and an electromagnet from the University of Minnesota electron spectrometer for OGO-I and -III satellites (Pfitzer, (1968)), various

E

TABLE V

ENERGY LOSSES IN ALUMINUM DEAD LAYER FOR PROTONS

Proton Energy (keV)	$\frac{dE}{dx}$ in Al. $(\frac{keV}{\mu g\text{-}cm^{-2}})$*	Energy Loss in $40 \mu g\text{-}cm^{-2}$ Dead Layer (keV)	Energy Loss in Detector Sensitive Volume (keV)
510	0.26	10	500
167	0.43-0.40	17	150
100	0.45	18 (max.)	82
67	0.43-0.40	17	50
32	0.35-0.26	12	20
20	0.26-0.20	9	11

*L.C. Northcliffe, (Subcommittee on Penetration of Charged Particles, (1964)).

TABLE VI

EXPERIMENTAL RESPONSE OF FLIGHT MODEL-FIXED

DETECTOR SYSTEM TO PROTONS

P12		P22	
Proton Energy (keV)	Counts/Sec	Proton Energy (keV)	Counts/Sec
17.5	2	35	5
20	40	40	50
25	1100	45	180
30	4000	50	350
35	7300	55	850
40	9700	60	1700
50	11000	70	3700
55	9400	80	4700
60	9500		
70	6100		
80	4000		

energies of electrons <100 keV were directed into the cooled fixed magnet-detector array of the prototype model in a forepump vacuum. For a selected electron energy of 40 keV and with the prototype E12 edges set at 33 and 49 keV and the prototype P12 edges set at 34 and 51 keV, 328 counts in 5 minutes were recorded in P12 with a background of 0 counts per minute in E12 and 1 count per minute in P12. Thus, the maximum percent of 40 keV electrons scattered into P12 compared to the number entering the magnet-detector array system is 7/335 x 100 or 2.1%. This is stated to be a maximum percentage because all 40 keV electrons entering the collimator may not be directed into and counted in E12. Similarly, from tests with the electron accelerator using the flight model fixed magnet-detector array, the number of electrons with energies <100 keV scattered into the P12 and P22 channels compared to the number of these electrons entering the magnet-detector array system was found to be less than 3%.

VIII. ELECTRON-PROTON SPECTROMETER CALIBRATIONS

A. Determination of Absolute Electron Fluxes of the Sr-90, Pm-147 Calibration Sources and Calculation of the Calibration Constants for the Electron-Proton Spectrometer

The calibration sources manufactured by Isotope Products Laboratories consist of two radioisotopes, Strontium (Sr-90) and Promethium (Pm-147), each with 240 microcurie activity. The Sr-90 isotope is in the form of strontium titanate dispersed in silver foil and covered with a bonded silver window. On top of this silver foil, the Pm-147 isotope is in the form of $PmCl_3$ as an evaporated salt sealed with epoxy resin binder. This double layered active deposit is mounted in a brass calibration source holder. (See Figure (21).) The active area of the source is approximately 0.24" in diameter. The half life of Sr-90 is 28.1 years and the half life of Pm-147 is 2.5 years.

The absolute electron fluxes for the calibration sources to be used with the ATS-F electron-proton spectrometer were determined in the following manner. A Kevex silicon-lithium drift semiconductor detector ($80mm^2$ - 5mm), thick enough to stop a 2.4 MeV beta particle in its active volume, was mounted inside a light tight aluminum box. A hole was drilled and tapped through a side of the box and the standard collimator of the ATS-F electron-proton spectrometer detector system was screwed tightly into the side of the box. The solid state detector was placed close to the opening of the collimator inside the box so that it completely filled the "look cone" through the collimator. Each calibration source (mounted in its permanent brass holder) was mounted in a special adapter which fits over the standard collimator end outside of the box and

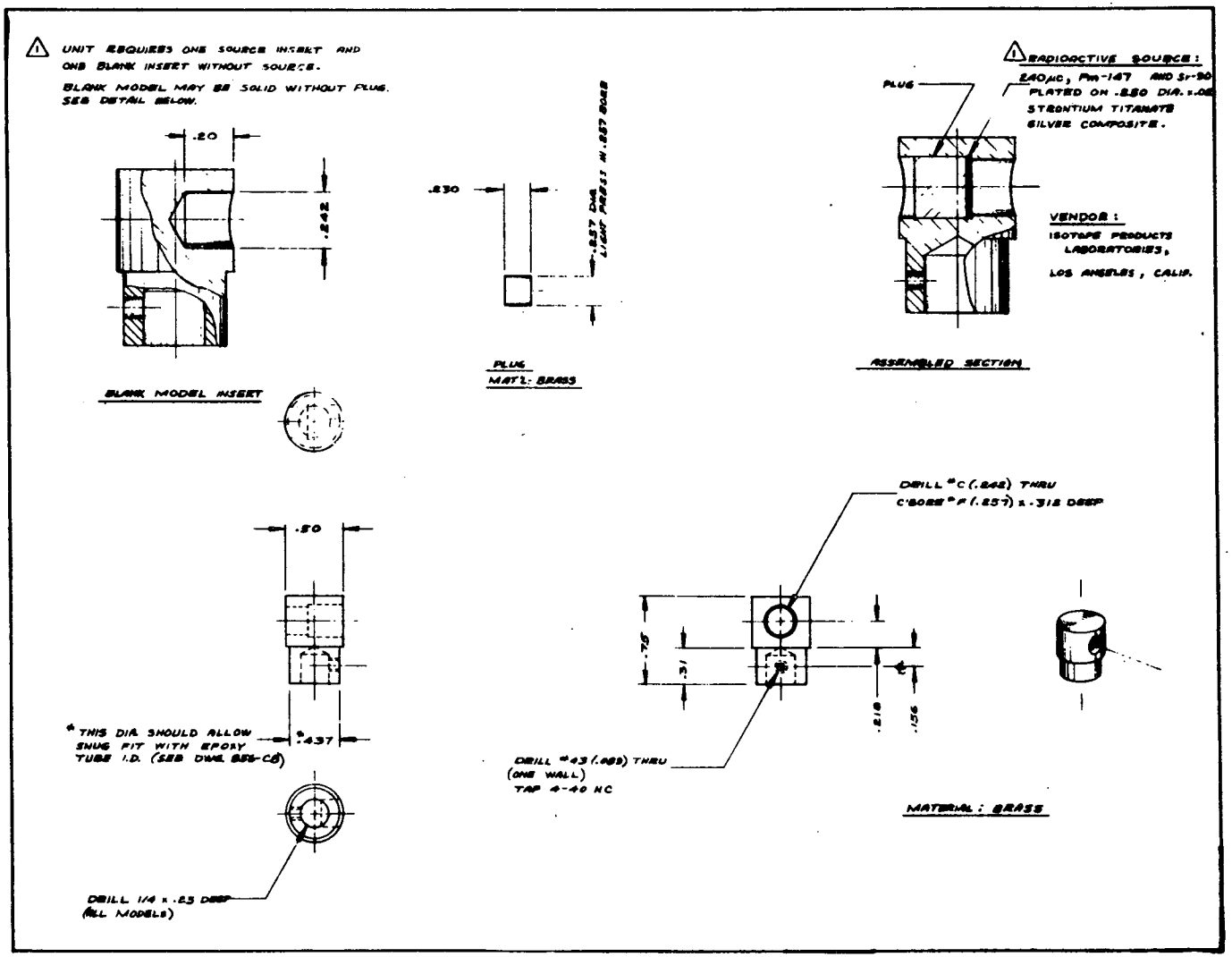
UNIT REQUIRES ONE SOURCE INSERT AND ONE BLANK INSERT WITHOUT SOURCE.
BLANK MODEL MAY BE SOLID WITHOUT PLUG. SEE DETAIL BELOW.
.20
.242
BLANK MODEL INSERT
.830
.827 DIA. LIGHT PRESS FIT W. .827 BORE
PLUG
MAT'L: BRASS
RADIOACTIVE SOURCE:
240μc, Pm-147 AND Sr-90
PLATED ON .250 DIA. x .08
STRONTIUM TITANATE
SILVER COMPOSITE.
PLUG
VENDOR:
ISOTOPE PRODUCTS LABORATORIES,
LOS ANGELES, CALIF.
ASSEMBLED SECTION
.50
* THIS DIA. SHOULD ALLOW SNUG FIT WITH EPOXY TUBE I.D. (SEE DWG. 855-CB)
.437
DRILL 1/4 x .25 DEEP (ALL MODELS)
DRILL #C (.242) THRU
C'BORE #F (.257) x .318 DEEP
.75
.31
.218
.136
DRILL #43 (.089) THRU (ONE WALL) TAP 4-40 NC
MATERIAL: BRASS

Figure (21)

places the active area of the calibration source so that it completely fills the "look cone" through the other end of the collimator. (See Figure 22). In a high vacuum bell jar, the spectrum of each calibration source was accumulated for 600 seconds live time with a pulse height analyzer. An Ortec pulser was calibrated with an electron accelerator up to 90 keV using this Si-Li detector-preamplifier-amplifier system. The results are given in Figure 23. The Ortec pulser, then, gives the calibration for this Si-Li detector system. The Si-Li detector system's response to higher energy electrons (>90 keV) can then be obtained to a good approximation by assuming that the pulser calibration is valid up to 2.3 MeV. The validity of the pulser calibration extension can be checked by comparison with the Si-Li detector system's response to Pm-147 and Sr-90. These beta particle sources have characteristic end point energies which can be compared to the extrapolated pulser settings. The end point energy is the maximum energy that can be departed to a beta particle in beta decay for a particular isotope. Figure 24 shows the comparison between the Si-Li detector system and pulse height analyzer response to the Ortec pulser and the end point energies of Pm-147 (229 keV) and Sr-90 (2.24 MeV). This response curve is used to convert the pulse height analyzer accumulation of the calibration source spectrums in terms of counts in 600 seconds in a given energy channel to counts in 600 seconds in a one keV energy interval. The calibration source spectrums in terms of counts accumulated in 600 seconds as a function of energy are given in Figures 25-29.

If N_i is the number of counts accumulated in an energy interval E_i(keV) in time t (seconds) and the collimator opening has a length l and an area A, then the average absolute flux of a calibration source for $A \ll l^2$ is:

$$\bar{J}_i = \frac{l^2 N_i}{A^2 t \Delta E_i} \tag{13}$$

For l = 2.54 cm (1.00")

A = 0.033 cm^2 (I.D.) = 0.081")

t = 600 sec

$$\bar{J}_i = 9.97\ N_i/\Delta E_i \quad (\text{electrons-cm}^{-2}\text{-sec}^{-1}\text{-ster}^{-1}\text{-keV}^{-1}) \tag{14}$$

For example, for the electron-proton spectrometer prototype calibration sources, the following absolute fluxes were determined:

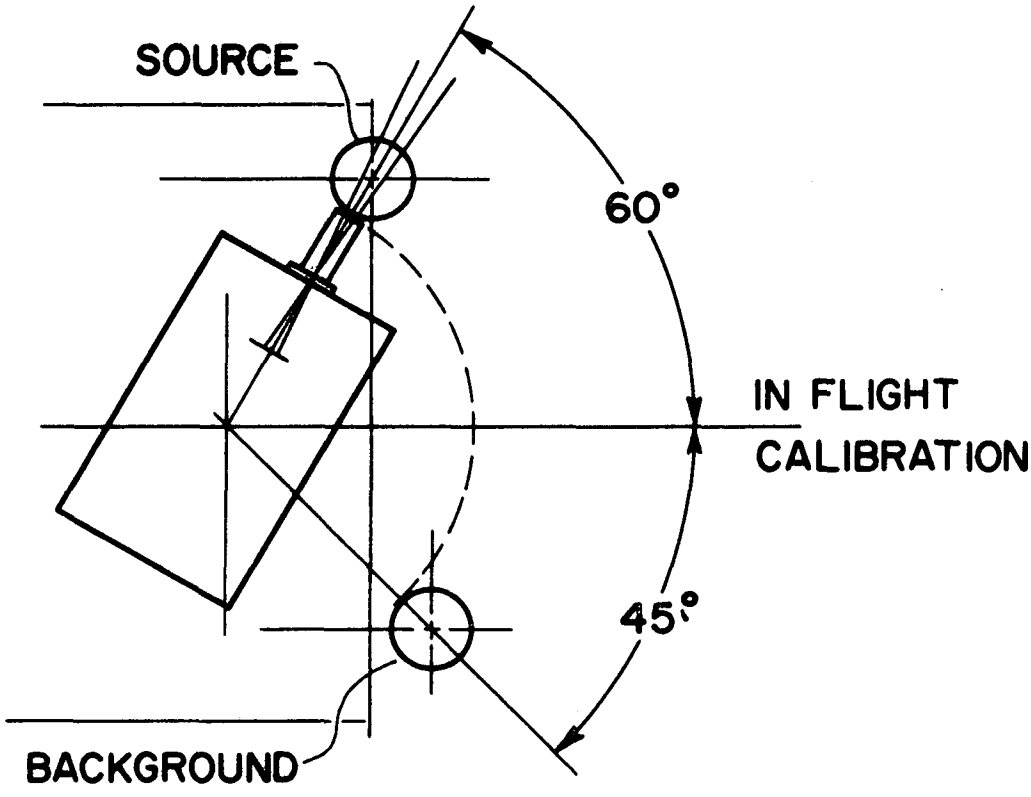
SOURCE
60°
IN FLIGHT
CALIBRATION
45°
BACKGROUND

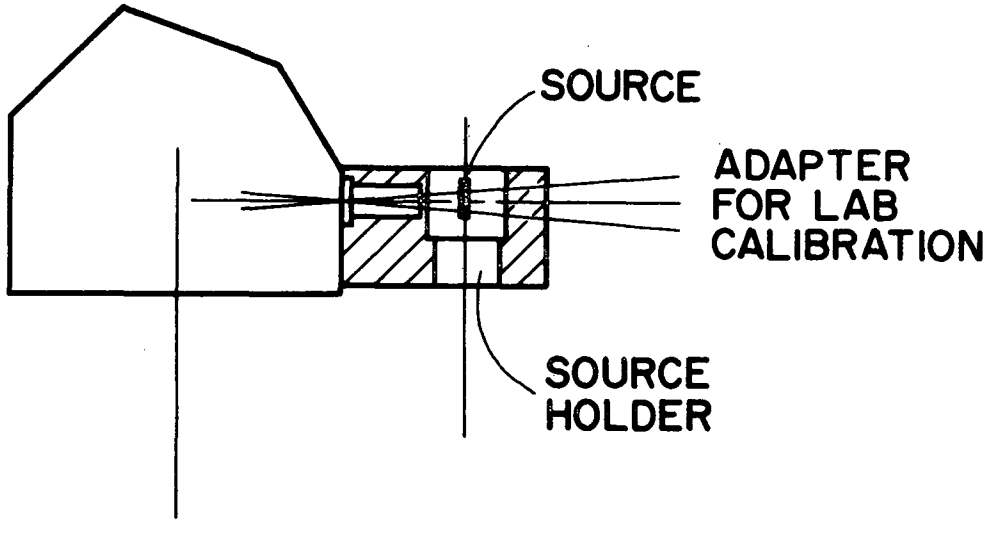
SOURCE
ADAPTER
FOR LAB
CALIBRATION
SOURCE
HOLDER

Figure (22)

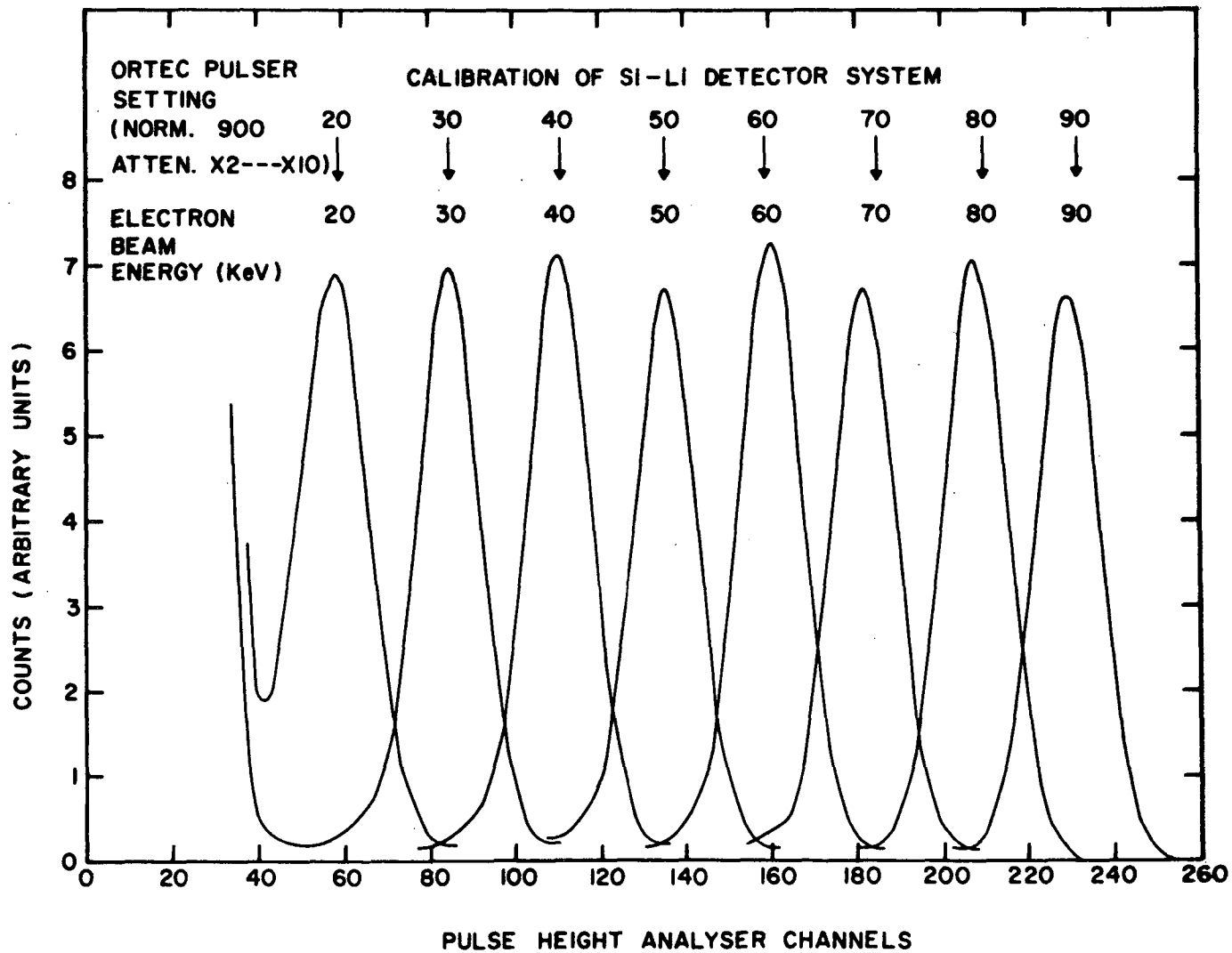
CALIBRATION OF SI-LI DETECTOR SYSTEM
ORTEC PULSER SETTING (NORM. 900 ATTEN. X2---X10)
20 30 40 50 60 70 80 90
ELECTRON BEAM ENERGY (KeV)
20 30 40 50 60 70 80 90
COUNTS (ARBITRARY UNITS)
0 1 2 3 4 5 6 7 8
0 20 40 60 80 100 120 140 160 180 200 220 240 260
PULSE HEIGHT ANALYSER CHANNELS

Figure (23)

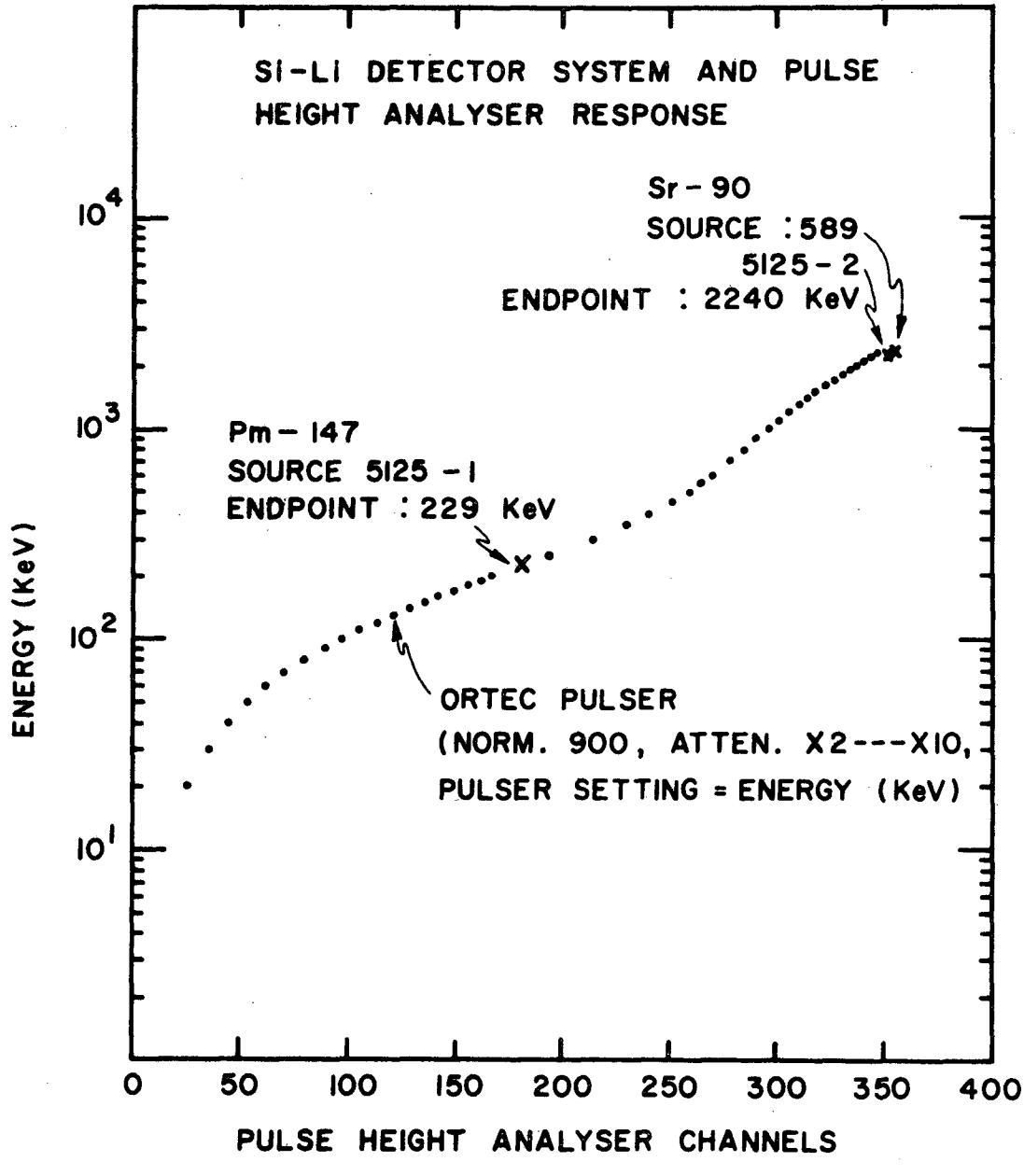
SI-LI DETECTOR SYSTEM AND PULSE HEIGHT ANALYSER RESPONSE
Sr - 90
SOURCE : 589
5125 - 2
ENDPOINT : 2240 KeV
Pm - 147
SOURCE 5125 - 1
ENDPOINT : 229 KeV
ORTEC PULSER
(NORM. 900, ATTEN. X2---X10,
PULSER SETTING = ENERGY (KeV)
ENERGY (KeV)
10^4
10^3
10^2
10^1
0
50
100
150
200
250
300
350
400
PULSE HEIGHT ANALYSER CHANNELS

Figure (24)

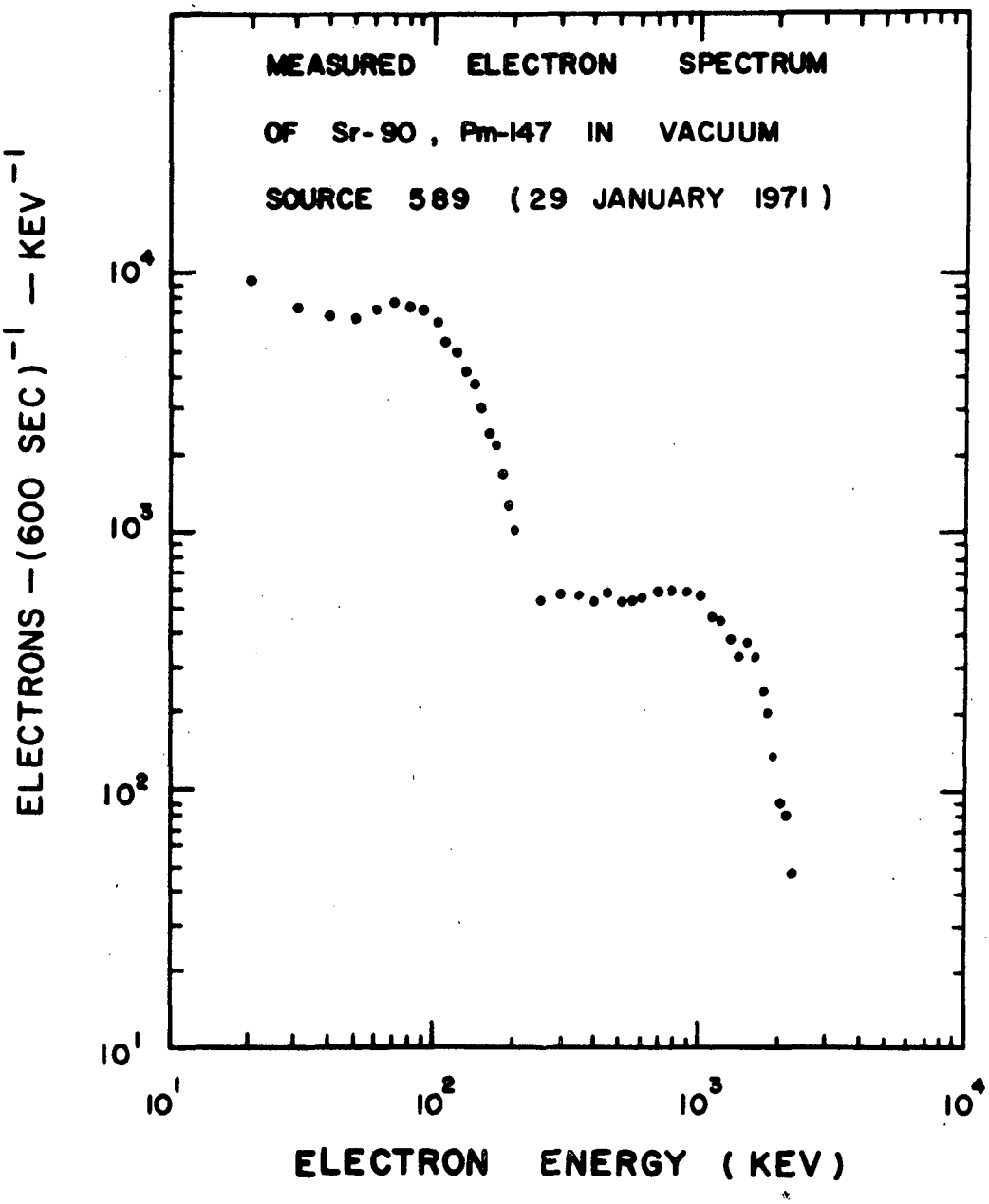
MEASURED ELECTRON SPECTRUM
OF Sr-90 , Pm-147 IN VACUUM
SOURCE 589 (29 JANUARY 1971)
ELECTRONS - (600 SEC)$^{-1}$ - KEV^{-1}
10^4
10^3
10^2
10^1
10^1
10^2
10^3
10^4
ELECTRON ENERGY (KEV)

Figure (25)

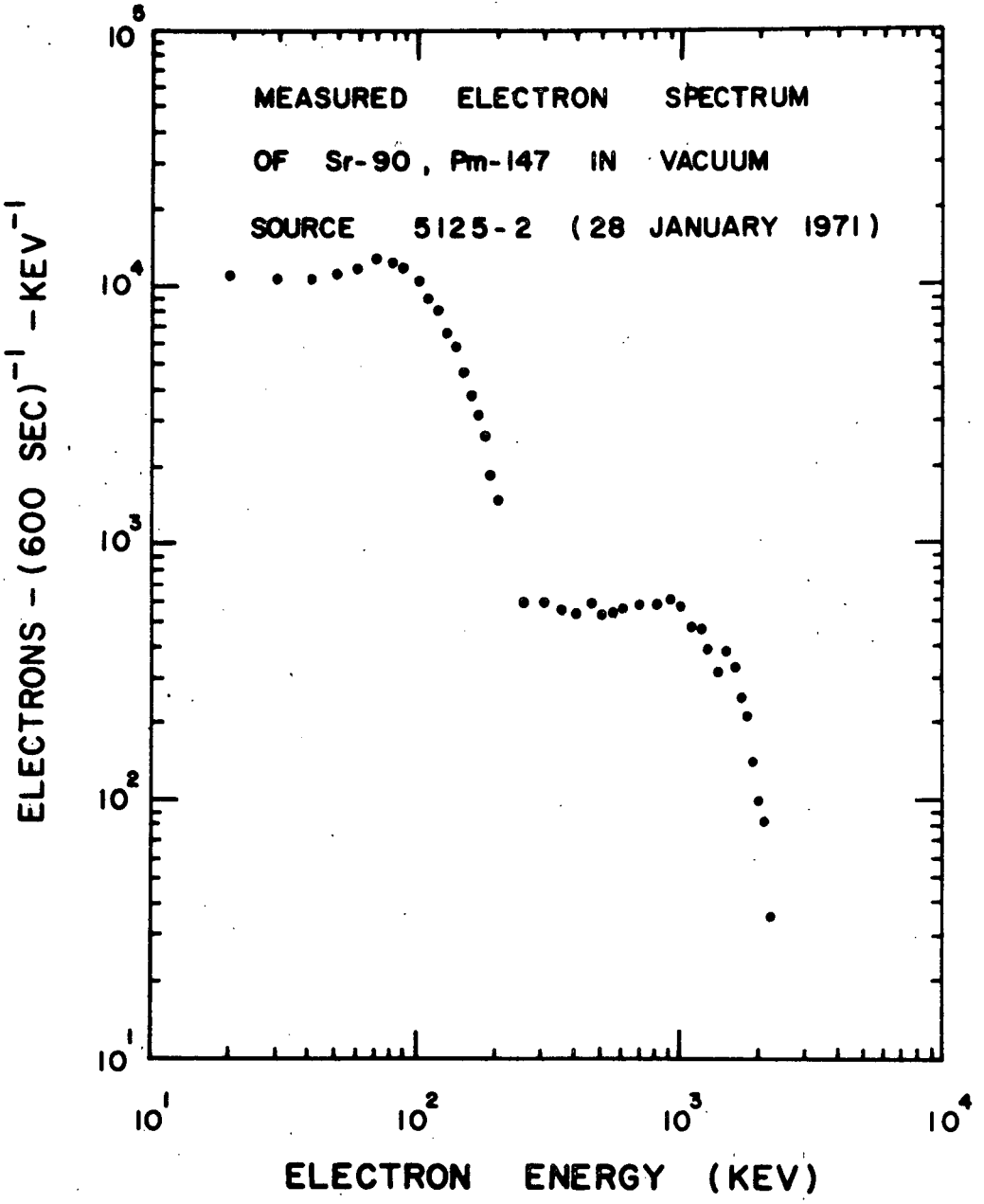
MEASURED ELECTRON SPECTRUM
OF Sr-90, Pm-147 IN VACUUM
SOURCE 5125-2 (28 JANUARY 1971)
ELECTRONS - (600 SEC)$^{-1}$ - KEV^{-1}
ELECTRON ENERGY (KEV)
10^5
10^4
10^3
10^2
10^1
10^1
10^2
10^3
10^4

Figure (26)

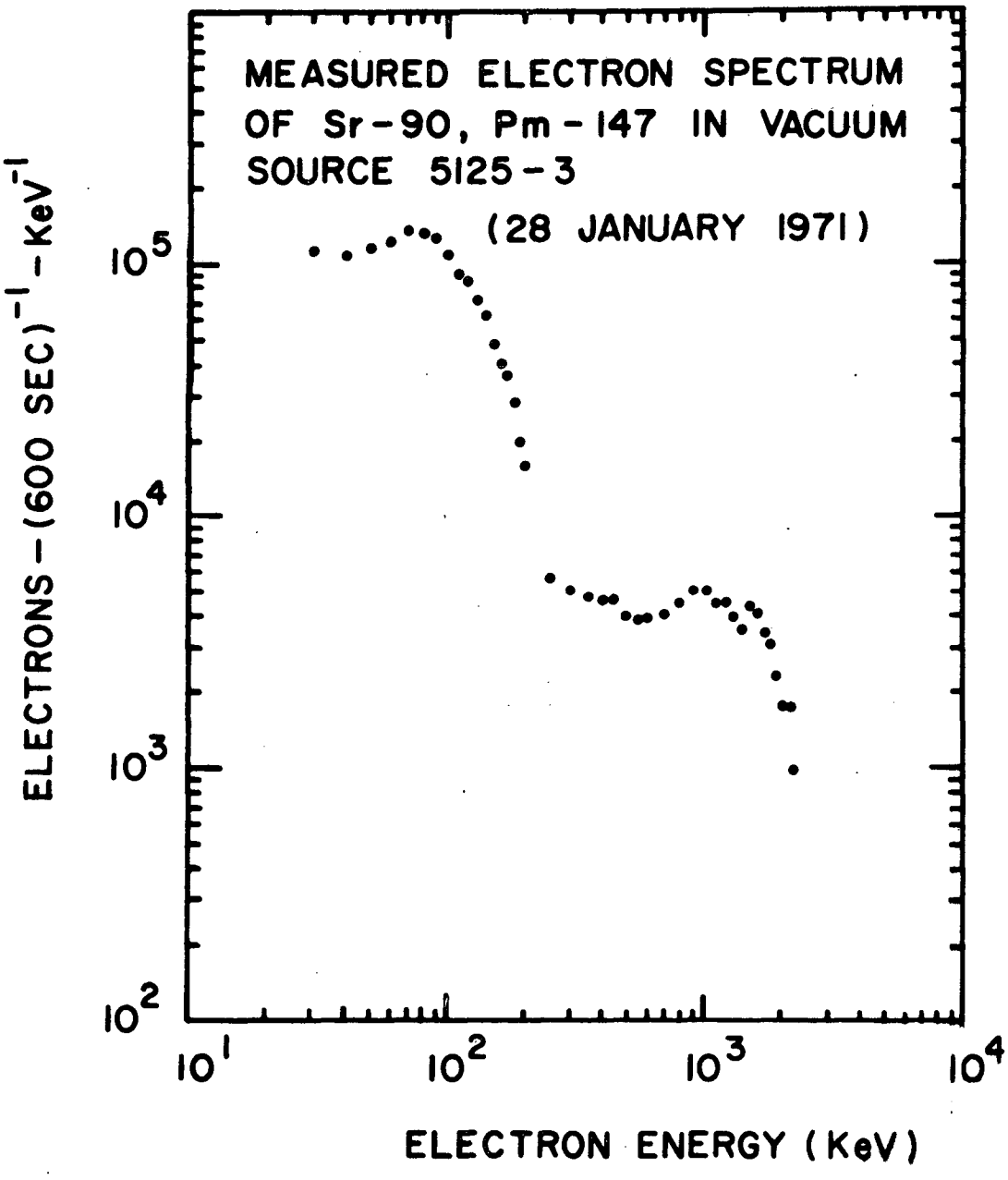
MEASURED ELECTRON SPECTRUM
OF Sr-90, Pm-147 IN VACUUM
SOURCE 5125-3
(28 JANUARY 1971)
ELECTRONS-(600 SEC)$^{-1}$-KeV^{-1}
10^5
10^4
10^3
10^2
10^1
10^2
10^3
10^4
ELECTRON ENERGY (KeV)

Figure (27)

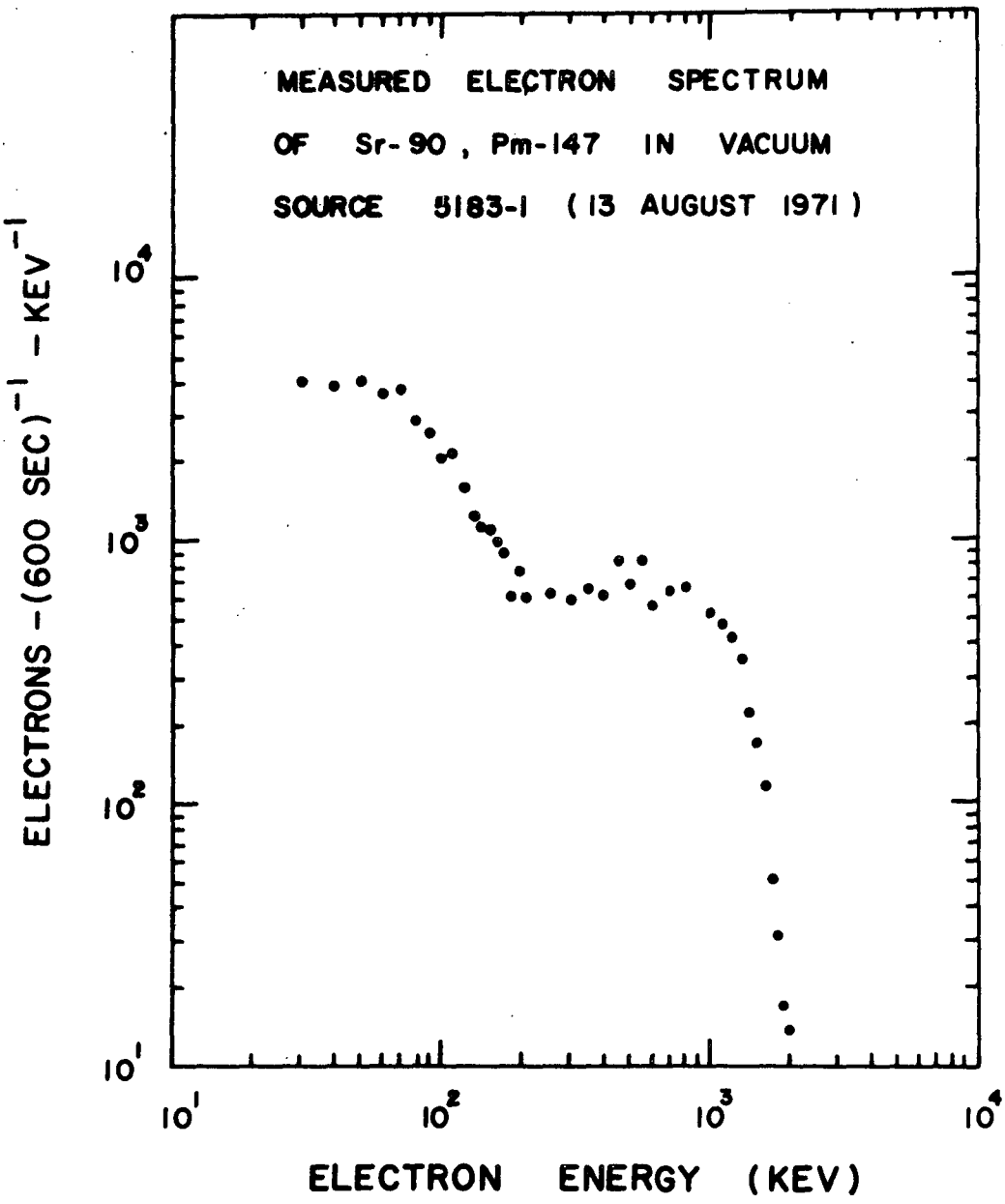
MEASURED ELECTRON SPECTRUM
OF Sr-90 , Pm-147 IN VACUUM
SOURCE 5183-1 (13 AUGUST 1971)
ELECTRONS - (600 SEC)$^{-1}$ - KEV^{-1}
10^4
10^3
10^2
10^1
10^1
10^2
10^3
10^4
ELECTRON ENERGY (KEV)

Figure (28)

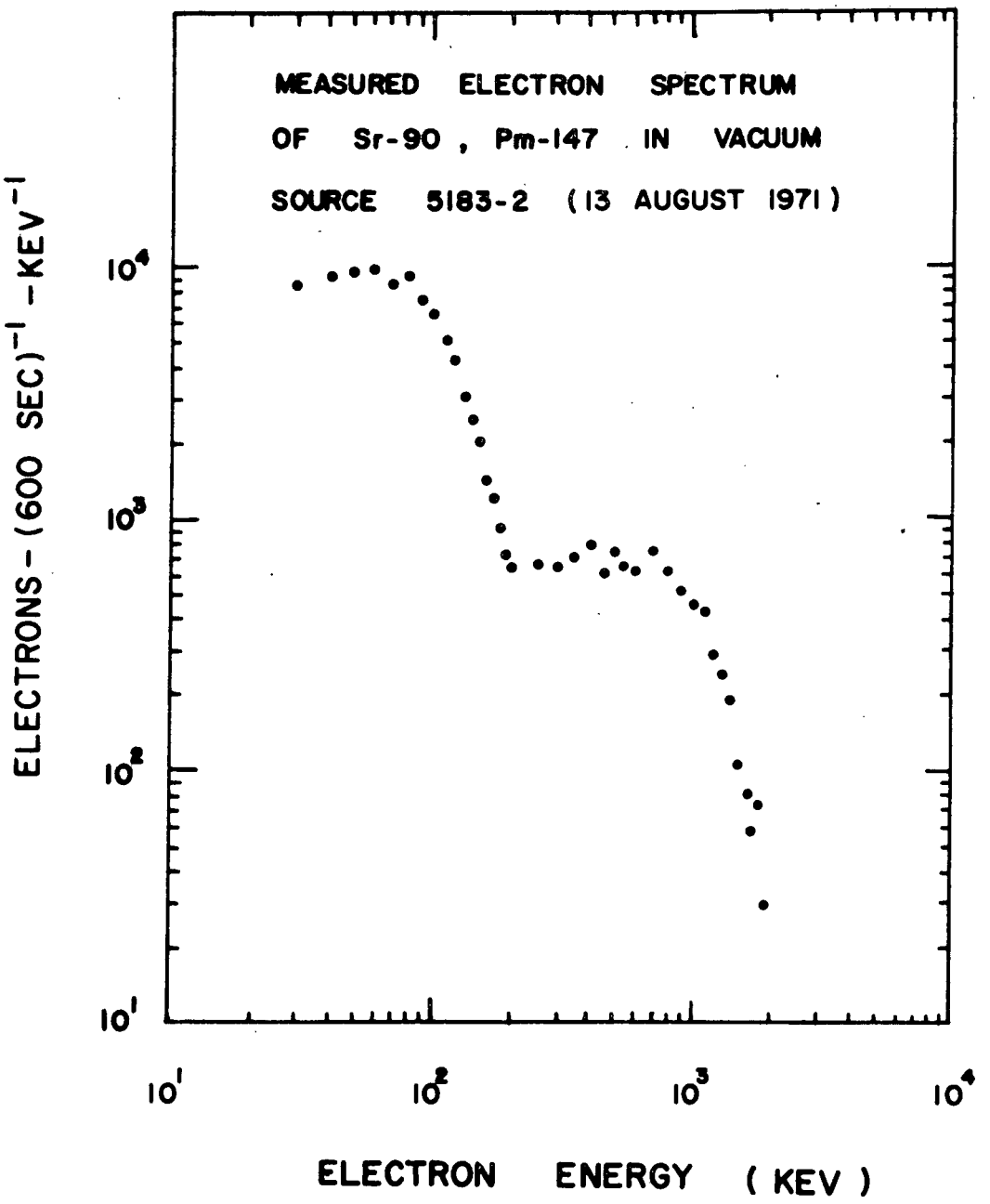
MEASURED ELECTRON SPECTRUM
OF Sr-90 , Pm-147 IN VACUUM
SOURCE 5183-2 (13 AUGUST 1971)
ELECTRONS - (600 SEC)$^{-1}$ - KEV^{-1}
10^4
10^3
10^2
10^1
10^1
10^2
10^3
10^4
ELECTRON ENERGY (KEV)

Figure (29)

Sr-90, Pm-147 Source #	Energy Range (keV)	E_i(keV)	N_i^*	$\bar{j}_i$
589	32-54	22	167,844	7.53×10^4
	150-196	46	93,530	2.01×10^4
	500-2240	1740	635,931	3.61×10^3
5125-2	36-54	18	229,805	1.26×10^5
	150-244	94	193,226	2.03×10^4
	500-2240	1740	641,120	3.64×10^3

*Spectrums accumulated 28-29 January 1971 for 600 seconds.

To obtain the calibration coefficients for the electron-proton spectrometer electron channels, the Sr-90, Pm-147 calibration source is placed in the tubular mounting post attached to the main electron-proton spectrometer electronics package for calibration of the scanning detector system. This mounting post holds the calibration source the same distance away from the collimator entrance as did the special adapter used with the Si-Li detector system. For the electron-proton spectrometer fixed detector system, the calibration source is mounted in the same special adapter as before which is pushed as far as possible onto the collimator. Thus, the active areas of the sources completely fill the "look cones" of their respective collimators on the scanning and fixed detector systems. (See Figure 22).

The unit is then placed in a high vacuum bell jar and counts in the six electron channels are accumulated for 600 seconds each. The results for the prototype model are as follows where N_j is the number of counts accumulated in the j^{th} spectrometer channel in 600 seconds:

	Channel	Energy Range (keV)*	N_j**
Source 589			
Scanning	E11	32-54	38,668
Detector	E21	150-196	38,523
System	E31	500-2240	62,639
Source 5125-2			
Fixed	E12	36-54	21,446
Detector	E22	150-244	56,039
System	E32	500-2240	66,612

The calibration constant for the $j^{\underline{th}}$ electron channel is given by:

$$C_E(j) = \frac{600\bar{j}_j}{N_j} \quad \{\frac{\text{electrons-cm}^{-2}\text{-sec}^{-1}\text{-ster}^{-1}\text{-keV}^{-1}}{\text{counts-sec}^{-1}}\} \qquad (15)$$

(Thus, for example, $C_E(E11) = \frac{(600)\ (7.53\text{x}10^4)}{38,668} = 1.17 \times 10^3$ $\frac{\text{electrons-cm}^{-2}\text{-sec}^{-1}\text{-ster}^{-1}\text{-keV}^{-1}}{\text{counts-sec}^{-1}}$.) The calibration constants for all of the prototype electron channels are given below:

$C_E(E11) = 1.17\text{x}10^3$ electrons-cm^{-2}-sec^{-1}-ster^{-1}-keV^{-1} / counts-sec^{-1}

$C_E(E21) = 3.13\text{x}10^2$ " "

$C_E(E31) = 3.46\text{x}10^1$ " "

$C_E(E12) = 3.53\text{x}10^3$ " "

$C_E(E22) = 2.17\text{x}10^2$ " "

$C_E(E32) = 3.28\text{x}10^1$ " "

---

*As determined by discriminator edge levels determined by a preliminary calibration using Ortec pulser settings: Norm. 890, Atten. x2---x10, Pulser setting = Energy (keV) and by the energy range response determined for each channel.

**Accumulated 18 February, 1971.

Thus, the average absolute flux of electrons in $j^{\underline{th}}$ channel is given by:

$$F_E(j) = \frac{C_E(j)N_E(j)}{t} \quad \{\text{electrons-cm}^{-2}\text{-sec}^{-1}\text{-ster}^{-1}\text{-keV}^{-1}\} \qquad (16)$$

where $N_E(j)$ is the number of observed counts in the $j^{\underline{th}}$ channel in time t in seconds. These calibration coefficients are only preliminary and will have to be repeated before the instrument flies.

These calibration coefficients are spectrally dependent, of course. The spectra of the Sr-90, Pm-147 calibration sources are not exactly like the low energy dominant, power law spectrum in the radiation belts at synchronous orbit. However, these calibration coefficients give an acceptable approximation to the true absolute fluxes of electrons at synchronous orbit.

Since essentially 100% of the protons entering through the collimator enter the proton detector, the calibration coefficients for converting observed count rates in the proton energy channels to absolute fluxes is given in the following manner. If $N_p(i)$ is the observed number of counts accumulated in time t (seconds) in an energy interval ΔE_i(keV) in the $i^{\underline{th}}$ channel, and l and A are defined as above, then the average absolute flux of protons in the $i^{\underline{th}}$ channel is:

$$F_p(i) = \frac{l^2}{A^2} \frac{N_p(i)}{t\Delta E_i} \quad . \qquad (17)$$

It should be noted that these calibration coefficients have to be corrected for an additional effect which causes the spectrometer to count a lower rate than it should. This correction is for the circuit dead time and is explained in Section XC. Also, it should be noted that these calibration coefficients reflect a temporary effect existing with the prototype model. Some pulses that should be counted in the E11, E12, P11, and P12 channels of the prototype model are not counted because the window width is so narrow that the noise adds or subtracts to a pulse and throws it out of the window. This effect causes these channels to be more inefficient. This temporary effect will be changed before the unit flies when the windows are adjusted to the proper settings.

The scanning and fixed detector systems must also be intercalibrated in order to compare their responses in flight. The electron channels of the prototype scanning and fixed detector systems have been intercalibrated by accumulating the count rate from one β source (Sr-90, Pm-147: #589) on both systems in a forepump vacuum. With the discriminator edges set as labeled (which excludes noise from counting in the windows), the counts in 30 seconds in each electron channel are given below:

Prototype Model Intercalibration

(In vacuum; 3 Sept. 1971)

Source: #589

	Channel	Energy Range (keV)*	Counts/30 sec.
Scanning	E11	32-47	1139
Detector	E21	150-187	1990
System	E31	500-2240	3262
Fixed	E12	34-50	1559
Detector	E22	150-229	3545
System	E32	500-2240	3724

The proton channels are difficult to intercalibrate accurately for lack of a fixed intensity proton source. However, since the magnetic field in the air gap has little effect on protons and the fixed and scanning detector array systems are identical, as a first approximation the proton channels are directly comparable if the discriminators are set at the same levels and the detectors are cooled below 0°C so that the detector noise levels are low and comparable.

B. Pulser Calibration for Testing and Determination of Electronic Discriminator Edges.

An Ortec pulser is used extensively to test the response of the circuitry and in the setting ofthe electronic discriminator edges. The Ortec pulser puts out a pulse that very closely resembles a pulse from an electron or proton losing its energy in a surface barrier detector. These test pulses are put into the circuit just before the preamplifiers. The connectors for the test pulse inputs are located on the preamplifier covers attached to the magnet-detector array assembly. The connectors will be covered with a screw-on metal cap during flight.

The Ortec pulser is calibrated in terms of electron energies lost in the surface barrier detectors. The 0-125 kV electron accelerator was used to give monoenergetic electron energy loss peaks between 35 and 70 keV in the E1 detector of the engineering model. Then, the pulser amplitude was adjusted so that its pulse height distribution matched the pulse height distribution of the monoenergetic

*As determined by discriminator edge levels determined by the calibration of the Ortec pulser as in Figure 30 in Section X-B and by the energy range response determined for each channel.

electron energy loss. Figure 30 shows the resulting pulser settings corresponding to 35, 40, 50, 60 and 70 keV electron loss peaks in the E1 detector of the engineering model and the matched pulse height distributions. In this energy range, the electrons are deflected directly into the E1 detector and lose their full energy in the E1 detector. This calibration of the pulser was done at several different times with the engineering model E1 detector with the resulting pulser settings varying $\pm$ 5%.

The pulser settings corresponding to higher energies of electron losses are extrapolated linearly. The linearity of the pulser output was checked by comparison of the pulse heights of the extrapolated pulser settings to the pulse heights of the known end point energies of Pm-147 (229 keV) and Sr-90 (2.24 MeV) as shown in Figure 24. The pulser pulse heights were found to agree with the end point energy pulse heights to within the 5% accuracy of the pulser calibration.

The voltage levels of the electronic discriminators are adjusted by changing the value of a resistor in each discriminator circuit. The calibrated Ortec pulser is used to determine the equivalent electron energy loss in a surface barrier detector which has a pulse height equal to the voltage level of the electronic discriminator. This determination of discriminator levels in terms of equivalent electron energies is done in the following manner. The Ortec pulser puts out pulses with a monoenergetic pulse height at the rate of 60 per second. The electronic noise of the system broadens these monoenergetic pulses into a Gaussian type distribution such that one-half of the pulse heights fall below and one half fall above the most probable pulse height of the distribution. For each discriminator level, the Ortec pulser setting is found such that its pulse height distribution is centered on the discriminator level. For discriminator levels which are high enough so that the electronic noise of the system does not trigger the discriminator, this centering of the pulser pulse height distribution corresponds to 30 pulses per second falling above the discriminator level and triggering the discriminator. If there were no electronic noise broadening in the system, all of the monoenergetic pulses from the pulser would have the pulse height of the peak of the broadened distribution which is centered on the discriminator level. From the pulser calibration curve, the electron energy loss corresponding to this pulser setting is found. Thus, the discriminator levels are determined by their corresponding electron energy loss pulse heights and can be labeled by these corresponding energies, such as the 20 keV discriminator level. Table VII gives the desired discriminator edge settings to be used for flight.

C. Calibration of Counting Capabilities and Circuit Dead Time.

The circuit dead time prevents all of the input pulses of proper pulse height from the detectors to become output pulses. A pulse occurring within the dead time after a preceding pulse will not

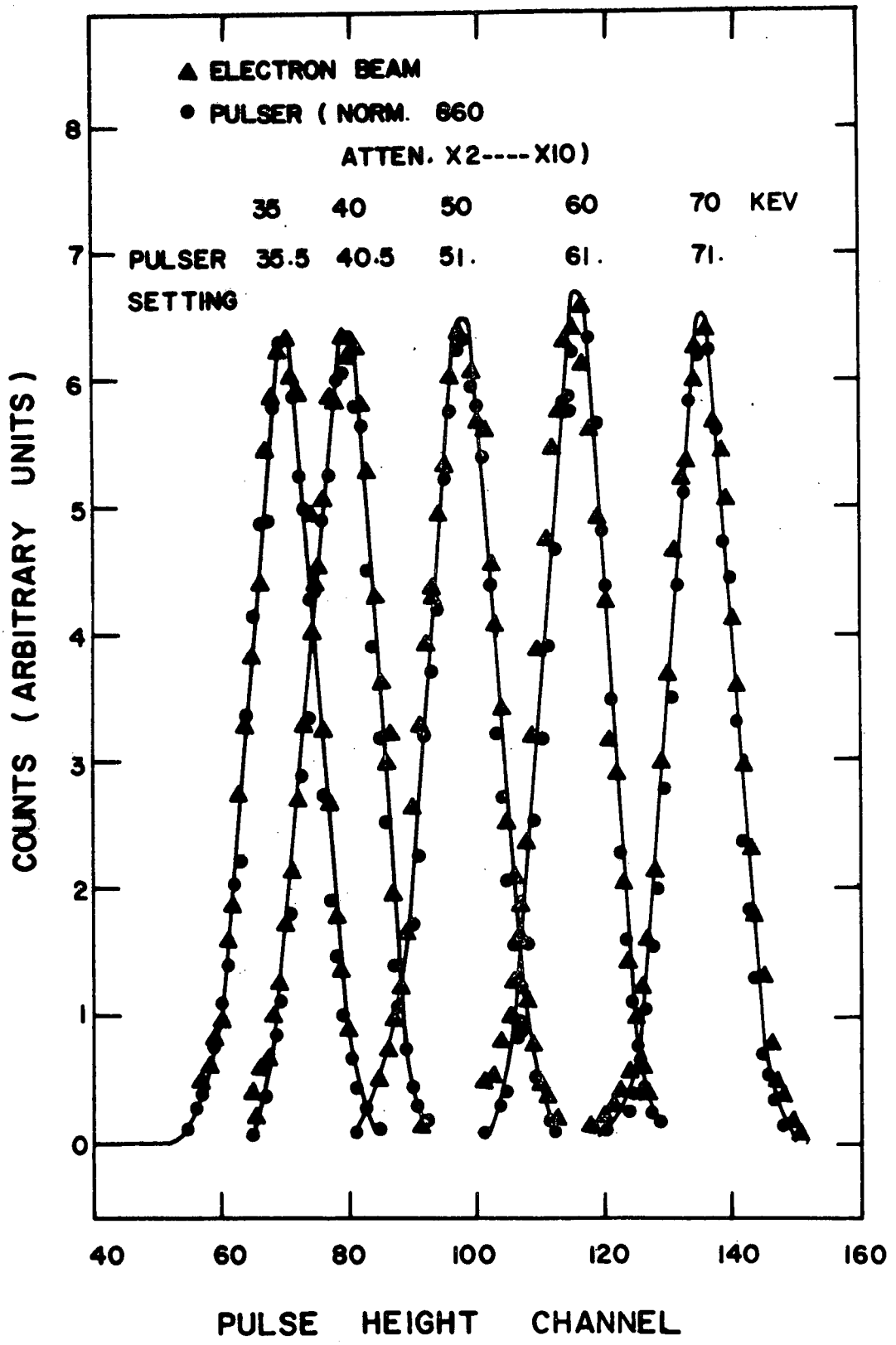
▲ ELECTRON BEAM
● PULSER (NORM. 660
ATTEN. X2----X10)
35 40 50 60 70 KEV
PULSER 35.5 40.5 51. 61. 71.
SETTING
COUNTS (ARBITRARY UNITS)
0 1 2 3 4 5 6 7 8
40 60 80 100 120 140 160
PULSE HEIGHT CHANNEL

Figure (30)

TABLE VII

DISCRIMINATOR EDGE SETTINGS FOR FLIGHT*

Energy Channels	Discriminator Edge	Energy Setting of Edge (keV)	Ortec Pulser Setting (Norm. 860, Atten. x2---x10)
E11, E12	LOWER	25	25.5
	UPPER	50	51
E21, E22	LOWER	120	122
	UPPER	200	203
E31, E32	LOWER	60	61
P11, P12	LOWER	20	20.5
	UPPER	50	51
P21, P22	LOWER	50	51
	UPPER	150	152
P31, P32	LOWER	150	152
	UPPER	500	507

*To be set during final refurbishing.

generate an output pulse because the circuit has not recovered to the point where it is capable of generating an output pulse. This effect especially becomes important when the count rate is high enough that the probability of two or more pulses occurring within a time interval equal to the dead time becomes significant.

This circuit dead time can be approximated by several methods. One method is to use a double pulser which puts out two pulses with a variable delay between them. The time interval between the two pulses is shortened until the second pulse just ceases to be counted. Another method is to use a random pulse generator with a substantial number of input pulses and observe the output pulses on a scope. Triggering the scope on the output pulses, the time delay, after the triggering pulses until the next pulses appear and recover to their full amplitude, is approximately equal to the circuit dead time. A third method is to use a random pulse generator and measure the input pulse rate versus the output pulse rate. Then, the following equations lead to the dead time $\Delta\tau$:

$$I = O + I^2\Delta\tau \tag{18}$$

$$\Delta\tau = \frac{1 - O/I}{I} \tag{19}$$

where I = input rate, O = output rate, $I^2\Delta\tau$ = the accidental rate or uncounted rate. In all three of these methods, the pulse height should be adjusted to be in the center of the respective discriminator windows.

Using a Datapulse model 110B pulser in the double pulse mode, the first method gives the dead time for the E12 channel of the prototype model to be 10μ seconds. Using the second method with a random noise generator triggering the Datapulse 110B pulser, the dead time for the E12 channel of the prototype model is 12μ seconds. The results of the third method using the random noise generator to trigger the Datapulse 110B pulser to give input pulses to the prototype model are shown in Figure 31. There is an additional effect in the E11, E12, P11, P12 channels besides the dead time which reduces the output count rate. The E11, E12, P11, P12 windows on the prototype are set narrower than they would be for flight, and the detectors are noisier than for a flight model, so that the noise, adding and subtracting randomly from the signal pulse, causes some pulses to have pulse heights too high or low to be counted in the discriminator window. This effect should be a fixed percentage of the number of input pulses and can be corrected for. Depending on what percentage is used for correction, the dead time for E12 of the prototype model using the third method is approximately 8-10μ seconds.

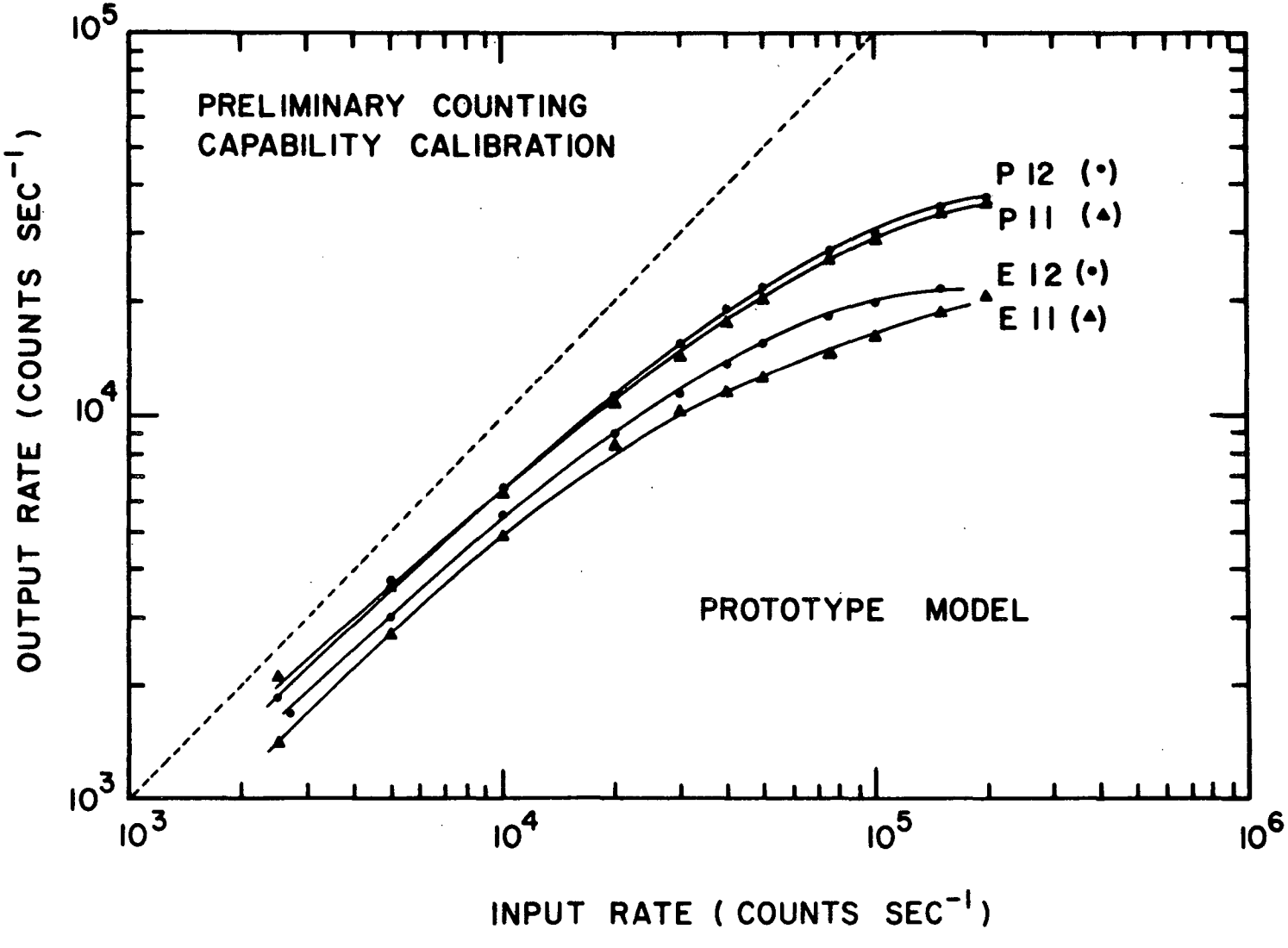
PRELIMINARY COUNTING
CAPABILITY CALIBRATION
P 12 (•)
P 11 (▲)
E 12 (•)
E 11 (▲)
PROTOTYPE MODEL
OUTPUT RATE (COUNTS SEC⁻¹)
INPUT RATE (COUNTS SEC⁻¹)
10³
10⁴
10⁵
10⁶

Figure (31)

D. Operational Test.

The procedure for performing the operational test on the ATS-F electron-proton spectrometer is outlined in detail in the Experiment Handbook. Basically, it consists of operating the instrument with a spacecraft simulator and output monitor or GSE (Ground Support Equipment) using a Sr-90 and Pm-147 β-ray calibration source on each detector system as a stimulus for all the electron and proton energy channels. The test is performed at room temperature and atmospheric pressure. Table VIII summarizes the resulting count rates for the prototype model determined on 4 May 1971 using the Sr-90, Pm-147 calibration sources 589 for the scanning detector array and 5125-2 for the fixed detector array in air at room temperature. The resulting count rates for the flight model, determined on 7 March 1973 using the calibration sources 5183-2 for the scanning detector array and 5183-1 for the fixed detector array for both air and vacuum at room temperature are given in Table IX. These numbers will change with time as the calibration sources naturally decay. Sr-90 has a half life of 28.1 years and Pm-147 has a half life of 2.5 years.

E. Scanning Detector Array Look Direction -Shaft Encoder Calibration.

As was mentioned previously in this paper, the look direction of the scanning detector array is determined by an optical encoder system which essentially measures the angular position of the shaft on which the scanning detector array is attached. The shaft encoder readout consists of four binary digits corresponding to 2^3, 2^2, 2^1, 2^0. Thus, the possible readouts in equivalent decimal numbers extends from 0 to 15. The shaft encoder system is adjusted so that nominally at each 15° position from EME north to south through west, the shaft encoder will read outthe binary equivalent to the decimal numbers from 0 at north to 12 at south. At intermediate positions between these nominal 15° steps, it is possible for the shaft encoder to read out numbers not corresponding to either of the two angular positions that the detector array is looking between. This happens because more than one binary digit has to change in order to read out the next position. Table X gives a preliminary calibration of the shaft encoder readouts in 1° increments for the prototype scanning detector array. Note, for example, the shaft encoder readouts between angles 182° to 190°. In changing from position 1100 (12) to position 1011 (11), three binary digits must change. However, the shaft encoder system is such that the three digits do not change at the same angular position. Thus, at 183°, the shaft encoder reads 1110 (14), and at 184°-189°, it reads 1010 (10). If the scanning detector array happens to change its nominal detented position from the 15° step intervals during flight, the true look position can be deduced from the sequence of shaft encoder readouts using this type of calibration. (The calibration in Table X is only preliminary and must be repeated before the unit is flown.)

TABLE VIII

PROTOTYPE MODEL
(4 May 1971)

OPERATIONAL TEST RESULTS
(In Air)

Sr-90, Pm-147 Source 589 Scanning Detector Array		Sr-90, Pm-147 Source 5125-2 Fixed Detector Array	
Energy Channel	Counts 10 Seconds	Energy Channel	Counts 10 Seconds
E11	15-250	E12	5-150
E21	356±70	E22	349±70
E31	1209±125	E32	1239±125
P11	300-700	P12	300-700
P21	2142±200	P22	2221±200
P31	371±75	P32	381±75

OPERATIONAL TEST RESULTS
(In Vacuum, Room Temperature)

TABLE IX

FLIGHT MODEL
(7 March 1973)

OPERATIONAL TEST RESULTS
(In Air, Room Temperature)

Sr-90, Pm-147 Source 5183-2 Scanning Detector Array		Sr-90, Pm-147 Source 5183-1 Fixed Detector Array	
Energy Channel	Counts 10 Seconds	Energy Channel	Counts 10 Seconds
E11	10-50	E12	5-50
E21	200-280	E22	200-270
E31	1000-1170	E32	860-1040
P11	300-500	P12	350-500
P21	1800-2050	P22	1620-1860
P31	330-470	P32	250-350

OPERATIONAL TEST RESULTS
(In Vacuum, Room Temperature)

Sr-90, Pm-147 Source 5183-2 Scanning Detector Array		Sr-90, Pm-147 Source 5183-1 Fixed Detector Array	
Energy Channel	Counts 10 Seconds	Energy Channel	Counts 10 Seconds
E11	200-620	E12	50-130
E21	390-510	E22	340-480
E31	1170-1350	E32	970-1150
P11	350-570	P12	350-520
P21	2030-2330	P22	1770-2040
P31	370-490	P32	280-380

TABLE X

PRELIMINARY SHAFT ENCODER CALIBRATION
(Prototype Scanning Detector)

Position (Degrees)	Shaft Encoder	Position (Degrees)	Shaft Encoder	Position (Degrees)	Shaft Encoder	Position (Degrees)	Shaft Encoder
N360	0000	337	0010	314-	0011	291	0100
359	0000	336	0010	313	0011	290	0100
358-	0000	335	0010	312	0011	289	0100
357	0000	334	0010	311	*0111	288	0101
356	0000	333	0010	310	*0110	287	0101
355	0000	332	0010	309	*0110	286-	0101
354	0000	331-	0010	308	*0110	285	0101
353	0000	330	0010	307	*0110	284	0101
352	0000	329	0010	306	*0110	283	0101
351	0000	328	0010	305	*0110	282	0101
350	0000	327	0010	304	0100	281	0101
349	0000	326	0010	303	0100	280	0110
348	0001	325	0010	302	0100	279	0110
347	0001	324	0010	301	0100	278	0110
346	0001	323	0010	300	0100	277	0110
345	0001	322	0010	299-	0100	276	0110
344-	0001	321	0010	298	0100	275	0110
343	0001	320	0010	297	0100	274	0110
342	0001	319	0010	296	0100	273	0110
341	*0011	318	0011	295	0100	272	0110
340	*0011	317	0011	294	0100	271	0110
339	0010	316	0011	293	0100	W270-	0110
338	0010	Bkd315	0011	292	0100	269	0110

*Intermediate, irregular reading -Detented position in scanning

TABLE X (Cont'd)

PRELIMINARY SHAFT ENCODER CALIBRATION
(Prototype Scanning Detector)

Position (Degrees)	Shaft Encoder	Position (Degrees)	Shaft Encoder	Position (Degrees)	Shaft Encoder	Position (Degrees)	Shaft Encoder
268	0110	245	*1110	223	1001	201	1010
267	0110	244	*1110	222	1001	200	1010
266	0110	243	*1010	221	1001	199	1010
265	0110	242	1000	220	*1011	198	1010
264	0110	241	1000	219	1010	197	1011
263	0110	240-	1000	218	1010	196	1011
262	0110	239	1000	217	1010	195-	1011
261	0110	238	1000	216	1010	194	1011
260	0110	237	1000	215	1010	193	1011
259	0110	236	1000	214	1010	192	1011
258	0110	235	1000	213	1010	191	1011
257	0111	234	1000	212	1010	190	1011
256	0111	233	1000	211	1010	189	*1010
255	0111	232	1000	Cal210-	1010	188	*1010
254-	0111	231	1000	209	1010	187	*1010
253	0111	230	1000	208	1010	186	*1010
252	0111	229	1000	207	1010	185	*1010
251	*1111	228	1000	206	1010	184	*1010
250	*1111	227	1001	205	1010	183	*1110
249	*1110	226	1001	204	1010	182	1100
248	*1110	225-	1001	203	1010	181	1100
247	*1110	224	1001	202	1010	S180-	1100
246	*1110						

*Intermediate, irregular reading -Detented position in scanning

F. Calibration of Thermistors.

All of the thermistors used in the prototype and flight models of the electron-proton spectrometer were calibrated at the same time at temperatures varying from +60°C to -20°C before they were installed into the units. The thermistors were heat sunk to a brass block whose temperature was controlled and measured. Each thermistor was connected in series with a known fixed resistance and a constant voltage of 6.2V was maintained across the two resistances by a Zener diode voltage regulator. The voltage drop across each thermistor was then measured at various temperatures. The results are shown in Figure 32. In addition, a calibration curve calculated from the manufacturer's specifications is also shown in Figure 32.

G

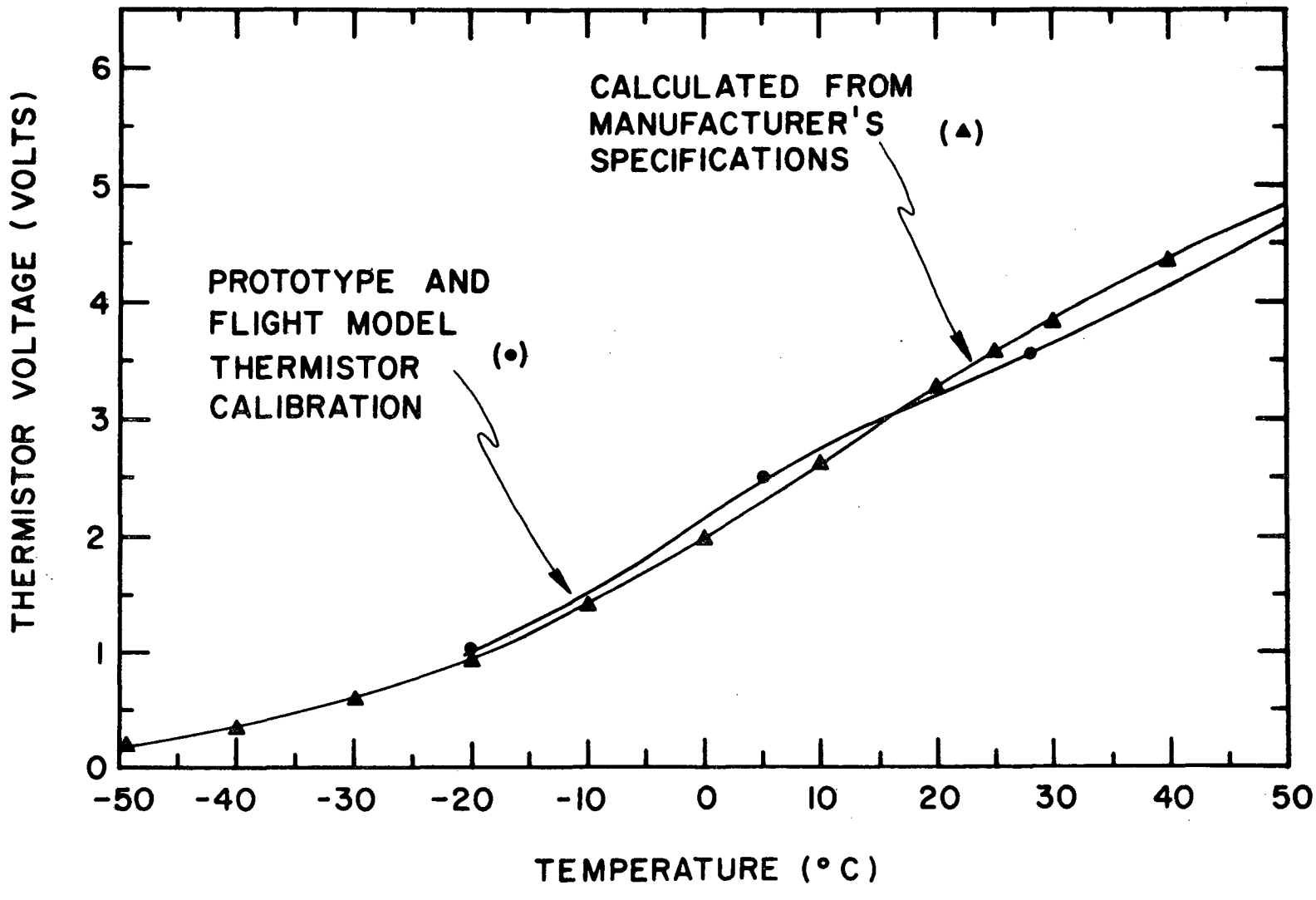
CALCULATED FROM
MANUFACTURER'S
SPECIFICATIONS
(▲)
PROTOTYPE AND
FLIGHT MODEL
THERMISTOR
CALIBRATION
(•)
THERMISTOR VOLTAGE (VOLTS)
0
1
2
3
4
5
6
-50
-40
-30
-20
-10
0
10
20
30
40
50
TEMPERATURE (°C)

Figure (32)

IX. CONCLUSION AND DISCUSSION

The electron-proton spectrometer in its final design satisfactorily fulfills its original purpose. Electrons and protons are distinguished from each other and their fluxes are measured in three energy ranges each. Time variations characteristic of these energy ranges for electrons and for protons in the outer radiation belt can be studied. Data from a magnetometer on board in addition to the directional capabilities of the electron-proton spectrometer will allow pitch angle calculations to be made and used in correlation with the electron-proton spectrometer data.

Before the electron-proton spectrometer is put into orbit, several pre-flight procedures for refurbishment must be carried out. These are listed in Table XI.

TABLE XI

PRE-FLIGHT REFURBISHMENT PROCEDURES

1. Some surface barrier detectors may have to be replaced with spares as listed in Table III in Section V-E if they are found to be noisy.

2. The discriminator edges will have to be adjusted to the values given in Table VII in Section VIII-B.

3. The scanning and fixed magnet-detector array system calibration coefficients will have to be determined according to the procedure in Section VIII-A.

4. The counting capability curves to correct for circuit dead time will have to be determined according to the procedure in Section VIII-C.

5. The shaft encoder calibration will have to be determined as described in Section VIII-E.

6. The scanning and fixed magnet-detector array systems will have to be intercalibrated with the same calibration source in a vacuum with the detectors cooled to $\approx 0^{\circ}C$.

7. The prototype and flight unit magnet-detector systems should all be intercalibrated with the same source in a vacuum with the detectors cooled to $\approx 0^{\circ}C$.

X. Bibliography

Akasofu, S. I., Polar and magnetospheric substorms, D. Reidel Publishing Co., Dordrecht, Holland, 1968.

Arnoldy, R. L., R. A. Hoffman and J. R. Winckler, Observations of the Van Allen radiation regions during August and September 1959, Part 1, J. Geophys. Res., 65, 1361, 1960.

Bertolini, G. and A. Coche, Semiconductor detectors, North-Holland Publishing Company, 1968.

Bostrom, C. O., D. S. Beall and J. C. Armstrong, Time history of the inner radiation zone, October 1963 to December 1968, J. Geophys. Res., 75, 1246, 1970.

Cladis, J. B., L. F. Chase, W. L. Imhof and D. J. Knecht, Energy spectrum and angular distribution of electrons trapped in the geomagnetic field, J. Geophys. Res., 66, 2297, 1961.

Davis, L. R. and J. M. Williamson, Low-energy trapped protons, Space Research, 3, 365, 1963.

Davis, L. R., R. A. Hoffman and J. M. Williamson, Observations of protons trapped above 2 earth radii, Trans. Am. Geophys. Union, 45, 84, 1964.

Dearnaley, G. and D. C. Northrop, Semiconductor counters for nuclear radiations, John Wiley and Sons, Inc., 1966.

DeForest, S. E. and C. E. McIlwain, Plasma clouds in the magnetosphere, J. Geophys. Res., 76, 3587, 1971.

Frank, L. A., J. A. Van Allen and H. K. Hills, A study of charged particles in the earth's outer radiation zone with Explorer XIV, J. Geophys. Res., 69, 2171, 1964.

Frank, L. A., On the extraterrestrial ring current during geomagnetic storms, J. Geophys. Res., 72, 3753, 1967.

Frank, L. A., Direct detection of asymmetric increases of extraterrestrial ring current proton intensities in the outer radiation zone, J. Geophys. Res., 75, 1263, 1970.

Freden, S. C. and R. S. White, Protons in the earth's magnetic field, Phys. Rev. Letters, 3, 9, 1959.

Goddard Space Flight Center, The ATS-F and -G data book, Goddard Space Flight Center, Greenbelt, Maryland, 20771, 1971.

Gross, W. C., Two-directional focusing of charged particles with a sector-shaped uniform magnetic field, Rev. Sci. Instr., 22, 717, 1951.

Hendrickson, R. A., R. W. McEntire and J. R. Winckler, Electron Echo experiment: a new magnetospheric probe, Nature, 230, 564, 1971.

Hess, W. N., The radiation belt and the magnetosphere, Blaisdel Publishing Co., 1968.

Johnson, J. B., Thermal agitation of electricity in conductors, Phys. Rev., 32, 97, 1928.

Lezniak, T. W., An experimental study of magnetospheric motions and the acceleration of energetic electrons during substorms, Ph.D. Thesis, School of Physics and Astronomy, University of Minnesota, Minneapolis, Minnesota 55455, 1970.

Lezniak, T. W. and J. R. Winckler, Experimental study of magnetospheric motions and the accelerations of energetic electrons during substorms, J. Geophys. Res., 75, 7075, 1970.

Melissinos, A. C., Experiments in modern physics, Academic Press, 1968.

Mihalov, J. D. and R. S. White, Low-energy proton radiation belts, J. Geophys. Res., 71, 2207, 1966.

Nakada, M. P. and G. D. Mead, Diffusion of protons in the outer radiation belt, J. Geophys. Res., 70, 4777, 1965.

O'Brien, B. J., Review of studies of trapped radiation with satellite-borne apparatus, Space Sci. Rev., 1, 415, 1962a.

O'Brien, B. J., Direct observations of dumping electrons at 1000-Kilometer altitude and high latitudes, J. Geophys. Res., 67, 1227, 1962b.

O'Brien, B. J., Lifetimes of outer zone electrons and their precipitation into the atmosphere, J. Geophys. Res., 67, 3687, 1962c.

O'Brien, B. J., High latitude geophysical studies with satellite Injun 3. 3. Precipitation of electrons into the atmosphere, J. Geophys. Res., 69, 13, 1964.

Ortec Incorporated, Instruction manual surface barrier detectors, Ortec Incorporated, 1970.

Pftizer, K. A., An experimental study of electron fluxes from 50 keV to 4 MeV in the inner radiation belt, Ph. D. Thesis, Technical Report CR-123, School of Physics and Astronomy, University of Minnesota, Minneapolis, Minnesota 55455, 1968.

Pfitzer, K. A. and J. R. Winckler, Experimental observation of a large addition to the electron inner radiation belt after a solar flare event, J. Geophys. Res., 73, 5792, 1968.

Subcommittee on Penetration of Charged Particles, Committee on Nuclear Science, Studies in penetration of charged particles in matter, National Academy of Sciences - National Research Council, Report Number 39, Publication 1133, 1964.

Thomas and Skinner, Inc., Permanent magnet design, Bulletin M303, Thomas and Skinner, Inc., Indianapolis, Indiana.

Van Allen, J. A., G. H. Ludwig, E. C. Roy and C. E. McIlwain, Observation of high intensity radiation by satellites 1958 Alpha and Gamma, Jet Propulsion, 588, 1958.

Van Allen, J. A. and L. A. Frank, Radiation around the earth to a radial distance of 107,400 Km, Nature, 183, 430, 1959.

Van Allen, J. A., The first public lecture on the discovery of the geomagnetically trapped radiation, State University of Iowa Report, 60-13, 1960.

Vernov, S. N. and A. E. Chudakov, Terrestrial corpuscular radiation and cosmic rays, Space Res., I, 751, 1960.

Westinghouse Defense and Space Center, Systems Development Division, Operations manual for the ATS-F/EME, Westinghouse Defense and Space Center, Baltimore, Maryland, Revised September 24, 1971.

Winckler, J. R., The origin and distribution of energetic electrons in the Van Allen radiation belts, presented at the Summer Advanced Study Institute, Earth's Particles and Fields, August 4-15, 1969, University of California, Santa Barbara; also published as Technical Report CR-144, School of Physics and Astronomy, University of Minnesota, Minneapolis, Minnesota 55455, 1969.

XI. APPENDIX I

SCAN MECHANISM DESIGN

The initial design of the scan mechanism was predicated on minimizing the size and power requirements for the instrument. In retrospect, this resulted in the selection of a stepper motor which would have operated satisfactorily in laboratory environments but had insufficient torque margin to overcome the increased frictional loads encountered in the use of lubricants suitable for space environments. By the time this problem was uncovered, increasing the size of the stepper motor would have required a major packaging redesign and power increase and was not a feasible solution. Thus, efforts were directed at minimizing the friction in the mechanism and reducing the variations in the friction during environmental testing. The untimely death of the chief mechanical designer at this time made the design analysis extremely difficult.

The initial design had a single bearing at two points on a rigid shaft. These bearings were pre-loaded. Initially the unit scanned properly after alignment and lubrication with light machine oil. The bearings and gears then were lubricated with a dry Vac Kote* molybdenum di-sulfide process. The initial treatment was totally unsatisfactory with excessive amounts of torque needed to move the shaft. After extensive work with BBRC on the problem the performance was improved to the point that the mechanism would operate satisfactorily for extended periods, but then develop sticky spots and resultant erratic stepping. It was found the lubricant tended to flake off or form rough bumps in the bearing races which increased the friction. The problem increased severely with vibration testing.

Based on discussion with staff members of Illinois Institute of Technology Research Institute and Goddard Space Flight Center personnel, it was decided to eliminate the Vac Kote process and install self-lubricating retainers of the shaft and stepper motor bearings. This did significantly reduce the friction in the mechanism; however, the unit again failed to scan properly after vibration testing. The single bearing at the bottom of the shaft still received excessive pounding during vibration and was found to be very rough to the touch.

The design was modified to incorporate two sets of preloaded pairs of bearings. Each set supported a section of the shaft which was now a two piece design. To allow axial expansion and contraction of the shaft and housing, a diaphragm was installed between the two shaft

---

* Proprietary process for lubrication of moving parts in high vacuum by Ball Brothers Research Corporation (BBRC), Boulder, Colorado.

sections. With some analysis and experimentation with various thicknesses, a .003" diaphragm of stainless steel was selected. This design has satisfactorily passed the necessary vibration tests. The unit did not, however, satisfactorily function during the cold operation test during EME Qualification testing. Due to differences in the rate of thermal expansion of the materials used in the bearing housing additional loading of the bearings occurred, causing the failure. To minimize this problem the bearing housing was again modified. It was further discovered that if careful attention were paid to bearing load distribution (particularily in a vibration environment) that the bearing pairs could be installed unloaded. This configuration performed satisfactorily in both thermal vacuum and vibration environments. Because of the large uncertainties in the vibration levels at our interface the new design was qualified at 1-1/2 times the levels given in GSFC Specification S-320-ATS-2D (as Modified for the University of Minnesota Experiment). The final design configuration is shown in Figure 33.

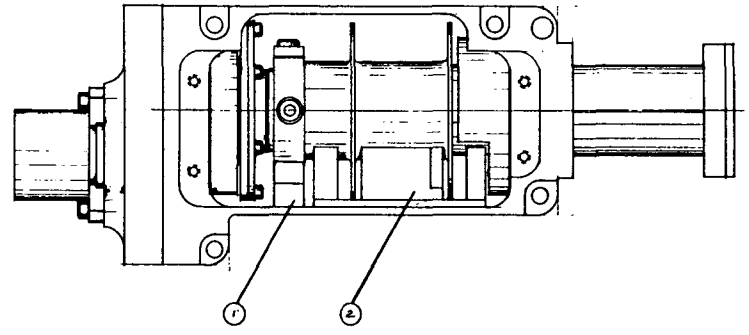

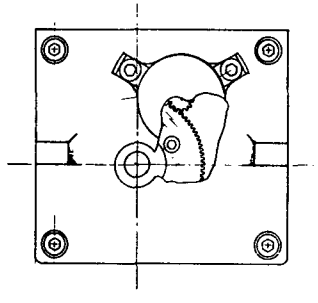

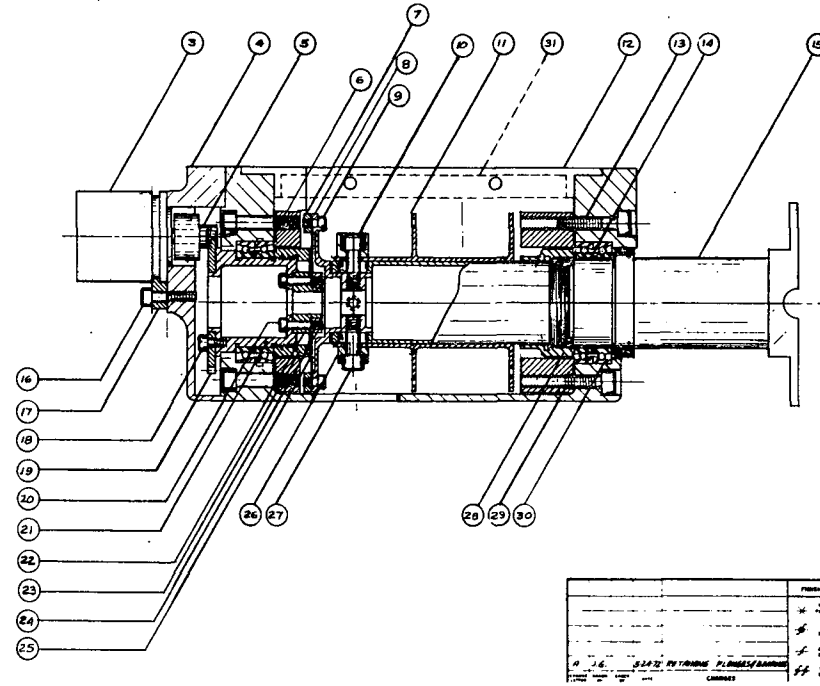

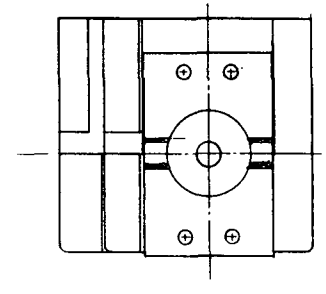

			4386	5590	MOTORIZED DETECTOR SCANNING MECH. ASSEMBLY
					ATS-F SATELLITE PROGRAM
					DOUBLE — DEPARTMENT OF PHYSICS, UNIVERSITY OF MINNESOTA, MINNEAPOLIS
					GELAND — 5-11-71 — B56-D11A

XII. APPENDIX II

ELECTRON ENERGY LOSS CALCULATIONS AND EXPERIMENTAL RESPONSE OF E3 AND P CHANNELS

A. Selection of Detector and Absorber Thicknesses.

The thicknesses of the P detector and the absorber between the P and E3 detectors were chosen such that a 500 keV electron would be able to penetrate these two layers of material and lose approximately 100 keV in the E3 detector. The range of a 500 keV electron is approximately 660μ in silicon. To lose 100 keV in the E3 detector, the 500 keV electron must lose 400 keV in the P detector and absorber and enter the E3 detector with 100 keV. The range of a 100 keV electron in silicon is approximately 56μ. Thus, the P detector and absorber must have the combined depth of the equivalent of 660μ minus 56μ or 604μ of silicon.

The proton detector could have been chosen to be approximately 604μ in depth. However, there is a problem in doing that. 604μ is approximately the range for a 470 keV electron. Thus, all electrons with 470 keV or less which enter the proton detector would be stopped in the detector and would be counted spuriously as protons of the same energy. The magnet sweeps essentially all of the electrons with <200 keV away from the P detector but allows increasing numbers of electrons into the P detector as their energy increases towards 500 keV. Only about 1/4 of the 500 keV electrons entering through the collimator are directed into the P detector. Thus, the most significant contributors to these spurious counts in the P detector would be the higher energy electrons just below 500 keV.

The problem is satisfactorily solved by choosing the P detector to be approximately 200μ deep and the absorber to be approximately equivalent to 400μ of silicon. The 200μ of silicon is the range of a 225 keV electron. Electrons with energies between 225 and 500 keV will pass through the P detector and lose lower amounts of energy in the P detector as the electron energy approaches 500 keV. A 500 keV electron loses approximately 80 keV in the P detector, and a 300 keV electron loses approximately 100 keV in the P detector by dE/dx energy losses. Thus, the higher energy electrons in the range 200-500 keV which are relatively more important in producing spurious counts in the P detector now give spurious pulses which appear in the P detector as protons with energies less than 100 keV. These spurious pulses are now less significant because of the spectrum of the electrons and protons at synchronous orbit. Using the assumption that the flux of electrons around 400 to 500 keV during magnetic storm times is approximately 10 times less than the flux of protons around 80 to 90 keV during magnetic quiet times, and since less than approximately a fifth of the 400-500 keV electrons enter the P detector and essentially

all of the protons enter the P detector, the spurious count rate in the P detector from electrons with <500 keV (excluding electrons scattered in) will almost always be less than 2% of the true proton count rate.

The absorber between the P and E3 detectors is a 0.020" epoxy board disk. An experimental determination of the density of the epoxy board material gives its density to be 1.79 ± 0.03 g/cm^{-3}. Using 2.33 g/cm^{-3} as the density of silicon, the equivalent thickness of the epoxy disk in terms of thickness of silicon can be determined by the following equation:

$$0.020\text{" epoxy} \times \frac{1.79\ g/cm^{-3}(\text{epoxy})}{2.33\ g/cm^{-3}(\text{Si})} = 0.0154\text{" Si} = 0.0390\ \text{cm Si} = 390\mu\ \text{Si} \qquad (20)$$

The final selection of P and E3 detector and absorber depths, therefore, includes a 200μ (Si) P detector, and equivalent of 390μ Si absorber, and a 300μ (Si) E3 detector.

B. Electron Energy Loss in E3.

With this arrangement, the 590μ equivalent depth of silicon will prevent ≈460 keV electrons from entering the E3 detector. 500 keV electrons will lose ≈115 keV in the E3 detector upon penetrating (660μ - 590μ = 70μ) approximately 70μ into the E3 detector. The maximum amount of energy lost in the E3 detector will come from the electron which is just stopped in the back of the E3 detector, or, in other words, the electron which has a range of 890μ of Si. This corresponds to an ≈620 keV electron. Since the 620 keV electron is just stopped at the back of the E3 detector, it loses an amount of energy in the E3 detector corresponding to an electron with a range of 300μ Si. Thus, the 620 keV electron loses ≈290 keV in the E3 detector. All energies of electrons between 500 and 620 keV are stopped in the E3 detector and, typically, lose amounts of energy from ≈115 keV up to ≈290 keV in the E3 detector. Electrons with energies higher than ≈620 keV begin to pass through the E3 detector. Because of their higher energy and corresponding greater velocity, these electrons >620 keV experience a smaller and smaller dE/dx energy loss in E3 as their energy increases. This decrease in dE/dx energy loss continues for electron energies only up to ≈1 MeV at which energy the electrons become "minimum ionizing" electrons. The dE/dx energy loss for a given thickness of silicon levels off at a minimum value and stays approximately constant with just a gradual upswing for electrons between 1 and 10 MeV. Thus, for example, 1-2 MeV electrons lose ≈105 keV in the E3 detector and a 5 MeV electron loses ≈114 keV in the E3 detector. These calculated energy losses in E3 for the typical detector thicknesses are summarized in Figure 19 in Section VII.

Remembering that the calculated dE/dx losses are only representative of the typical energy lost for given energy electrons, the true spread in energies of dE/dx losses for given energy electrons must be determined experimentally. The resulting dE/dx energy losses from various energies of electrons $\geq$ 500 keV in a 300μ thick, totally depleted surface barrier detector are shown in Figures 34 and 35. Note that the peaks of these energy loss distributions agree fairly well with the calculated dE/dx energy losses. These experimental data were obtained by using the OGO-I and OGO-III electron spectrometer electromagnet designed by Dr. Karl A. Pfitzer (Pfitzer, (1968)) to select various energies of a Sr-90 beta source placed over the entrance collimator. The 300μ thick surface barrier detector was placed directly over the exit opening of the electromagnet. The test was conducted at atmospheric pressure in air. Note that the majority of the dE/dx energy losses fall between roughly 70 and 180 keV in this 300μ detector. The error bar in Figure 19 in Section VII shows this experimentally observed energy spread in dE/dx losses for the E3 detector.

C. Electron Energy Loss in P.

The energy losses in the P detector from electrons >500 keV can also be calculated from the dE/dx versus energy curve for electrons in silicon given in the Ortec Surface Barrier Detector Instruction Manual. For a sensitive depth of 200μ (Si), 500 keV electrons would have a dE/dx energy loss of ≈80 keV. As explained in the previous paragraph, the dE/dx energy loss decreases with increasing energy down to the minimum energy lost by a "minimum ionizing" electron with energies of 1-2 MeV. These 1-2 MeV electrons lose ≈ 70 keV in the P detector and 5 MeV electrons lose ≈76 keV in the P detector.

In order to determine the true dE/dx energy loss spread in the P detector (200μ thick) from electrons >500 keV, one can approximate that the energy loss values will be two-thirds of that observed experimentally in the 300μ thick detectors as shown in Figures 34 and 35. Thus, the majority of the dE/dx energy losses in a 200μ thick detector from electrons >500 keV would fall between ≈45 and 120 keV. Since the P2 energy window is from 50-150 keV, the majority of the dE/dx energy losses from electrons >500 keV would fall thus in the P2 window.

D. Dead Layer Effects for Electrons.

It should be noted that the dead layers of the surface barrier detectors are not significant in computing the energy losses for electrons in the stacking arrangement of the P detector, absorber, and E3 detector. The depth of a surface barrier detector is given in terms of the sensitive depletion depth of silicon. The dead layer for totally depleted detectors consists mainly of the aluminum and gold surface contacts which are 40 $\pm$ 1 $\mu g/cm^{-2}$ each. Thus, for

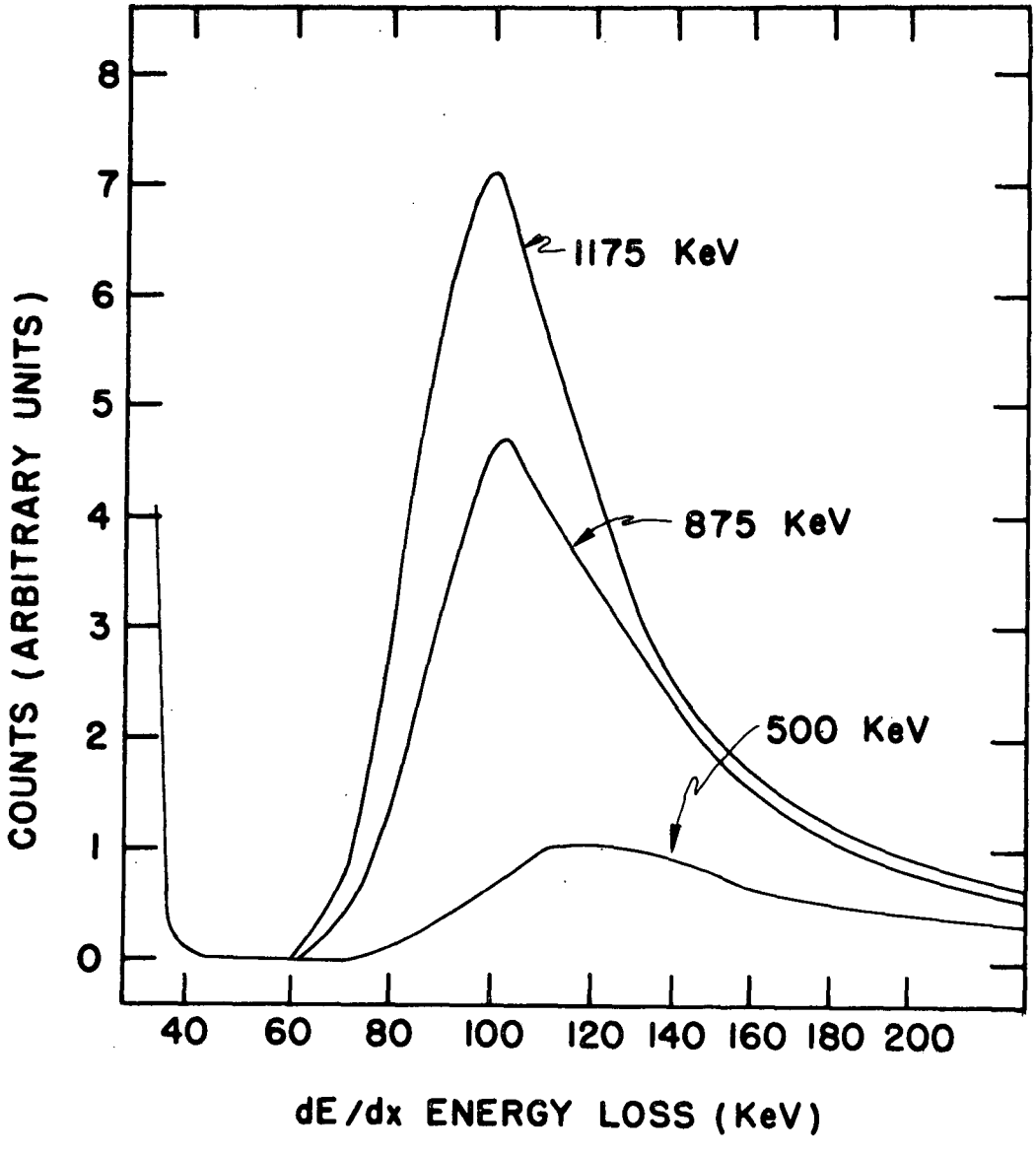
COUNTS (ARBITRARY UNITS)
0
1
2
3
4
5
6
7
8
40
60
80
100
120
140
160
180
200
dE/dx ENERGY LOSS (KeV)
1175 KeV
875 KeV
500 KeV

Figure (34)

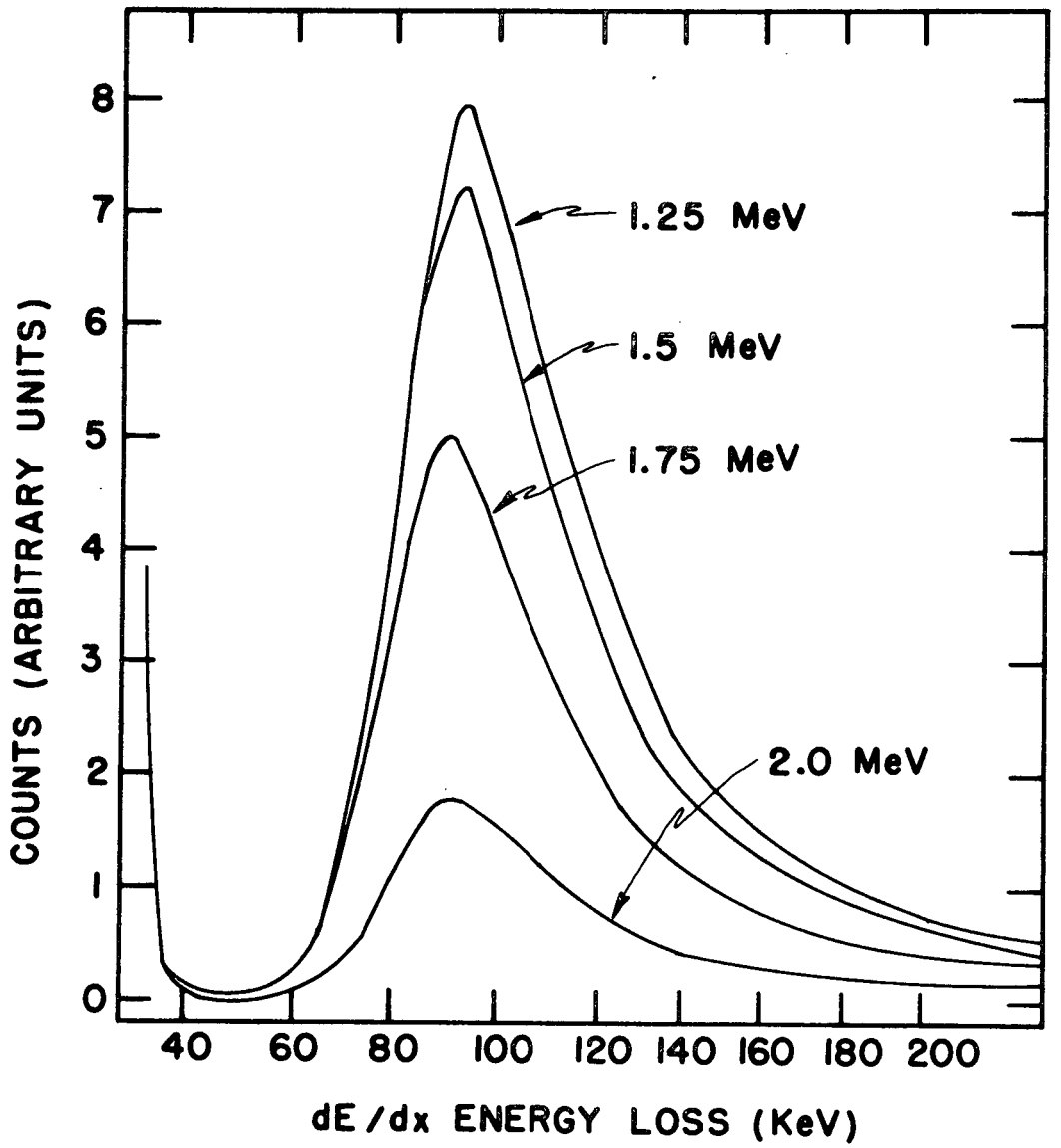
COUNTS (ARBITRARY UNITS)
0
1
2
3
4
5
6
7
8
40
60
80
100
120
140
160
180
200
dE/dx ENERGY LOSS (KeV)
1.25 MeV
1.5 MeV
1.75 MeV
2.0 MeV

Figure (35)

C 2

electrons entering the E3 detector and crossing three surface contact layers, this amounts to an extra 120μg/cm^{-2} of material to penetrate. In terms of thickness of silicon, this amount of material is equivalent to:

$$\frac{120\ g/cm^{-2}}{2.33\ g/cm^{-3}} = 5.15 \times 10^{-5}\ cm\ Si = 0.515\ \ Si \qquad (21)$$

This amount is insignificant compared to the uncertainty in the depth of the 390μ Si equivalent absorber.

For dead layer effects on the energy losses in the P detector, only the front 40μg/cm^{-2} layer of aluminum need be taken into account. This layer is equivalent to 0.172μ of silicon. The maximum effect of this dead layer would correspond to a dE/dx energy loss of 0.065 keV for a 500 keV electron. Compared to the ≈80 keV lost by a 500 keV electron in the P detector, the effect of this dead layer on the P detector response to electrons >500 keV is at most 0.08% or , in other words, completely negligible.

Likewise, for the E1 and E2 detectors, the dead layer is equivalent to ≈0.172μ of silicon. This dead layer has the maximum effect on a ≈30 keV electron, which would experience a dE/dx energy loss of ≈0.3 keV. Thus, the dead layer would cause a maximum reduction in energy loss in the E1 detector of ≈1%. For the E2 detector the maximum effect would be on a 150 keV electron, which would experience a dE/dx energy loss of ≈0.1 keV in the dead layer. This corresponds to a ≈0.07% maximum reduction of energy lost in the E2 detector. Thus, the dead layer effects are negligible compared to the experimental uncertainty of the edge discriminator settings.